Computational Investigations of Organometallic Polymerization Catalyst Reaction Mechanisms

by

Andrew K. Vitek

A dissertation submitted in partial fulfillment
of the requirements for the degree of
Doctor of Philosophy
(Chemistry)
in the University of Michigan
2019

Doctoral Committee:
Associate Professor Paul Zimmerman, Chair
Professor John Kieffer
Professor Anne J. McNeil
Associate Professor Nathaniel K. Szymczak

Andrew K. Vitek
andvitek@umich.edu
ORCID iD: 0000-0002-8940-6829

Dedication

To my parents, whose sacrifices make me forever humble. And to my mentors, whose wisdom make me forever grateful. Thank you.

Acknowledgements

I will be forever grateful for my time spent in Ann Arbor at the University of Michigan. I owe much of my personal growth and many of my accomplishments to the mentors, colleagues, and friends that I met here. I would first like to acknowledge my advisor, Professor Paul Zimmerman, for his guidance, encouragement, and support. Paul exemplifies all the leadership qualities that one could ask for in an advisor. Paul's sharp mind, patience, and unique knack for motivation had an immeasurable influence on the scope and quality of my graduate work. Paul's mentorship has greatly improved my abilities as a scientist. I would also like to thank Professor Anne McNeil for her continual feedback on most of the projects contained in this thesis. I am lucky to have collaborated with Professor McNeil, her group, and other great minds in the polymer chemistry field that I have connected with through her. I am also grateful for my time spent working with Professor Nathaniel Szymczak. Experimental chemistry experience is necessary to keep computational chemists grounded with real chemistry, and I appreciated the opportunity to work in Professor Szymczak's lab. I greatly appreciate Professors John Kieffer, Anne McNeil, and Nathaniel Szymczak for serving on my committee and providing feedback and advice during my graduate career.

Thank you to past and current members of the Zimmerman lab for challenging and helping me throughout my time in graduate school. I am excited to read your future works and witness your future accomplishments.

Thank you to my friends and family for enriching my life in so many meaningful ways. To Casey Vitek, Alan Chien, Ben Meinen, David Lee, and Josh Damron. Thank you for lending your time and attention on our various adventures.

Finally, thank you to the thoughtful and loving Sydney Faylor and the Faylor family. You are the reason that Ann Arbor is – and will always be – home.

Table of Contents

List of Figures

List of Tables

List of Equations

List of Appendices

Abstract

Computational chemistry is a proven tool for creating a better understanding of known chemistry, discovering new mechanisms and chemical reactivity, and systematically improving catalyst and reaction design. The insight that can be gained from computational studies, however, is limited by the accuracy of the models used and often requires an established working knowledge of the chemical system of interest. In addition to this, computational chemistry must be guided and grounded by experiment in order to synergistically approach the goal of achieving a fuller understanding of reaction pathways. The studies herein demonstrate this synergy between computational and experimental chemistry with an emphasis on building realistic computational models for reaction path exploration.

Chapter 1 provides a brief overview of computational chemistry fundamentals that are needed to understand reaction landscapes. This introduction describes the reaction path and transition state finding methods that were used in subsequent studies found in this work. These methods and concepts are then demonstrated via studies on metal-catalyzed polymerization reactions that are led by experiment in Chapter 2. This chapter highlights the computational investigations of these systems that were used to support and extend the chemical insights toward catalyst reactivity.

Chapter 3 describes the computationally-led elucidation of the transmetalation mechanism of thiophene-based conductive polymer synthesis. This work presents a full mechanistic viewpoint of the transmetalation reaction and establishes the chemical details that are necessary for accurately modeling this reaction including realistic models of reagents, consideration of catalyst spin state, and changing steric interactions as polymerization proceeds. The insights gained from this study should aid catalyst design for polymerization reactions and related cross coupling reactions.

Chapter 4 describes conformational effects resulting from the inherent flexibility of organometallic catalysts. This chapter was inspired by the importance of biochemical protein-

substrate conformational effects that prompted the investigation of similar effects in the context of organometallic reactions. This study surveys the conformer ensembles of several bisphosphine nickel catalysts and their reductive elimination pathways. The conformational effects shown in this work result in large reductive elimination ground and transition state effects. Additionally, the conformer analysis revealed that reductive elimination barrier height and the degree of distortion of the reactant geometries contained a high-correlation structure-reactivity relationship. This work should inspire more thorough evaluation of conformer effects for transition-metal-catalyzed reactions.

Significant efforts are still needed to develop and test chemically insightful and accurate computational methods. This work outlines applications of these modern computational tools toward building better models and a developing a deeper understanding of organometallic chemistry and polymer chemistry.

Chapter 1: Introduction

1.1 Investigating Reaction Pathways with Computational Chemistry

Computational chemistry has grown as an established tool for revealing atomistic details of chemical reactivity. Modern advances in computing power and the development of accurate quantum mechanics and molecular dynamics methods has enabled computational chemistry the speed and reliability needed to further develop chemical understanding in cooperation with experimental studies. Density functional theory (DFT) has emerged as a fast, reliable, and cost-effective method for investigating reaction landscapes and computing chemical quantities of interest.[1,2] Computational studies have become vital to chemical understanding due to their ability to map the potential energy surface of a reaction of interest, explore the relevant chemical space of unintuitive chemical steps or unknown intermediates, and identify structure-activity relationships. When combined with experimental studies, synergy between computation and experiment can result in rapid understanding of reaction landscapes and modification and optimization of chemical systems. This work describes the application of DFT and automated reaction path finding in the context of polymerization reactions catalyzed by organometallic complexes.

Chapter 2 will focus on identifying intermediates crucial to catalysis and locating transition states that accurately predict the kinetics of relevant chemical transformations. These studies will feature an enantioselective chromium epoxide polymerization, nickel diimine copolymerization of olefin and thiophene, and nickel diimine thiophene homopolymerization.

Chapter 3 will highlight the complicated transmetalation reaction featured in conductive polymer synthesis and Kumada coupling. Chapter 4 will focus on applying the aforementioned computational techniques to assess organometallic catalyst conformational effects on reductive elimination. Before discussing these applications of computational methods, a brief introduction of the relevant background information is presented below. While not exhaustive, the following information will cover relevant material needed for understanding the computational studies contained in this work. Extensive reviews on computational chemistry methods and techniques are available for the interested reader if more information is desired.[3–5]

1.2 Chemical Space, Potential Energy Surfaces, and Predicting Reaction Rates

The potential energy surface (PES) is a multi-dimensional surface that depicts the energy of a molecule, catalyst, or collection of starting reagents as a function of their interatomic distances. The dimensionality of a PES is approximately equal to 3N dimensions where N is the number of atoms in a given system. While experimental chemistry naturally samples and navigates this highly complex space, *ab initio* simulations are challenged with identifying and sampling only the most relevant chemical space of a PES. DFT, transition state search methods, and other modern computational methods allow for the efficient exploration of this relevant chemical space by identifying stationary points along the PES that represent local minima (reactants, products, and stable intermediates) and the transition states that connect local minima. These two types of structures (local minima and transition states) are the chemically accessible parts of a PES that are relevant to chemistry conducted at most reasonable temperatures.

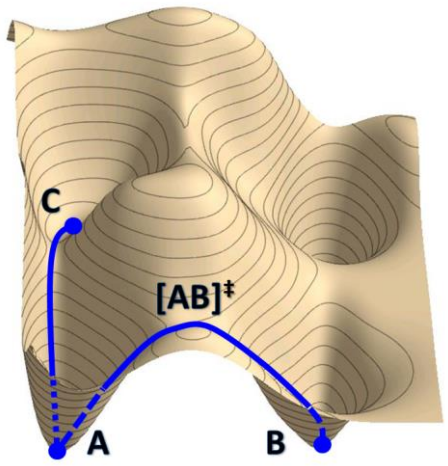

Figure 1.1: Sample potential energy surface that depicts a global minimum (A), two local minima (B and C). $[AB]^{‡}$ indicates a transition state that is the minimum energy path between A and B.

Minima found within a PES represent thermodynamically stable reactants, intermediates, and products. These geometries can be optimized for a given level of theory using standard optimization methods in most quantum chemical packages.[3,5,6] Figure 1.1 depicts an example PES where structure A represents a global minimum. Structures B and C are local minima that correspond to reactive intermediates that are connected via transition states (e.g. $[AB]^{‡}$). The transition states follow a minimum energy path from reactants to reactive intermediates; this is considered an elementary step. Over a few to several elementary steps, the reactants can navigate a PES to eventually reach the products. Plotting the reaction path versus the energy of the various species (shown in Figure 1.2) allows us to calculate quantities that are relevant for understanding the equilibrium of species in solution or the rate of reaction. Mapping the PES to provide the Gibbs free energy of activation ($\Delta G^{‡}$) and the Gibbs free energy of reaction (ΔG) is shown below.

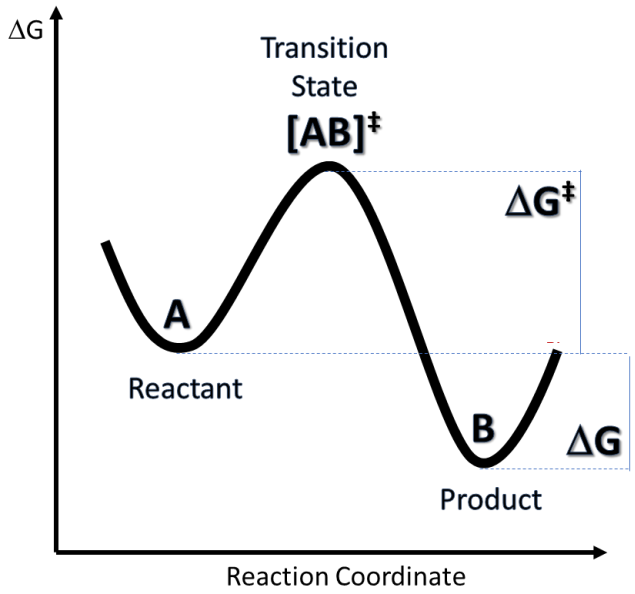

Figure 1.2: 2-dimensional reaction coordinate for the example PES in Figure 1.1.

Computing Gibbs free energies of the relevant minima and transition states is useful because they can be used to calculate equilibrium concentrations of various species on the PES. Normally, equilibrium constants of stable species would be trivial to obtain via experiment. However, a delicate equilibrium of reactive but unobservable intermediates may be important for the product distribution of a total reaction. Additionally, one can predict the efficiency of a reaction if it is directly related to the total change in Gibbs free energy. Computational chemistry can be used to predict such cases with the equilibrium expression for K_{eq} shown below (Equation 1.1).

$$K_{eq} = e^{-\frac{\Delta G}{RT}} = \frac{[A]^{\sigma}}{[B]^{\rho}}$$

Equation 1.1. Equilibrium constant expression.

In Equation 1.1, K_{eq} is the equilibrium constant for a reaction which can be used to determine equilibrium concentrations of chemical species ([A] and [B]) based on the change in Gibbs free energy (ΔG) and the temperature of the reaction (T). R is the universal gas constant and σ and ρ correspond to the reaction order of each species. This simplified example demonstrates how calculated Gibbs free energies can be used to predict a useful, experimentally observable quantity when a reaction is controlled by the thermodynamic change of a system.

Additionally, transition state information is valuable when a chemical system exhibits kinetic control. The Eyring equation relates transition state energies ($\Delta G^{\ddagger}$) with the rate of reaction in the equation below.

$$r_{\{A \rightarrow B\}} = \kappa \left(\frac{k_B T}{h} \right) e^{-\left(\frac{\Delta G^{\neq}}{RT} \right)}$$

Equation 1.2. Eyring equation relating the reaction rate, *r*, and $\Delta G^{\ddagger}$.

In Equation 1.2, *r* is the rate of the reaction A→B, κ is the transmission coefficient, k_B is Boltzmann's constant, T is temperature in Kelvin, *h* is Planck's constant, R is the universal gas constant, and $\Delta G^{\ddagger}$ is the transition state energy for the reaction A→B. This equation can be used to predict experimentally observed chemical rates but is generally more useful when using computations to predict relative rates of competing reactions.

While stable intermediate geometries are generally trivial to obtain, transition state structures are slightly more difficult. The reasons for this and a description of transition state search methods including the growing string method (GSM) used in this work are described below.

1.3 Transition State Finding Methods

The high dimensionality of PESs makes an exhaustive search of the relevant chemical space impractical due to time and computational restrictions. A directed approach that only explores the relevant chemical space of a given reaction involves identifying nearby, meta-stable intermediates, generating the transition states that connect reactants and intermediates to one another, and repeating this process until one has navigated to product structures. Identifying accurate transition states that connect the local minima on a PES is crucial in understanding the kinetic feasibility of certain elementary steps and obtaining transition state energies that can be used to predict relative chemical rates for competing reactions. Geometric information is generally available for stable reactants and products which allows for qualitatively accurate "guess" structures, which can then be optimized by quantum mechanical methods to generate accurate structures for a given level of theory with relative ease. Transition state structures, however, have less available geometric information which makes accurate and automated methods for generating transition state geometries an important part of PES exploration.

An accurate transition state is a first order saddle point along the minimum energy path that connects the reactant and product of an elementary step. This saddle point is a maximum in the direction of the reaction path where the normal mode of the transition state's single imaginary frequency reflects the change from reactants to products and is a minimum in all other directions. Difficulties in obtaining accurate transition states for chemical reactions stem from the need to fulfill the above characteristics, the high dimensionality of the PES, and a general lack of chemical knowledge of transition state geometries. The two main methods for locating transition states are local surface-walking algorithms[7–12] and interpolation methods.[13–22] Surface-

walking methods generally start from a guess transition state structure and are optimized until a saddle point that meets the transition state criteria are fulfilled. These methods can suffer from costly calculations when the guess structure is qualitatively far from the true transition state which can be problematic when little information about the transition state geometry is known.

Interpolation methods produce geometries between the reactant and product which guarantees that the transition state is along a given reaction coordinate. These methods are some of the most commonly utilized transition state search methods because they require less user input and do not require an initial transition state guess. Interpolation methods in widespread use for transition state finding include the nudged elastic band method (NEB)[13–16] and growing string methods (GSM).[17–22] The NEB method requires reactant and product input and generates an interpolated set of nodes or geometries between the two points to form a reaction path. Spring interactions between neighboring nodes are used to create a continuous reaction path. Double-ended string methods[17–21] and single-ended string methods[22] are similar to the NEB method in that these two methods populate a reaction path with interpolated images or nodes between the reactant and product. For double-ended string methods, a designated number of nodes are grown inward from the reactant and product. After optimizing the newly generated nodes, additional nodes that approach a transition state guess structure are added and the nodes are reparametrized to ensure equal spacing. The single-ended growing string method requires only reactant input and driving coordinates that describe a desired reaction. The string is grown until a transition state region is traversed, then the string is optimized to refine the reaction path and transition state. A more detailed explanation of the single-ended and double-ended string methods used in this work to generate reaction paths is provided below.

1.4 Transition State Finding via Growing String Methods

String methods are established, reliable transition state search methods that come in two forms, double- and single-ended string methods. Double-ended methods require both initial and final geometries to be known in order to generate an approximate reaction coordinate. Nodes in between the initial and final product are added and relaxed such that the nodes follow the minimum energy pathway connecting the two structures. When enough nodes are added such that the pathway proceeds downhill rather than uphill (after passing a transition state), the highest energy node should have a structure close to that of the exact transition state. This transition state node can be further optimized using methods that relax the geometry in all directions except the direction of the reaction path.[6,23] Single-ended methods do not require a final structure and produce a reaction path via driving coordinates in the form of changing interatomic distances, bonds, and torsions. A schematic that illustrates a growing string method transition state search is shown below in Figure 1.3.

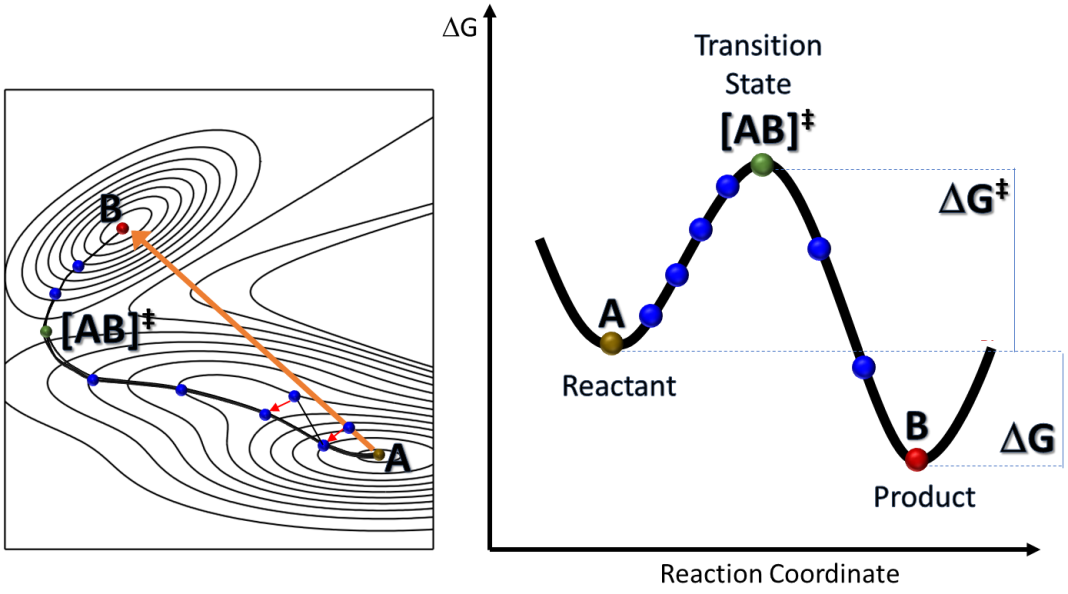

Figure 1.3: Single-ended growing string method schematic.

The computational studies contained in this work demonstrate exploratory and necessary chemical considerations needed when creating models that accurately predict chemical reactivity. Once reasonable reactant models have been constructed, transition state geometries were obtained via single-ended and double-ended string methods in order to elucidate novel pathways, identify structure-activity relationships, and better understand chemical reactivity/selectivity. Established understanding of the mechanisms contained herein from previous experimental and computational works vary greatly which necessitates careful consideration of what chemical features must be modeled to accurately predict reactivity. Brief examples of experimentally driven works on organometallic polymerization reactions with our computational contributions are provided below.

1.5 Dissertation Outline

Chapter 1 provides a brief overview of how computational tools are used to explore reaction pathways and inform chemical understanding. In Chapter 2, these tools and concepts are applied to computations that are used to support the findings of polymerization reactions catalyzed by nickel(II) diimines and an additional example of enantioselective epoxide polymerization. The following chapters will further demonstrate these ideas in the context of polymer chemistry reactions catalyzed by organometallic complexes.

Chapter 3 is a complete mechanistic investigation of the transmetalation reaction involved in the polymerization of thiophene conductive polymers catalyzed by nickel(II) diimines. For thiophene polymerization catalyzed by nickel diimines, the catalytically active intermediate is known to undergo a change in spin state from a high-spin tetrahedral precatalyst geometry to a low-spin square planar geometry during polymerization. The most stable spin state

of various catalytic intermediates during polymerization and the active spin state during transmetalation, however, are not well studied. The bimolecular nature of Kumada coupling-based transmetalation reactions and important solvent effects increase the system size needed to accurately model the reaction and has dissuaded computational chemists from devising an accurate model for transmetalation. This study will detail catalyst electronic states, steric environment, and chemically accurate models of reagents. Once reasonable starting structures are identified for the transmetalation reaction, transition states for high-spin and low-spin transmetalation pathways will be obtained via de-GSM to identify the active pathway. These varied considerations will be demonstrated as necessary for accurately modeling Grignard-based transmetalation reactions.

Chapter 4 details conformational effects in the context of reductive elimination via nickel(II) bisphosphine catalysts. This investigation is an attempt to better understand the ability of catalysts with flexible ancillary and reactive ligands to adopt several conformations or conformers. All possible conformers of eight bisphosphine catalysts with varying side chain size and backbone length are generated by systematically rotating all bonds in the ancillary ligand to identify unique, stable conformers. Finally, transition states for each unique conformer are obtained via se-GSM. These conformers can vary greatly in energy and can lead to unique reductive elimination pathways that also show high variance in transition state energies and barrier heights. This can result in potentially large calculated barrier inaccuracies – especially when comparing ancillary ligands of varying flexibility. Much of the potential barrier inaccuracy stems from the difficulties associated with identifying the global minimum and minimum energy transition state when a catalyst exhibits conformational flexibility. Ultimately, this study describes how the conformational flexibility of organometallic catalysts result in large ground

and transition state effects and can be used to discover meaningful chemical details about reductive elimination of thiophene-ligated organometallic complexes.

Chapter 5 will include Final Remarks, a summary of the studies contained herein, and a discussion of the limitations of this work.

1.6 References

(1) Becke, A. D. Perspective: Fifty Years of Density-Functional Theory in Chemical Physics. *J. Chem. Phys.* **2014**, 140 (18), 18A301.

(2) Burke, K. Perspective on Density Functional Theory. *J. Chem. Phys.* **2012**, 136 (15), 150901.

(3) Schlegel, H. B. Geometry Optimization. *Wiley Interdiscip. Rev. Comput. Mol. Sci.* **2011**, 1 (5), 790–809.

(4) Wales, D. J. Energy Landscapes: Calculating Pathways and Rates. *Int. Rev. Phys. Chem.* **2006**, 25 (1–2), 237–282.

(5) Schlegel, H. B. Exploring Potential Energy Surfaces for Chemical Reactions: An Overview of Some Practical Methods. *J. Comput. Chem.* **2003**, 24 (12), 1514–1527.

(6) Schlegel, H. B. Geometry Optimization on Potential Energy Surfaces. *Modern Electronic Structure Theory*. **1995**; pp 459–500.

(7) Halgren, T. A.; Lipscomb, W. N. The Synchronous-Transit Method for Determining Reaction Pathways and Locating Molecular Transition States. *Chem. Phys. Lett.* **1977**, 49 (2), 225–232.

(8) Müller, K.; Brown, L. D. Location of Saddle Points and Minimum Energy Paths by a Constrained Simplex Optimization Procedure. *Theor. Chim. Acta* **1979**, 53 (1), 75–93.

(9) Dewar, M. J. S.; Healy, E. F.; Stewart, J. J. P. Location of Transition States in Reaction Mechanisms. *J. Chem. Soc. Faraday Trans. 2* **1984**, 80 (3), 227.

(10) Ionova, I. V.; Carter, E. A. Ridge Method for Finding Saddle Points on Potential Energy Surfaces. *J. Chem. Phys.* **1993**, 98 (8), 6377–6386.

(11) Cerjan, C. J.; Miller, W. H. On Finding Transition States. *J. Chem. Phys.* **1981**, 75 (6), 2800–2806.

(12) Henkelman, G.; Jónsson, H. A Dimer Method for Finding Saddle Points on High Dimensional Potential Surfaces Using Only First Derivatives. *J. Chem. Phys.* **1999**, 111 (15), 7010–7022.

(13) Trygubenko, S. A.; Wales, D. J. A Doubly Nudged Elastic Band Method for Finding Transition States. *J. Chem. Phys.* **2004**, 120 (5), 2082–2094.

(14) Henkelman, G.; Uberuaga, B. P.; Jónsson, H. A Climbing Image Nudged Elastic Band Method for Finding Saddle Points and Minimum Energy Paths. *J. Chem. Phys.* **2000**, 113 (22), 9901–9904.

(15) Henkelman, G.; Jónsson, H. Improved Tangent Estimate in the Nudged Elastic Band Method for Finding Minimum Energy Paths and Saddle Points. *J. Chem. Phys.* **2000**, 113 (22), 9978–9985.

(16) Maragakis, P.; Andreev, S. A.; Brumer, Y.; Reichman, D. R.; Kaxiras, E. Adaptive Nudged Elastic Band Approach for Transition State Calculation. *J. Chem. Phys.* **2002**, 117 (10), 4651–4658.

(17) Zimmerman, P. Reliable Transition State Searches Integrated with the Growing String Method. *J. Chem. Theory Comput.* **2013**, 9 (7), 3043–3050.

(18) Zimmerman, P. M. Growing String Method with Interpolation and Optimization in Internal Coordinates: Method and Examples. *J. Chem. Phys.* **2013**, 138 (18), 184102.

(19) Peters, B.; Heyden, A.; Bell, A. T.; Chakraborty, A. A Growing String Method for Determining Transition States: Comparison to the Nudged Elastic Band and String Methods. *J. Chem. Phys.* **2004**, 120 (17), 7877–7886.

(20) E, W.; Ren, W.; Vanden-Eijnden, E. Finite Temperature String Method for the Study of Rare Events †. *J. Phys. Chem. B* **2005**, 109 (14), 6688–6693.

(21) E, W.; Ren, W.; Vanden-Eijnden, E. String Method for the Study of Rare Events. *Phys. Rev. B* **2002**, 66 (5), 052301.

(22) Zimmerman, P. M. Single-Ended Transition State Finding with the Growing String Method. *J. Comput. Chem.* **2015**, 36 (9), 601–611.

(23) Peng, C.; Ayala, P. Y.; Schlegel, H. B.; Frisch, M. J. Using Redundant Internal Coordinates to Optimize Equilibrium Geometries and Transition States. *J. Comput. Chem.* **1996**, 17 (1), 49–56.

Chapter 2: Applications of Pathway Exploration Methods on Chemical Systems

The following sections are dedicated to our computational contributions to the work of our experimental collaborators. It is necessary to have computational chemistry grounded with experimental studies such that unrealistic models can be quickly improved upon to give accurate and chemically meaningful results. The three following studies should highlight the ability of simulation to provide detailed chemical explanations that help support experimental observations.

2.1 Pathway Exploration of Olefin-Thiophene Copolymerization Switching Catalysis Mechanism

The following content is associated with the publication below.

- Souther, K. D.; Leone, A. K.; Vitek, A. K.; Palermo, E. F.; LaPointe, A. M.; Coates, G. W.; Zimmerman, P, M.; McNeil, A. J. Trials and Tribulations of Designing Multitasking Catalysts for Olefin/Thiophene Block Copolymers. *J. Poly. Sci., Part A: Polym. Chem.*, **2018**, *56*, 132-137.

The following section is dedicated to the work of Souther, Leone, McNeil, and co. regarding the difficulties designing a multitasking block copolymerization catalyst. The general reaction scheme is shown below in Figure 1.4 and the simulations that support the experimentally observed slow chain transfer process and catalyst dissociation from the growing polymer are provided below.

2.1.1. Introduction

Block copolymers are a class of copolymers composed of blocks of chemically distinct monomer sequences. The ability to incorporate monomer sequences with different properties into diverse polymer architectures has led to the discovery of materials with advanced and unique materials properties.[1–4] Synthesis of block copolymers with chemically similar monomers is often possible in a single pot because the monomers undergo the same polymerization mechanism. Challenges in block copolymerization arise when incorporating monomers with significantly differing chemical properties (i.e. insulating polyolefin and conducting polythiophene polymers). One method for synthesizing block copolymers with chemically distinct monomers involves coupling reactions that connect polymer blocks with active chain-ends.[5,6] This method was achieved for combining regioregular poly(3-hexylthiophene) (P3HT) and polyethylene (PE) by an innovative strategy of using allyl-functionalized thiophene end-groups to allow for subsequent ring-opening metathesis polymerization (ROMP).[5] This method, however, suffers from requiring multiple catalysts, separations, and purifications which makes the polymerization scale poorly. A more scalable method for obtaining P3HT-PE block copolymers involves using a single catalyst that can enchain and polymerize one monomer and then undergo a switch in reactivity such that the catalyst can polymerize another chemically distinct monomer. This method is generally limited to monomers that undergo the same polymerization mechanism due to the difficulties in identifying a catalyst and catalytic conditions that can undergo a drastic change in mechanism required to polymerize to distinct monomers.

The McNeil group identified a Ni(II) species capable of polymerizing P3HT and PE albeit at different reaction conditions. Optimizing the catalyst system to make the P3HT and PE polymerizations compatible in a single pot involved identifying an appropriate precatalyst,

activator, olefin monomer, and reaction conditions. Despite efforts to make the two distinct polymerization mechanisms compatible, the reaction produced only a small amount of P3HT-PE copolymer with P3HT homopolymer as the major product. This result is likely due to a high barrier reductive elimination that occurs when the catalyst switches from olefin to thiophene polymerization. An overview of the copolymerization mechanism and the computed switching mechanism are described herein.

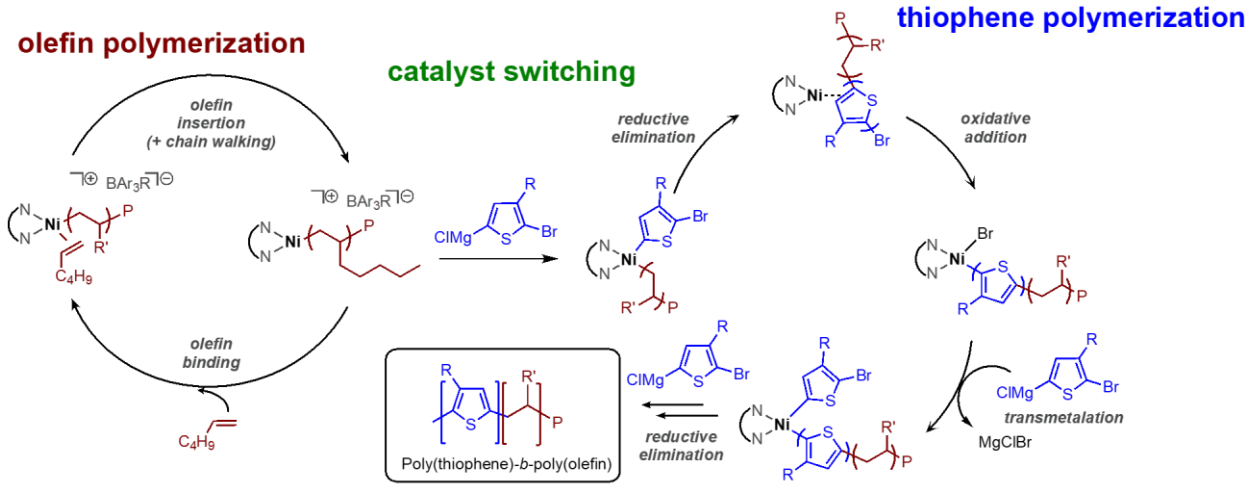

Figure 2.1: Olefin-thiophene copolymerization mechanism.

The difficult task of using a single catalyst to efficiently perform and switch between two distinct polymerization mechanisms is shown in Figure 2.1. The McNeil group identified a nickel catalyst (**C0** shown in Figure 2.2) capable of producing polyolefin via terminal alkene polymerization and regioregular polythiophene. Souther and co. identified a discrete form of this catalyst, a bis-methylene trimethylsilyl precatalyst, that could be activated for polymerization of 1-pentene in neat conditions. They also developed reaction conditions that allowed for both polymerizations to occur whereas typical reaction conditions for olefin and thiophene polymerizations are incompatible. Following this, unreacted 1-pentene monomer was removed

from the solution due to the ability of the alkene to coordinate to the nickel catalyst and disrupt thiophene polymerization (see Figure 2.3).

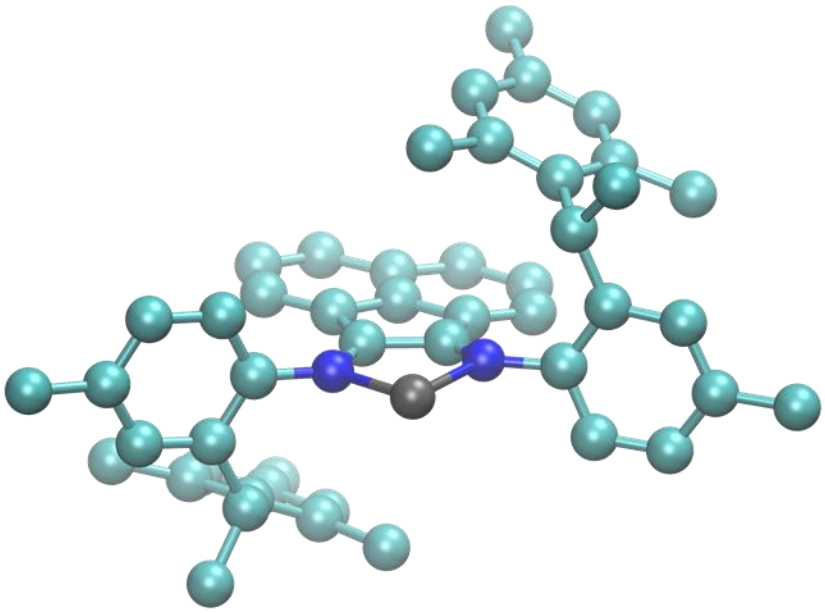

Figure 2.2: C0, switching catalyst diimine ancillary ligand structure.

2.1.2. Discussion

Although the computational studies shown below did not identify a distinct catalyst dissociation mechanism, binding energies between the **C0** and various species in solution (shown in Figure 2.3) indicate that several species have binding energies comparable to the modeled copolymer (3-bromo-2,5-dimethylthiophene). This supports the experimental observation of polymer-catalyst dissociating after the addition of thiophene Grignard monomer. Additionally the potential energy surface for the switching transmetalation was explored and is shown below in Figure 2.4.

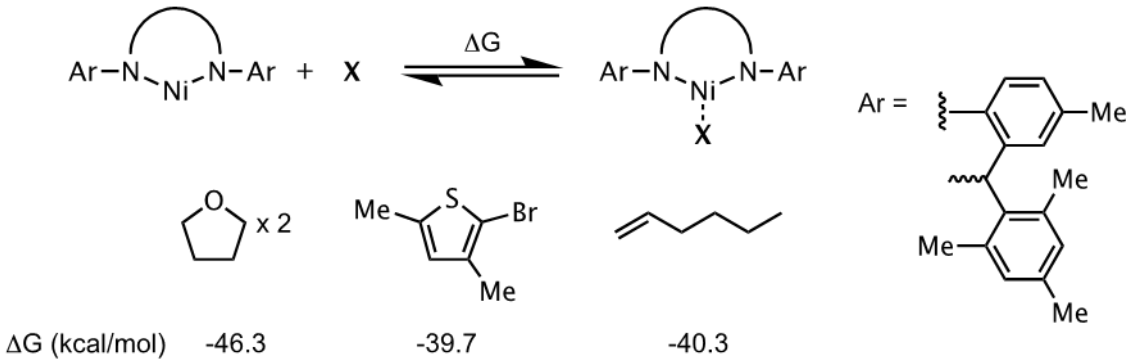

Figure 2.3: Binding energy calculations of Ni(0) to species in solution for copolymerization.

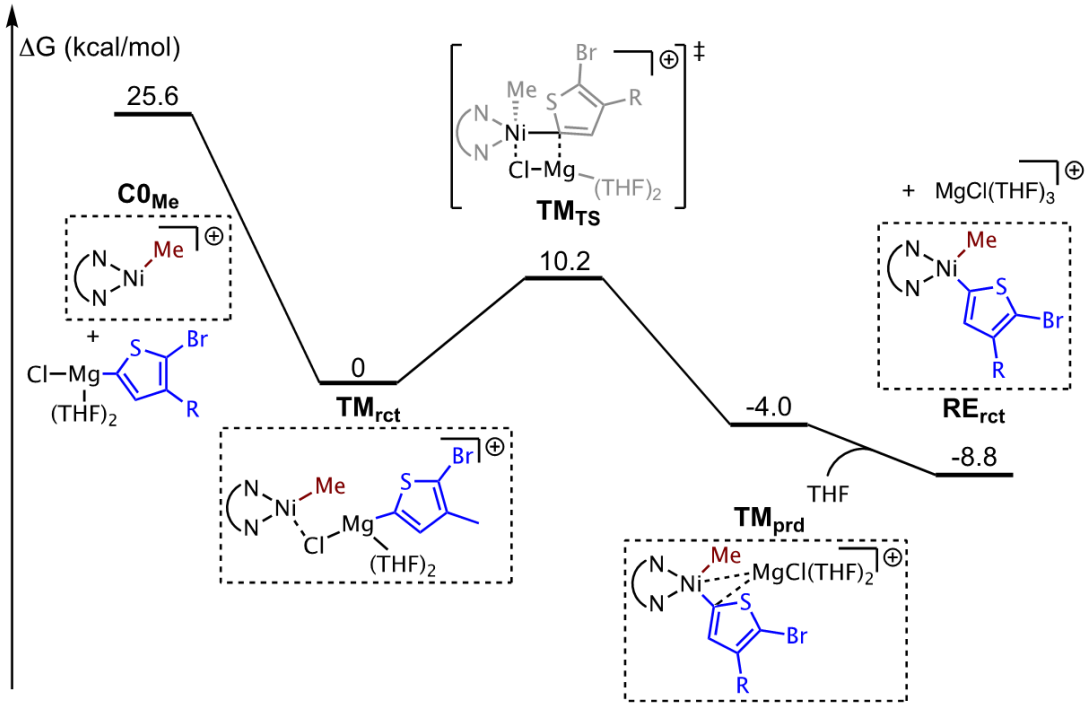

Figure 2.4: The potential energy surface for transmetalation with thiophene at the cationic nickel center.

The relative rates of sp^2-sp^3 reductive elimination, (Figure 2.5, red pathway) compared to thiophene homopolymerization (sp^2-sp^2 reductive elimination, black pathway) were computed for catalyst **C2**. The reaction begins at $\mathbf{RE_{rct}}$ and proceeds through the three-membered transition state, $\mathbf{RE_{ts}}$ to form the π-complex intermediate $\mathbf{RE_{prd}}$. The calculated difference between the two reductive elimination pathways predicts slow sp^2-sp^3 reductive elimination and fast thiophene

homocoupling. At room temperature, the 4.2 kcal/mol preference for the black pathway would result in a switching step that is approximately 1,000 times slower than thiophene homocoupling. This is in good agreement with experiments that exhibited slow switching. The reductive elimination barriers for other alkyl and thiophene ligands were examined in the ligand survey in Figure 2.5. These calculations showed that sp^2-sp^3 reductive elimination barriers slightly decrease with decreasing size of the alky reactive ligand. Reductive elimination involving two thiophene ligands remains fast in comparison, and the activation barrier decreases by about 3 kcal/mol for the dithiophene reactive ligand.

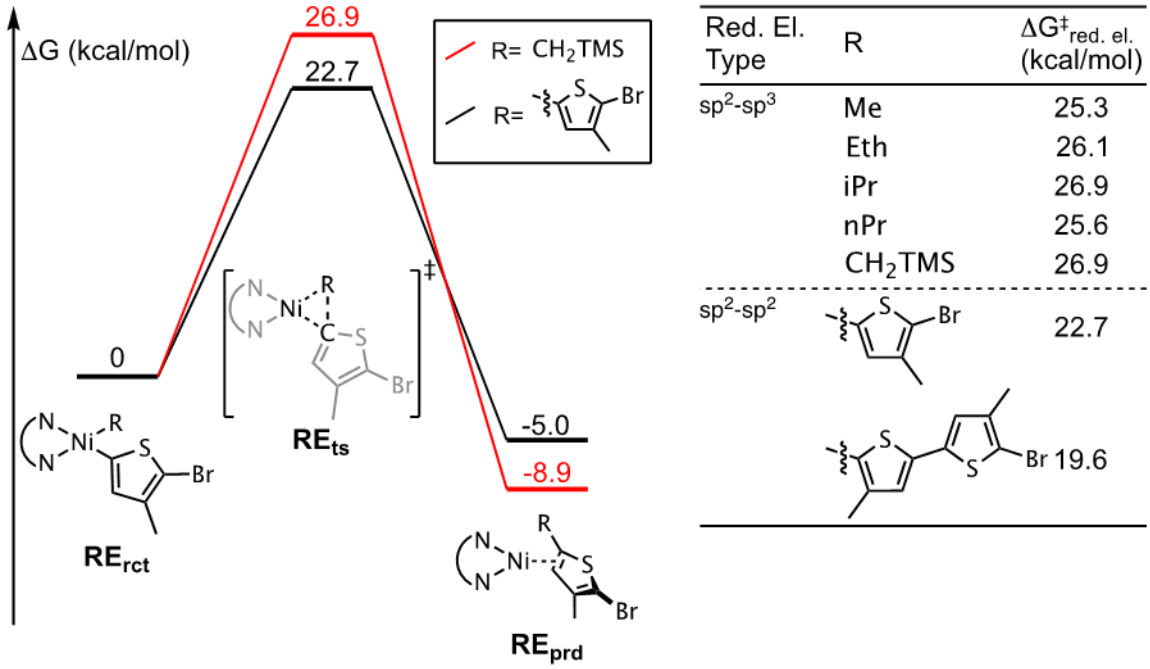

Red. El. Type	R	$\Delta G^{\ddagger}_{red.\ el.}$ (kcal/mol)
sp^2-sp^3	Me	25.3
	Eth	26.1
	iPr	26.9
	nPr	25.6
	CH_2TMS	26.9
sp^2-sp^2		22.7
		19.6

Figure 2.5: The potential energy surface for sp^2-sp^3 and sp^2-sp^2 reductive elimination.

2.1.3. Conclusions

This work supported experimental observations of a slow switching step that resulted in very little chain transfer and only a small observable amount of olefin-thiophene copolymer. While these computational studies did not identify the source of catalyst dissociation that led to thiophene homopolymerization, they did provide important insight toward designing a

multitasking catalyst. The source of difficulty for the catalyst switching from olefin to thiophene polymerization was identified as the high barrier alkyl-thiophene reductive elimination step. Further optimization of this difficult copolymerization would involve reducing this barrier that could be achieved via ancillary ligand modification to accelerate reductive elimination, the use of additives that achieve the same effect, or the copolymerization of monomers that undergo a more facile reductive elimination (sp^2-sp^2 or sp^3-sp^3).

2.2 Determining Source for Non-Living Thiophene Polymerization via Nickel Diimines

The following content is associated with the publication below.

- Leone, A. K.; Souther, K. D.; Vitek, A. K.; LaPointe, A. M.; Coates, G. W.; Zimmerman, P, M.; McNeil, A. J. Mechanistic Insight into Thiophene Catalyst-Transfer Polymerization Mediated by Nickel Diimine Catalysts. *Macromolecules*, **2017**, *50*, 9121-9127.

The following section is dedicated to the work of Leone, Souther, McNeil, and co. in elucidating the chain-growth polymerization of thiophene with nickel diimine catalysts. The computational work below describes our contributions to understanding how ancillary ligands can determine the ability of a catalyst to undergo chain-growth polymerization. The general reaction scheme and the simulations that support experimental observation of distinct polymerization mechanisms exhibited by different catalysts are provided below.

2.2.1. Introduction

Catalyst transfer polymerization[7–10] (CTP) is a living polymerization method for conjugated polymer synthesis where the growing polymer chain remains bound to an active catalyst via an associative metal-polymer π-complex.[11] This method is useful for producing

conjugated polymers with controlled length because the growing polymer chains experience linear growth with respect to time. This allows for the polymerization to terminated at any time to give polymers with predictable molecular weight. The living nature of the polymerization also allows for sequence control, where new conductive monomers can be added to the polymerization to form block copolymers and gradient copolymers. One limitation of CTP is the current inability to polymerize large monomers with fused arene groups.[12,13] While the source for the inability to polymerize larger monomers is currently unknown, unproductive pathways are thought to occur when the metal-polymer π-complex is either too stable (resulting in high barriers for polymerization to proceed) or too unstable (resulting in catalyst-polymer dissociation).

Nickel(II) diimine catalysts are recently discovered class of CTP catalysts for the polymerization of poly(3-hexylthiophene) (P3HT). Some of the first diimine ligands used in conductive polymer synthesis were unencumbered diimine ancillary ligands used to generate P3HT, polybenzotriazole, and other electron-deficient conductive polymers,[14–17] however these systems often exhibited chain-growth only at low monomer conversion. In this study, the McNeil group designed new diimine ligand scaffolds to better understand the relationship between steric and electronic properties of the diimine ancillary ligand and the chain-growth properties of the resulting polymerization. The polymerization reactions described in this study detail how varying the steric properties of the ancillary ligand results in a wide range of P3HT molecular weights and dispersities. This relationship between the steric properties of the ancillary ligand and the control of the polymer properties is thought to be the result of the strength of the metal-polymer π-complex. The computational investigation of the metal-polymer π-complex shown herein

revealed that bis-naphthyl diimines exhibit Ni-ligand π-interactions that can allow for catalyst-polymer dissociation.

2.2.2. Discussion

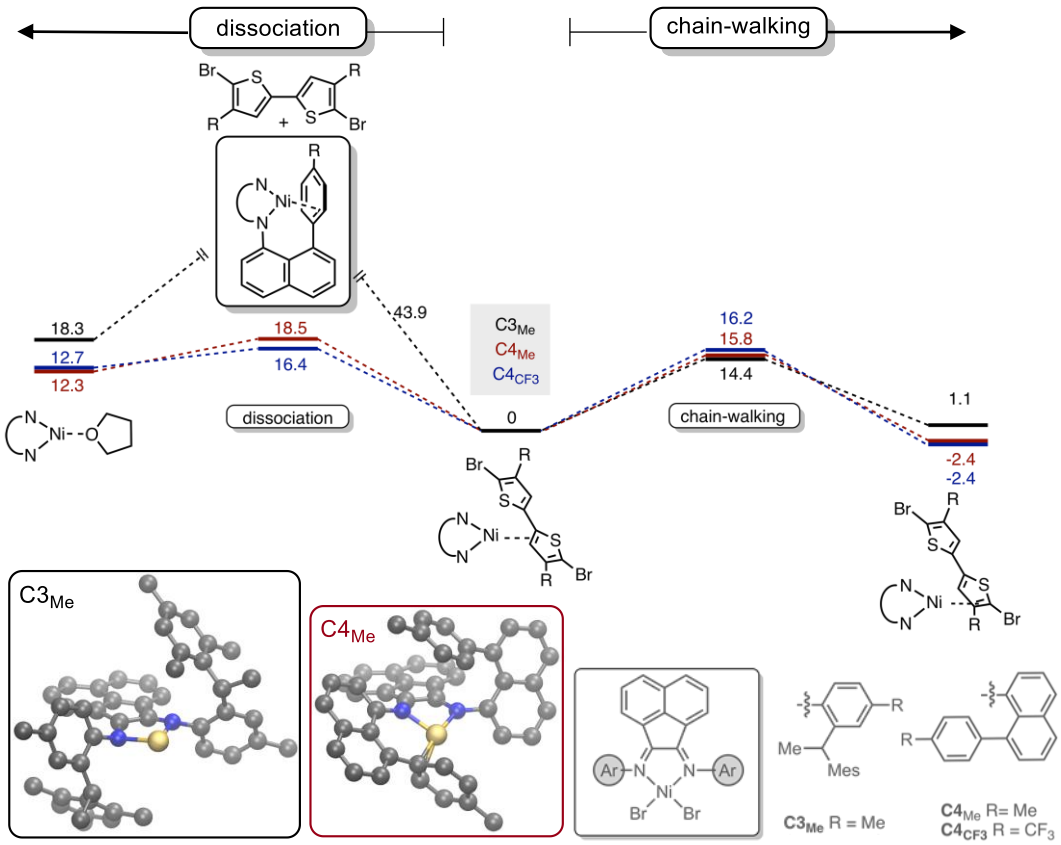

Figure 2.6: Free energy landscape of catalyst dissociation versus ring walking for **C3$_{Me}$**, **C4$_{Me}$**, and **C4$_{CF3}$**.

In transition-metal-catalyzed thiophene polymerization, catalyst-polymer association and ring walking are important for catalytic control over polymer growth. Catalyst-polymer association is required for the polymer chains to have a uniform size while ring walking is the step required for the catalyst to migrate to the reactive end of the polymer to continue chain growth. Leone, McNeil, and co. identified several nickel diimine catalysts capable of thiophene polymerization. Examples of two classes of these catalysts (**C3** and **C4**) are shown in Figure 2.6. The **C4** catalysts (**C4$_{Me}$** and **C4$_{CF3}$**) exhibited poorer conversion, lower polymer molecular

weight, and high dispersity than **C3$_{Me}$**. We sought to find the chemical reason for the low performance of **C4$_{Me}$** and **C4$_{CF3}$**. Figure 2.6 proposes that catalyst-polymer dissociation may be facilitated by self-association of the nickel with the para-tolyl group of the **C4** catalysts. This metal-π interaction is prevented in the **C3$_{Me}$** catalyst by the inflexible aryl arm. The metal-π interaction exhibited by the C4 catalysts acts as a proxy for catalyst dissociation and is competitive with ring walking which results in the poor control over molecular weight and dispersity.

2.2.3. Conclusions

This experimental study on nickel diimine P3HT polymerizations provided one of the first thorough investigations for assessing the living nature of conjugated polymerization catalysts. The McNeil group were able to synthesize P3HT diimine catalysts that exhibited a range of chain-growth properties from high to low molecular weight and dispersion for the resulting polymers. Computational studies were used to identify the sources of differing reactivity for the tested catalysts. Computed pathways for the productive ring walking step necessary for polymer propagation showed a facile step for all observed catalysts. Calculated binding energies between a thiophene dimer and each catalyst revealed ligand-metal self-association for a class of diimine ancillary ligand containing naphthyl side chains. This self-association is likely the source for catalyst-polymer dissociation which results in poor chain-growth conditions. The experimental portion of this work finely details necessary considerations for designing highly active CTP catalysts for 3HT polymerization while the computational studies were used to explain a potential dissociation mechanism that leads to poor chain-growth conditions. Ultimately, this study can be used to finely tune the design of CTP catalysts for proper living, chain-growth conditions while avoiding undesirable catalyst-polymer dissociation pathways.

2.3 Enantioselective Epoxide Polymerization via Bimetallic Chromium Catalysts – Determining the Source for Enantioselectivity

The following content is associated with the publication below.

- Childers, M. I.; Vitek, A. K.; Morris, L. S.; Widger, P. C. B.; Ahmed, S. M.; Zimmerman, P, M.; Coates, G. W. Isospecific, Chain Shuttling Polymerization of Propylene Oxide using a Bimetallic Chromium Catalyst: A New Route to Semicrystalline Polyols. *J. Am. Chem. Soc.*, **2017**, *139*, 11048-11054.

The following section is dedicated to the work of Childers, Morris, Coates, and co. pertaining to a bimetallic chromium catalyst (***rac*-1**) that can be used to form isotactic poly-(propylene oxide) (*i*PPO). The general reaction scheme is shown below in Figure 2.7 and the simulations that support the experimentally observed enantioselectivity follow.

2.3.1. Introduction

Poly(propylene oxide) (PPO) is useful polymer because its reactive end-groups can be incorporated into other macromolecules to form higher ordered polymer architectures in a controlled manner.[18] This functionality allows PPO to be incorporated into polyurethanes used in industrial adhesives.[19] Three methods for generating *i*PPO exist for homogeneous systems. The first involves the catalyzed polymerization of enantiopure propylene oxide.[20–22] This method, however, is not economical due to the high cost of separating PO enantiomer in a racemic mixture. A second method involves using an enantioselective catalyst that reacts with only one of the PO enantiomers in a racemic mixture of PO (Figure 2.7).[23–25] This method has the benefit of generating *i*PPO and enantiopure, unreacted PO monomer, however, the method is inappropriate for large-scale production because only 50% of the monomer is consumed. A third method involves isospecific polymerization of *i*PPO using a racemic mixture of PO and a

racemic mixture of enantioselective catalysts.[26–28] This can be accomplished by using two enantioselective catalysts that polymerize each "matching" propylene oxide enantiomer.

The Coates group initially identified a bimetallic cobalt salen catalyst that enantioselectively polymerizes propylene oxide.[26] The enantioselectivity for this catalyst was remarkably high and resulted in producing highly isotactic PPO. One drawback of the cobalt catalyst was that it required separate syntheses for each of the cobalt salen catalyst enantiomers. The Coates group then developed a racemic chromium salalen catalyst (the (*S*) enantiomer is shown in Figure 2.7) that could be synthesized in a single pot and potentially polymerize PO. The chromium salalen catalysts also had the benefit of being compatible with chain-shuttling agents, which allowed for generating polymers that have isotactic stereoblocks with uniform molecular weight and dispersity. The computations contained herein describe the source of enantioselectivity for the chromium salalen catalyst via simulated PO polymerization initiation and propagation steps comparing the reactivity of each propylene oxide enantiomer. Due to the large number of possible catalyst isomers, all potential catalyst stereoisomers, post-activation regioisomers, and spin states are considered to identify the most stable form of the catalyst.

2.3.2. Discussion

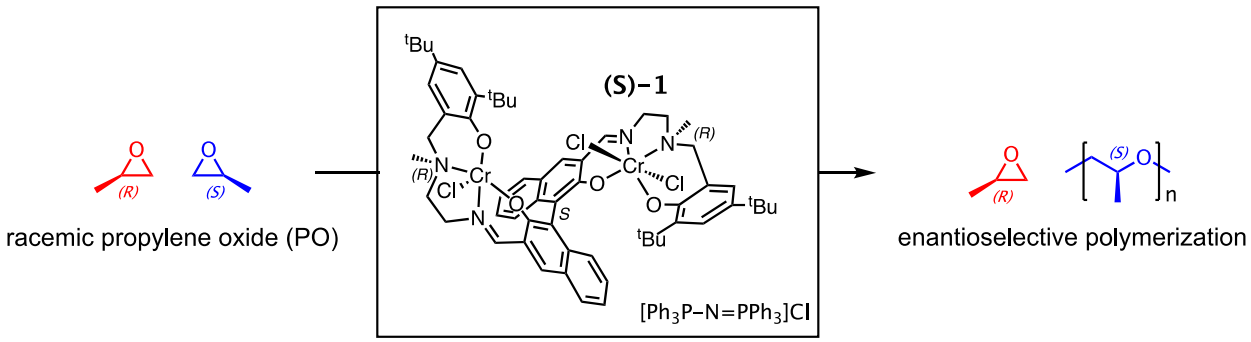

Figure 2.7: Kinetic resolution of PO polymerization by **(*S*)-1** for the synthesis of isotactic polypropylene oxide.

Many aspects of the catalyst must be taken into consideration in order to construct a reasonable model. Prior to polymerization, the catalyst must be activated by the cocatalyst, [PPN]Cl. Therefore the precatalyst for polymerization is proposed to be a trihalide version of ***rac*-2** where [PPN]Cl has donated its chloride to ***rac*-2**. For these simulations, the ***(S)*-2** version of ***rac*-2** is used, and its mirror image represents the ***(R)*-2** catalyst present in the racemic mixture. This trihalide species allows two possible arrangements of the three chloride ligands, *exo-endo*/*exo* and *endo-endo*/*exo*, and four possible configurations of the two N-methyl substituents of the ligand in *R/R*, *R/S*, *S/R*, or *S/S* stereochemical configurations, for a total of 8 possible structures (see Figures 2.8 and 2.9). The simulations show that the *exo-endo*/*exo* structure with *R/R* N-methyl centers is the lowest energy geometry for ***(S)*-2**, being 1.2 kcal/mol lower than the next most stable structure. The catalyst prefers this configuration due to minimal steric interactions between the aminomethyl group and *endo*-chloride ligand within the catalytic cleft. Polymerization initiation and propagation mechanisms (Figure 2.11 and 2.12) support the *exo-endo*/*exo* chloride configuration due to the need for an open coordination site within the catalytic cleft. The *R/R* N-methyl stereochemistry also minimizes steric inter-actions of bound PO monomer and the ligand, which results in lower energies for intermediates and transition states along the reaction mechanisms shown. This lowest energy configuration was therefore chosen as the most likely precatalyst leading to polymerization, and is used for subsequent reactivity calculations.

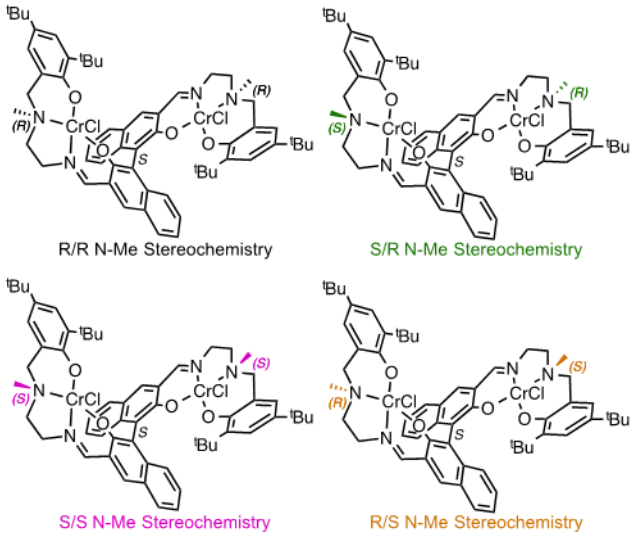

Figure 2.8: Possible stereoisomers of (S)-2 arising from amino-methyl configuration.

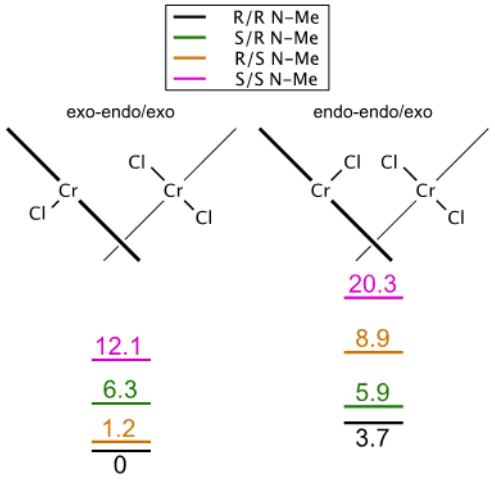

Figure 2.9: Possible conformations of (S)-2 after activation. Relative energies are in kcal/mol.

To provide details of the mechanism for initiation and propagation of polypropylene oxide (PPO), a slightly reduced catalyst model (Figure 2.10) was employed for subsequent computations. This model maintains all key features of the catalyst, and reproduces the major catalyst stereoselectivity features (vide infra).

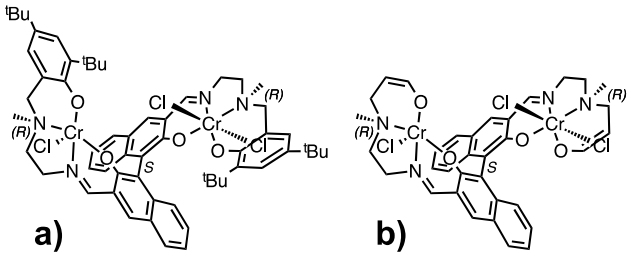

Figure 2.10: **a)** Full catalyst ***(S)*-2** after activation with *exo-endo*/*exo* chloride configuration and **b)** truncated model of the ***(S)*-2** catalyst.

Polymerization initiation is outlined in Figure 2.11. Starting from the *exo-endo*/*exo R*/*R* model catalyst (**C0**), an (*R*)- or (*S*)-PO monomer can coordinate to a coordination site at the endo position of one Cr center by displacing the Cr-Cl-Cr bridge (**R1** and **S1**). By backside attack of Cl on the nearest PO carbon to ring-open the PO, one Cr gains an open coordination site ($\mathbf{TS_{R1}}$ and $\mathbf{TS_{S1}}$). These processes occur in a single elementary step and have free energy barriers of 10.4 kcal/mol for (*S*)-PO and 15.3 kcal/mol for (*R*)-PO. Therefore the initiation step for PPO growth at the model **(*S*)-2** precatalyst prefers to occur with (*S*)-PO by the significant margin of 4.9 kcal/mol.

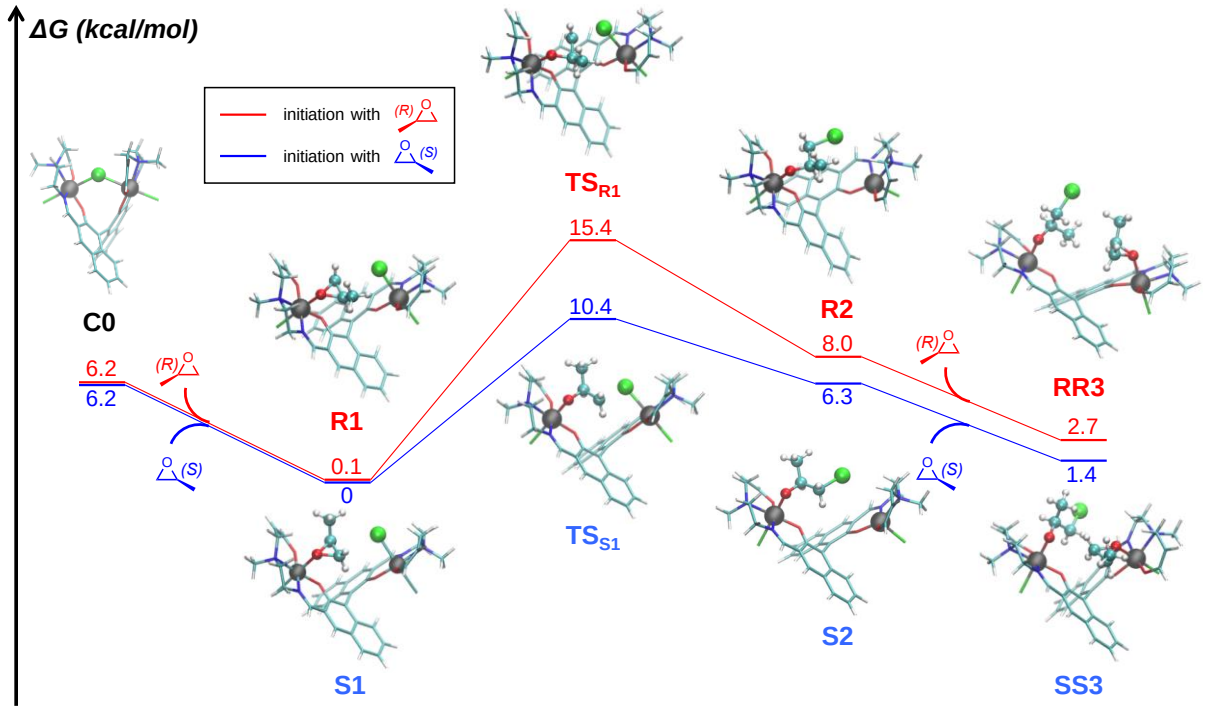

Figure 2.11: Free energy profile of initiation of chain growth at the truncated trihalide model ((S)-2) with *(R)*-PO and *(S)*-PO monomers.

From the (*S*)-initiated catalyst, a second (*R*)- or (*S*)-PO can coordinate to the open Cr site. (*S*)-PO binds more strongly, by 4.9 kcal/mol compared to 1.9 kcal/mol (**SS3** and **RS3**, respectively, Figure 2.12), indicating a continued preference for (*S*)- PO at ***(S)-2***. In this species, attack of the newly coordinated (*S*)-PO by the adjacent polymer alkoxide end group extends the polymer chain with a barrier of 25.7 kcal/mol via $\mathbf{TS_{SS3}}$. In contrast, (*R*)-PO has a higher barrier of 29.7 kcal/mol for insertion via $\mathbf{TS_{RS3}}$. This selectivity for (*S*)-PO polymerization is anticipated to persist as the chain grows. The catalyst stereoselectivity for (*S*)-PO is largely determined by the local environment surrounding the newly bound monomer and includes the most recently inserted monomer. The rest of the growing polymer extends away from the interior catalytic cleft and does not greatly influence stereoselectivity (**SS4** and **RS4** of Figure 2.12).

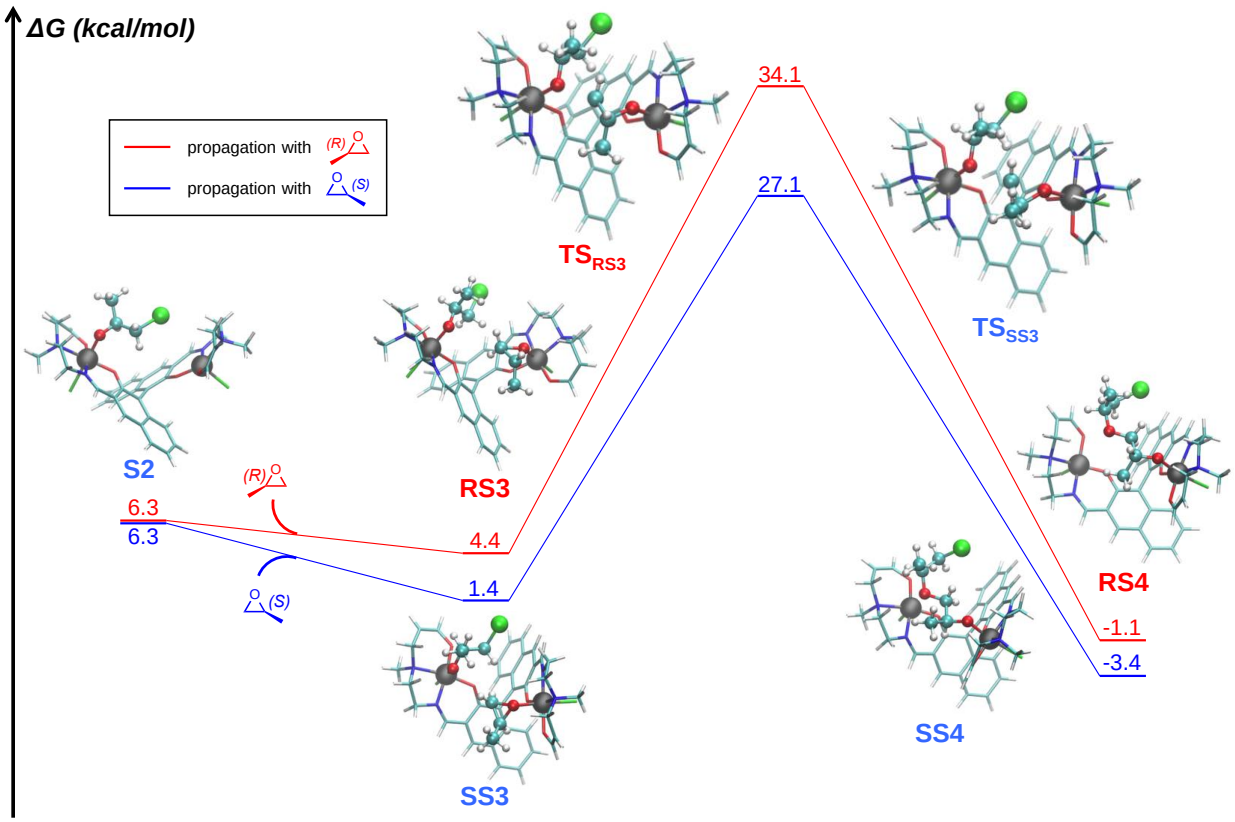

Figure 2.12: Free energy profile of chain growth using (*R*)-PO and (*S*)-PO monomers starting from the (*S*)-PO initiated polymer chain.

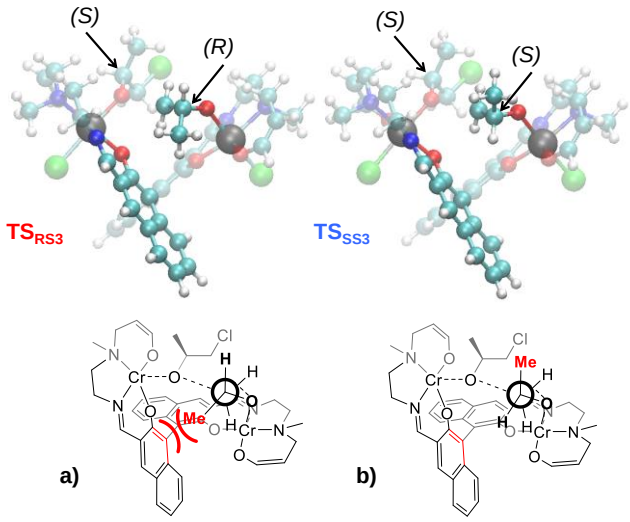

Figure 2.13: Stereochemical model for propagation transition states for **a)** (*R*)-PO and **b)** (*S*)-PO after initiation using (*S*)-PO.

These atomistic simulations also provide a 3D structural explanation for the observed stereoselectivity of catalysis. As shown in Figure 2.13, the (*R*)- and (*S*)-monomers take different orientations for their methyl groups at the chain growth steps, $\mathbf{TS_{RS3}}$ and $\mathbf{TS_{SS3}}$. Via Newman projections, it can be seen that the methyl group of (*R*)-PO sterically clashes with the proxi-mate naphthyl group of model (*S*)-2. This interaction causes a shift to a higher energy, less preferred transition state geometry compared to (*S*)-PO insertion. In (*S*)-PO insertion $\mathbf{TS_{SS3}}$, the same methyl position is replaced by hydrogen, minimizing this unfavorable steric interaction and resulting in a barrier that is 4.0 kcal/mol lower than that of $\mathbf{TS_{RS3}}$.

2.4 Conclusions

Ultimately, this work helped to illustrate the observed enantioselectivity of the bimetallic chromium catalyst, **(*S*)-1**. Careful consideration of all possible catalyst spin states, stereoisomers, and regioisomers post-activation were needed to identify a realistic form of the catalyst and accurately calculate the catalyst's enantioselectivity. Using a realistic, truncated model, ***(S)-2***, initiation and propagation pathways for the polymerization of (*R*) and (*S*) propylene epoxide monomers were calculated. These calculations suggest that the "matching" (*S*) propylene oxide monomer is preferred to react by over 5 kcal/mol, resulting in the enantioselective polymerization. Visualizing transition states of the reacting monomers illustrated the unique catalytic cleft that is tuned for the (*S*) PO monomer. The transition state is destabilized when (*R*) propylene oxide is introduced to the catalytic cleft due to a steric clash between the mismatched monomer and catalyst. The high barrier for the mismatched monomer-catalyst results in a high barrier for polymerization and explains the observed catalyst enantioselectivity.

2.5 References

(1) Feng, H.; Lu, X.; Wang, W.; Kang, N.-G.; Mays, J. Block Copolymers: Synthesis, Self-Assembly, and Applications. *Polymers (Basel).* **2017**, *9* (12), 494.

(2) Hu, H.; Gopinadhan, M.; Osuji, C. O. Directed Self-Assembly of Block Copolymers: A Tutorial Review of Strategies for Enabling Nanotechnology with Soft Matter. *Soft Matter* **2014**, *10* (22), 3867.

(3) Mai, Y.; Eisenberg, A. Self-Assembly of Block Copolymers. *Chem. Soc. Rev.* **2012**, *41* (18), 5969.

(4) Kim, H.-C.; Park, S.-M.; Hinsberg, W. D. Block Copolymer Based Nanostructures: Materials, Processes, and Applications to Electronics. *Chem. Rev.* **2010**, *110* (1), 146–177.

(5) Deming, T. J.; Novak, B. M. Polyisocyanides Using $[(\eta^3\text{-}C_3H_5)Ni(OC(O)CF_3)]_2$: Rational Design and Implementation of a Living Polymerization Catalyst. *Macromolecules* **1991**, *24* (22), 6043–6045. https://doi.org/10.1021/ma00022a023.

(6) Deming, T. J.; Novak, B. M.; Ziller, J. W. Living Polymerization of Butadiene at Both Chain Ends via a Bimetallic Nickel Initiator. Preparation of Hydroxytelechelic Poly(Butadiene) and Symmetric Poly(Isocyanide-*b*-Butadiene-*b*-Isocyanide) Elastomeric Triblock Copolymers. *J. Am. Chem. Soc.* **1994**, *116* (6), 2366–2374.

(7) Bryan, Z. J.; McNeil, A. J. Conjugated Polymer Synthesis via Catalyst-Transfer Polycondensation (CTP): Mechanism, Scope, and Applications. *Macromolecules* **2013**, *46* (21), 8395–8405.

(8) Yokozawa, T.; Ohta, Y. Transformation of Step-Growth Polymerization into Living Chain-Growth Polymerization. *Chem. Rev.* **2016**, *116* (4), 1950–1958.

(9) Leone, A. K.; McNeil, A. J. Matchmaking in Catalyst-Transfer Polycondensation: Optimizing Catalysts Based on Mechanistic Insight. *Acc. Chem. Res.* **2016**, *49* (12), 2822–2831.

(10) Verheyen, L.; Leysen, P.; Van Den Eede, M. P.; Ceunen, W.; Hardeman, T.; Koeckelberghs, G. Advances in the Controlled Polymerization of Conjugated Polymers. *Polym. (United Kingdom)* **2017**, *108*, 521–546.

(11) He, W.; Patrick, B. O.; Kennepohl, P. Identifying the Missing Link in Catalyst Transfer Polymerization. *Nat. Commun.* **2018**, *9* (1), 3866.

(12) Lu, L.; Zheng, T.; Wu, Q.; Schneider, A. M.; Zhao, D.; Yu, L. Recent Advances in Bulk Heterojunction Polymer Solar Cells. *Chem. Rev.* **2015**, *115* (23), 12666–12731.

(13) Holliday, S.; Li, Y.; Luscombe, C. K. Recent Advances in High Performance Donor-

Acceptor Polymers for Organic Photovoltaics. *Prog. Polym. Sci.* **2017**, *70*, 34–51.

(14) Pollit, A. A.; Obhi, N. K.; Lough, A. J.; Seferos, D. S. Evaluation of an External Initiating Ni(II) Diimine Catalyst for Electron-Deficient π-Conjugated Polymers. *Polym. Chem.* **2017**, *8* (28), 4108–4113.

(15) Bridges, C. R.; Yan, H.; Pollit, A. A.; Seferos, D. S. Controlled Synthesis of Fully π-Conjugated Donor–Acceptor Block Copolymers Using a Ni(II) Diimine Catalyst. *ACS Macro Lett.* **2014**, *3* (7), 671–674.

(16) Pollit, A. A.; Bridges, C. R.; Seferos, D. S. Evidence for the Chain-Growth Synthesis of Statistical π-Conjugated Donor-Acceptor Copolymers. *Macromol. Rapid Commun.* **2015**, *36* (1), 65–70.

(17) Bridges, C. R.; McCormick, T. M.; Gibson, G. L.; Hollinger, J.; Seferos, D. S. Designing and Refining Ni(II)Diimine Catalysts Toward the Controlled Synthesis of Electron-Deficient Conjugated Polymers. *J. Am. Chem. Soc.* **2013**, *135* (35), 13212–13219.

(18) Quirk, R. P.; Pickel, D. L. Controlled End-Group Functionalization (Including Telechelics). In *Polymer Science: A Comprehensive Reference*; Elsevier, 2012; pp 351–412.

(19) Engels, H.-W.; Pirkl, H.-G.; Albers, R.; Albach, R. W.; Krause, J.; Hoffmann, A.; Casselmann, H.; Dormish, J. Polyurethanes: Versatile Materials and Sustainable Problem Solvers for Today's Challenges. *Angew. Chemie Int. Ed.* **2013**, *52* (36), 9422–9441.

(20) Shi, W.; McGrath, A. J.; Li, Y.; Lynd, N. A.; Hawker, C. J.; Fredrickson, G. H.; Kramer, E. J. Cooperative and Sequential Phase Transitions in *it*-Poly(Propylene Oxide)-*b*-Poly(Ethylene Oxide)-*b*-*it*-Poly(Propylene Oxide) Triblock Copolymers. *Macromolecules* **2015**, *48* (9), 3069–3079.

(21) McGrath, A. J.; Shi, W.; Rodriguez, C. G.; Kramer, E. J.; Hawker, C. J.; Lynd, N. A. Synthetic Strategy for Preparing Chiral Double-Semicrystalline Polyether Block Copolymers. *Polym. Chem.* **2015**, *6* (9), 1465–1473.

(22) Price, C. C.; Osgan, M. The Polymerization of L-Propylene Oxide 1. *J. Am. Chem. Soc.* **1956**, *78* (18), 4787–4792.

(23) Ahmed, S. M.; Poater, A.; Childers, M. I.; Widger, P. C. B.; LaPointe, A. M.; Lobkovsky, E. B.; Coates, G. W.; Cavallo, L. Enantioselective Polymerization of Epoxides Using Biaryl-Linked Bimetallic Cobalt Catalysts: A Mechanistic Study. *J. Am. Chem. Soc.* **2013**, *135* (50), 18901–18911.

(24) Widger, P. C. B.; Ahmed, S. M.; Coates, G. W. Exploration of Cocatalyst Effects on a Bimetallic Cobalt Catalyst System: Enhanced Activity and Enantioselectivity in Epoxide

Polymerization. *Macromolecules* **2011**, *44* (14), 5666–5670.

(25) Thomas, R. M.; Widger, P. C. B.; Ahmed, S. M.; Jeske, R. C.; Hirahata, W.; Lobkovsky, E. B.; Coates, G. W. Enantioselective Epoxide Polymerization Using a Bimetallic Cobalt Catalyst. *J. Am. Chem. Soc.* **2010**, *132* (46), 16520–16525.

(26) Peretti, K. L.; Ajiro, H.; Cohen, C. T.; Lobkovsky, E. B.; Coates, G. W. A Highly Active, Isospecific Cobalt Catalyst for Propylene Oxide Polymerization. *J. Am. Chem. Soc.* **2005**, *127* (33), 11566–11567.

(27) Ajiro, H.; Peretti, K. L.; Lobkovsky, E. B.; Coates, G. W. On the Mechanism of Isospecific Epoxide Polymerization by Salen Cobalt(III) Complexes: Evidence for Solid-State Catalysis. *Dalt. Trans.* **2009**, No. 41, 8828.

(28) Fast, A.; Esfandiari, N. M.; Blum, S. A. Small Number of Active Sites and Single-Locus Kinetics Revealed in (Salph)Co-Catalyzed Ethylene Oxide Polymerization. *ACS Catal.* **2013**, *3* (9), 2150–2153.

Chapter 3: Transmetalation Mechanism in Nickel(II)-Catalyzed Grignard Reactions

The following content is associated with the publication below.

- Vitek, A. K.; Leone, A. K.; McNeil, A. J.; Zimmerman, P, M. Spin-Switching Transmetalation at Ni Diimine Catalysts. *ACS Catal.*, **2018**, *8*, 3655-3666.

3.1 Abstract

Transmetalation is a ubiquitous transformation used for synthesizing organic molecules. In catalyst-transfer polymerization (CTP), conjugated monomers are polymerized using transmetalation of Grignard reagents to make versatile organic semiconductors such as poly(3-hexylthiophene). This study presents the complete mechanistic viewpoint for this transmetalation reaction, taking into consideration the catalyst electronic states, steric environment, and realistic models of each reagent. These quantum chemical results reveal that singlet-triplet crossing is routine in these transmetalation reactions, and switching between low-spin square planar and high-spin tetrahedral geometries naturally occurs during the catalytic cycle. In this cycle transmetalation preferentially occurs from a triplet state, but forces the metal center back into a singlet state after monomer addition. Furthermore, the relative preference of singlet vs. triplet state can be modulated by the ancillary ligand. This model therefore captures reactive and ancillary ligand interactions and demonstrates how the relative distortion of the tetrahedral and square planar geometries can be used to quantify these sensitive ligand effects on the electronic state. Additionally, the activation barriers for transmetalation follow trends dictated by steric environment and the lateness of the transition state, measured in terms of the Ni-C bond distance. Together, these models provide predictive insight into ancillary ligand-based reactivity trends.

3.2 Introduction

Transition-metal mediated reactions such as Kumada cross-couplings are versatile synthetic tools for generating carbon-carbon bonds.[1] Despite their ubiquity, the mechanism of the transmetalation step is only partly understood, and there is no detailed, predictive model for how and why ligand modifications modulate reactivity.[2] For instance, catalyst-transfer polymerization (CTP) is a powerful method for synthesizing conjugated polymers that typically employs group 10 transition metals paired with N-heterocyclic carbene (NHC), phosphine, or diimine ligands.[3,4] CTP provides many examples of how varying catalyst ancillary[5–9] and reactive ligands[10–13] changes reactivity,[14,15] which may be useful for manipulating reactions toward a variety of desirable outcomes.

McCullough[16] and Yokozawa[17] demonstrated that a Ni bisphosphine catalyst could synthesize poly(3-hexylthiophene) (P3HT) in a living, chain-growth manner via what is now referred to as CTP.[18–21] Since this discovery, CTP has evolved to encompass additional monomers and copolymer sequences (e.g., block copolymers,[22–26] and gradient copolymers[26,27]). Current research efforts focus on expanding the monomer scope and monomer/catalyst compatibility to permit the synthesis of higher performing materials for organic electronics.[14] The present article focuses on the first step of the CTP cycle (Scheme 1), transmetalation, to develop a mechanistic model that fully accounts for electronics (spin state) and steric effects (untruncated ancillary ligands, varying reactive ligands, and solvated Grignard reagents).

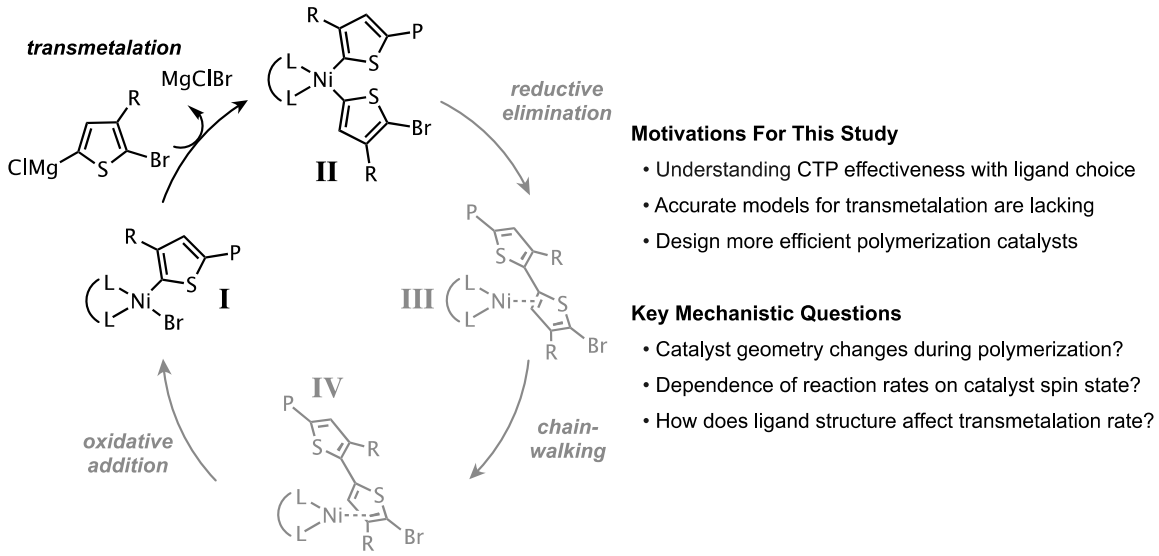

Figure 3.1 Proposed mechanism of propagation during CTP of 3-hexylthiophene. The emphasized transmetalation step (**I→II**) is the focus of this work.

The postulated CTP mechanism follows four steps: transmetalation, reductive elimination, chain-walking, and oxidative addition (Figure 3.1). Propagation from LNiBr(thiophene) (**I**) begins with monomer transmetalation, generating a bisthiophene Ni complex (**II**). Complex **II** undergoes reductive elimination to form a π-bound Ni-bisthiophene complex (**III**). The catalyst then migrates to the halide terminus of the polymer chain (**IV**) via chain-walking. The cycle is completed by intramolecular oxidative addition, regenerating **I**.

Mechanistic analyses of CTP have shown that monomer and catalyst steric and electronic properties regulate the rate-determining step, as well as the regioregularity, molecular weight, and dispersity of the resulting polymer.[20] For example, increasing the steric properties of the Grignard monomer dramatically decreases its transmetalation rate when Ni bisphosphine catalysts were used.[13,28,29] A fundamental understanding of the interactions between the ancillary and reactive ligands is expected to enable systematic design of new catalysts for CTP.

Quantum chemical simulations can provide a high level of detail to help explain reactivity on an atomistic level. Despite several theoretical studies of transition-metal-mediated polymerizations,[10,30–33] the transmetalation step has remained insufficiently characterized for CTP catalysts. In related reactions, efforts at modeling iron-catalyzed coupling reactions have suggested roles for multiple oxidation states,[34–36] complexities in explicit solvation,[37] and the possibility of spin state changes.[36,38] For Ni-catalyzed cross-coupling, these complexities may exist but no reports are available.[39] Herein we present a thorough quantum chemical investigation of transmetalation during initiation and propagation for polymerizing thiophene via Ni diimine catalysts. This study reveals: 1. The spin state changes during catalysis, which results in catalytically active tetrahedral and square planar geometries, and 2. The structure-activity relationship between ligand sterics and activation energies for Grignard transmetalations to Ni diimine catalysts. These mechanistic details should be informative for designing alternative catalysts where transmetalation is vital, including but not limited to CTP.

3.3 Results and Discussion

The present investigation focuses on transmetalation steps beginning with (diimine)$NiBr_2$ precatalysts to demonstrate how electronic states change during this transformation. Diimine-ligated Ni catalysts have polymerized conjugated monomers[29,40–43] and are well known for α-olefin polymerization,[44–51] making them an important ligand class for mechanistic studies.

Specific to this study, complex L^1NiBr_2 has been used in olefin polymerizations[44–48] and recently demonstrated the ability to generate olefin/thiophene block copolymers.[52] Herein, L^1NiBr_2 catalyst is compared to a sterically more demanding analogue, L^2NiBr_2 (Figure 3.2). These two catalysts differ by a single methyl group that is proximate to the metal center, which will be shown to result in significant changes in spin equilibria and transmetalation rate. Inspired by prior successes in elucidating complicated reactivity,[53–60] the reaction discovery tools developed by the Zimmerman group were used to guide this study.[61–65]

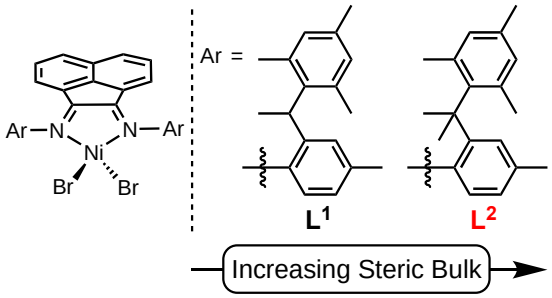

Figure 3.2: Ni diimine precatalysts under consideration.

Starting from a $LNiBr_2$ precatalyst, the CTP mechanism involves three transmetalation reactions each differing by a single reactive ligand (Figure 3.3). From **TM1** to **TM3**, steric and electronic effects of the reactive ligands change simultaneously and significantly. **TM1** involves a thiophene monomer replacing a bromide of $LNiBr_2$, forming LNiBr(thiophene). Subsequently, a second monomer replaces the remaining Br in **TM2** to form $LNi(thiophene)_2$. Reductive elimination (**II→III**), followed by chain-walking (**III→IV**) and oxidative addition (**IV→I**) results in LNiBr(dithiophene). Transmetalation of a third monomer results in LNi(thiophene)(dithiophene), allowing the sequence **II→III→IV→I** to repeat.

The computational study of **TM1**–**TM3** uncovered a particular sensitivity of these reactions to the ancillary ligand and the reactive ligand. To begin explaining these effects, the spin state of the transition metal complex is examined, with an emphasis on demonstrating how ancillary/reactive ligand combinations dictate Ni's preferred spin state. After elucidating these complexities, the finer details of the transmetalation reactions will be discussed thoroughly.

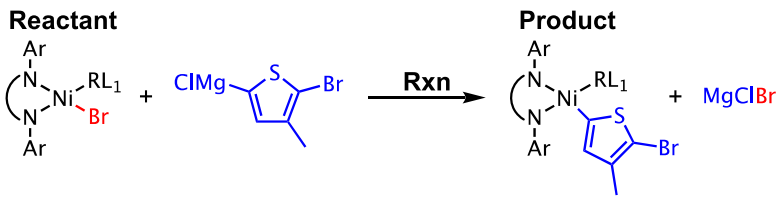

RL_1	Rxn	Reactant	Product
Br	**TM1**	$LNiBr_2$	LNiBr(thiophene)
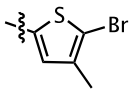	**TM2**	LNiBr(thiophene)	$LNi(thiophene)_2$
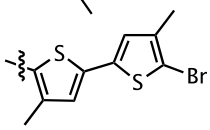	**TM3**	LNiBr(dithiophene)	LNi(dithiophene) (thiopehene)

Figure 3.3: Transmetalation reactions under consideration (RL = reactive ligand).

3.4 Ligand Control of Spin State

In **TM1**–**TM3**, Ni is in the +2 oxidation state, allowing square planar and tetrahedral geometries. Square planar geometries are most stable in a low-spin configuration (S0) and tetrahedral geometries are typically high spin (T1).[66] Quantum chemical simulations show that the two $LNiBr_2$ precatalysts favor high-spin, tetrahedral geometries by ≥10 kcal/mol (Figure 3.4 c). These predictions agree with single-crystal X-ray diffraction data for L^1NiBr_2,[44] and are corroborated by the weak crystal-field splitting of the Br ligands.[67] In contrast, $LNi(thiophene)_2$ complexes are more stable in the low-spin, square planar geometries, by >13 kcal/mol, due to the stronger field effect of the thiophene reactive ligands.[68] When the LNi complexes contain one Br and one thiophene reactive ligand, the spin state varies based on the ancillary ligand. Less sterically demanding L^1 results in a low-spin square planar geometry whereas the more sterically demanding L^2 entails a high-spin tetrahedral geometry (Figure 3.4 c). To within the capabilities of quantum chemical methods (see section A.24 in Appendix A), the spin gaps (–4.5 to 2.1 kcal/mol) suggest an equilibrium between the two electronic states is feasible for LNi(thiophene)Br.

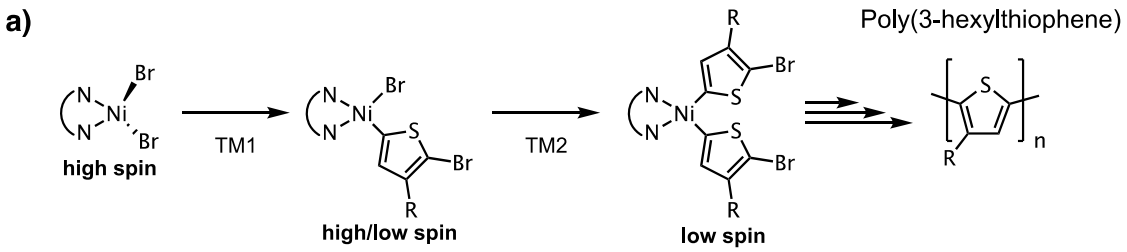

c)

	ΔG = G(S0)-G(T1) (kcal/mol)		
Ligand	$LNiBr_2$	LNiBr (thiophene)	LNi $(thiophene)_2$
L^1	13.6	-4.5	-13.2
L^2	10.0	2.1	-15.4

Figure 3.4: **a)** Transmetalation-induced spin-state switch during initiation, **b)** Equilibrium between square planar and tetrahedral Ni complexes, and **c)** Computed S0 versus T1 energy gap for initiation intermediates where ΔG=G(S0)-G(T1).

The predicted spin-state changes were experimentally supported using ^{1}H NMR spectroscopy. As anticipated for a high-spin, tetrahedral Ni(II) complex, precatalyst L^1NiBr_2 exhibits paramagnetic resonances between –20 and –40 ppm (Figure 3.5). Additionally, the resonances shift linearly in response to temperature (–5 to 30 °C), demonstrating that L^1NiBr_2 follows Curie's law, and providing support for its paramagnetic nature (see Figure 5.11 and 5.12 in Appendix A). L^1NiBr(thiophene) was generated *in situ* by adding thiophene Grignard (1 equivalent) to L^1NiBr_2. The resulting ^{1}H NMR spectrum shows a significant loss of paramagnetic resonance intensity with concomitant formation of sharp peaks between 0 and 10 ppm, suggesting that L^1NiBr(thiophene) is low-spin and square planar. To confirm a change in spin state upon transmetalation, Evan's method[69,70] using THF-d_8 as a standard was employed to analyze the presence (or absence) of a THF-d_8 peak shift. In the ^{1}H NMR spectrum of L^1NiBr_2, a THF-d_8 peak shift of 0.43 ppm is observed, consistent with a paramagnetic species. Subsequent transmetalation generates L^1NiBr(thiophene), where the disappearance of the THF-d_8 peak shift suggests a low-spin square planar geometry. These NMR spectroscopic data are in good agreement with the prediction that the nickel center switches from high-spin to low-spin when transforming from L^1NiBr_2 to L^1NiBr(thiophene).[71]

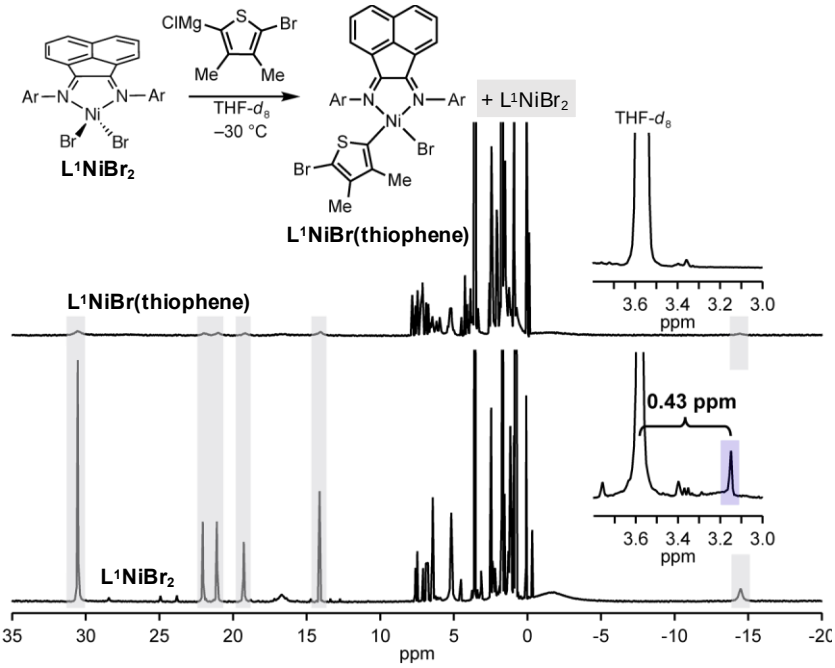

Figure 3.5: ^{1}H NMR spectra supporting the predicted high- and low-spin states for $L^{1}NiBr_2$ and $L^{1}NiBr$(thiophene) using Evan's method by Amanda Leone.[72]

Next, the square planar and tetrahedral geometries were evaluated in greater detail to reveal how ancillary ligands affect the steric and electronic environment around the metal center (Figure 3.6). Specifically, the $LNiBr_2$ and $LNi(thiophene)_2$ intermediates are analyzed because they represent the limiting cases of weak (i.e., Br) and strong field (i.e., thiophene) reactive ligands, as well as a range of steric bulk.

The $LNiBr_2$ geometries show that steric encumbrance distorts the positions of the Br reactive ligands (Figure 3.6). These Br reactive ligands rotate away from the axial positions of canonical, relaxed tetrahedral geometries (where $\alpha=\beta=90°$) by +15° and +35° in $L^{1}NiBr_2$ and $L^{2}NiBr_2$, respectively. Similarly, the $L^{2}Ni(thiophene)_2$ geometry demonstrates a twisted square planar geometry due to interference from the gem-dimethyl groups of L^{2}. In contrast, $L^{1}Ni(thiophene)_2$ with its monomethyl groups shows only minor distortions from a square planar geometry, suggesting that steric properties of the diimine ligand's Ni-facing groups significantly influence the stability of square planar and tetrahedral geometries. While this qualitatively explains that the ligand electronic and steric effects dictate Ni's spin state preference, the trends in spin gap (Figure 3.4 c) require a more quantitative explanation.

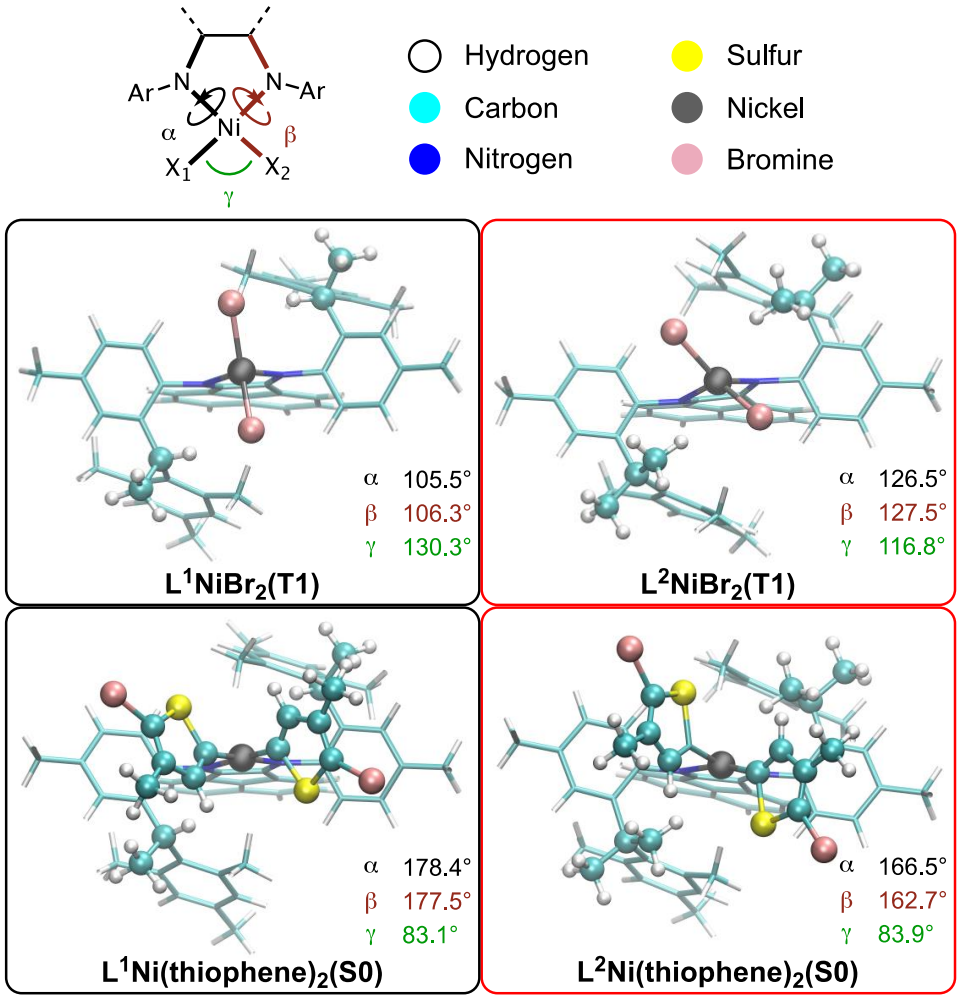

Figure 3.6: Geometries of $LNiBr_2$ and $LNi(thiophene)_2$. Geometries shown are precatalyst species adopting a high-spin, tetrahedral geometry (from top left to top right, $L^1NiBr_2(T1)$ and $L^2NiBr_2(T1)$) and bisthiophene complexes adopting a low-spin, square planar geometry (from bottom left to bottom right, $L^1Ni(thiophene)_2(S0)$ and $L^2Ni(thiophene)_2(S0)$).

To understand how L^1 and L^2 affect spin state stabilities, the full catalysts were compared to a model with truncated ancillary ligand scaffolds. The model system replaces the aryl pendant groups of each diimine ligand with a hydrogen atom (Figure 3.7 a), thus eliminating the steric effects of the diimine. This model therefore enables partitioning of the electronic and steric factors on each intermediate/spin state as follows. The electronic contributions represent the energetic costs to twist the ligands away from their favored positions (i.e., ideal square planar or tetrahedral) to the positions of the full catalyst, without including the steric-interaction energies between the reactive and ancillary ligands. The steric contributions are the difference between the electronic energy factors (i.e., distortion) and the total energetics of the full system. Overall,

this simple partitioning provides a quantitative viewpoint on the interplay between sterics and electronics on each catalytic intermediate.

This simple partitioning approach demonstrates that electronic distortions favor the low-spin, square planar geometry (Figure 3.7 b), which is expected as square planar structures tend to be less twisted than the tetrahedral structures (see Figure 3.6). Additionally, as reactive ligand torsional angles (α and β) diverge from those of the reference model, high-spin, tetrahedral geometries experience stronger destabilization per degree of displacement than low-spin, square planar geometries (see Figure 5.14 in Appendix A). The greater displacement of reactive ligands in the dimethylated ligand (L^2) therefore results in a stronger electronic effect, favoring the low-spin, square planar geometry.

The steric contributions, on the other hand, demonstrate that L^1 favors the low-spin, square planar geometry while L^2 favors the high-spin, tetrahedral geometry. This is fully consistent with the electronic contribution, as the mesityl groups of L^1 and L^2 introduce steric bulk to the axial regions of the nickel complexes and destabilize the high-spin, tetrahedral geometry. The two dimethyl groups of L^2 introduce additional steric bulk to the equatorial region, surpassing the mesityl's steric effect. Thus, the sterically encumbered L^2 has steric contributions that disfavor the low-spin, square planar structure, ultimately favoring the high-spin, tetrahedral configuration. This effect is most pronounced for $L^2Ni(thiophene)_2$, where the reactive ligands add additional interference with the gem-dimethyl groups.

a)

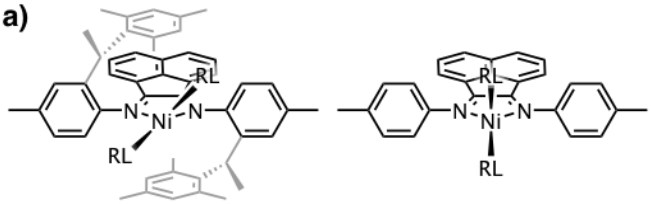

Full/Truncated Reference

b)

	$LNiBr_2$	LNiBr (thiophene)	LNi $(thiophene)_2$
Ligand	$\Delta H_{elec.}$**(S0) -** $\Delta H_{elec.}$**(T1)** (kcal/mol)		
L^1	-1.7	-7.1	-3.6
L^2	-5.9	-4.7	-6.5
	$\Delta H_{ster.}$**(S0) -** $\Delta H_{ster.}$**(T1)** (kcal/mol)		
L^1	-3.6	-2.8	-2.5
L^2	0.4	0.3	2.6

Figure 3.7: **a)** Depiction of full (left, grey), truncated (left, black), and reference (right) systems for catalytic intermediates. Distortion of reactive ligands caused by ancillary ligands is frozen in the truncated system. **b)** Enthalpies from electronic and steric contributions to the distortion of low-spin, square planar (S0) and high-spin, tetrahedral (T1) geometries.

The relative changes in steric and electronic effects (Figure 3.7) must be considered alongside the absolute values of spin gap for the model system. The reference complex in the dihalide intermediate has a singlet-triplet gap of 16.8 kcal/mol (see Table 5.1 in Appendix A). Thus, even the sum of steric and electronic changes incurred by the full ligand do not make the singlet state favored for $LNiBr_2$. Similarly, in the LNi$(thiophene)_2$, the ligand steric and electronic interactions cannot overcome the ligand field effect to produce a favorable triplet state. In the intermediate regime of the monohalide, monothiophene species, the ancillary ligand effect may be strong enough to affect the preferred spin state. Steric interactions between the thiophene and mesityl destabilize the tetrahedral geometries for both LNiBr(thiophene) complexes. The gem-dimethyl group of L^2, however, destabilizes the square planar L^2NiBr(thiophene) complex leading to L^1 favoring the singlet slightly more than L^2 when considering electronic distortion. The possibility that either the singlet or the triplet may be favored at this mixed reactive ligand species means that transmetalation could potentially occur from either electronic state. Therefore, the LNiBr(thiophene) structure—which is a key intermediate for CTP—will need to be examined in greater detail for its role in transmetalation.

3.5 Transmetalation Initiation Mechanism

To accurately model transmetalation, high- and low-spin transmetalation pathways were investigated for initiation (Figures 3.8-3.11) and propagation (Figure 3.12 and 3.13). In these pathways, the Grignard reagent was assumed to be disolvated (e.g., $(THF)_2MgCl(thiophene)$) based on experimental[73–75] and computational[76,77] evidence (see Figure 5.14 in Appendix A). Simulations show that high-spin pathways proceeding through tetrahedral nickel complexes have lower activation barriers than the analogous low-spin pathways (see Table 5.3 in Appendix A). For example, high-spin and low-spin pathways for transmetalation at the L^1NiBr_2 precatalyst are shown in Figure 3.8.

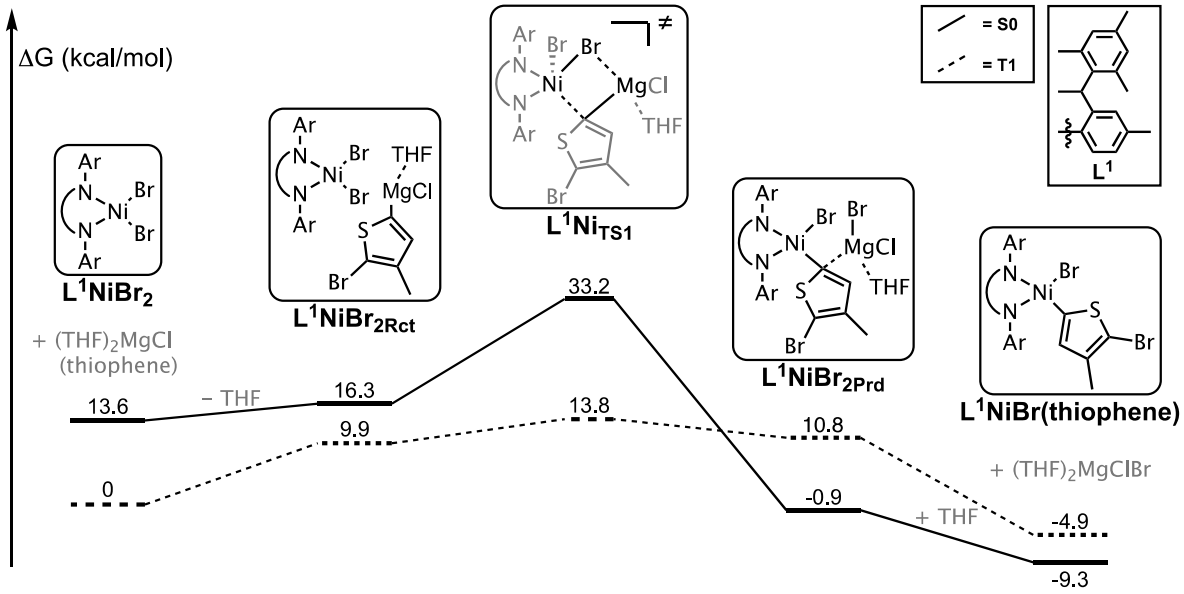

Figure 3.8: High-spin (dashed lines) and low-spin (solid lines) transmetalation pathways (**TM1**) for L^1NiBr_2. The reference energy is calculated from separated high-spin L^1NiBr_2 and $(THF)_2MgCl(thiophene)$.

The pathways in Figure 3.8 start from L^1NiBr_2 and $(THF)_2MgCl(thiophene)$. First, $(THF)_2MgCl(thiophene)$ eliminates a solvent molecule, generating a sterically accessible species capable of association to L^1NiBr_2, giving L^1NiBr_{2Rct}. Transmetalation occurs via a 4-membered transition state (L^1Ni_{TS1}), where (THF)MgCl(thiophene) exchanges thiophene for a Br reactive ligand, forming L^1NiBr_{2Prd}. Binding of a THF solvent molecule to (THF)MgClBr enables magnesium salt dissociation from the resulting $L^1NiBr(thiophene)$. This high-spin transmetalation pathway (**TM1**) has a barrier that is 19.4 kcal/mol below the low-spin pathway.

The final product of **TM1**, however, favors the low-spin geometry by 4.4 kcal/mol. The spin state therefore changes after the transition state while (THF)MgClBr remains associated with the Ni complex.

The analogous transmetalation pathway with L^2NiBr_2 also favors the high-spin state, as do all pathways for **TM2** and **TM3** (see Table 5.3 in Appendix A). As such, only the high-spin pathway is discussed for subsequent transmetalation reactions. The $LNiBr(RL_{Rct})$ and $LNiBr(RL_{Prd})$ intermediates (RL = Br, thiophene, or dithiophene) are implied but not explicitly shown in the following PESs, as their existence and behavior is similar for all subsequent reaction steps (Figures 3.9, 3.10, and 3.12). For the **TM1** pathways involving L^1 or L^2 (Figure 3.9), L^2NiBr_2 initiation has a 1.1 kcal/mol higher barrier than L^1NiBr_2 and prefers the high-spin state post-transmetalation.

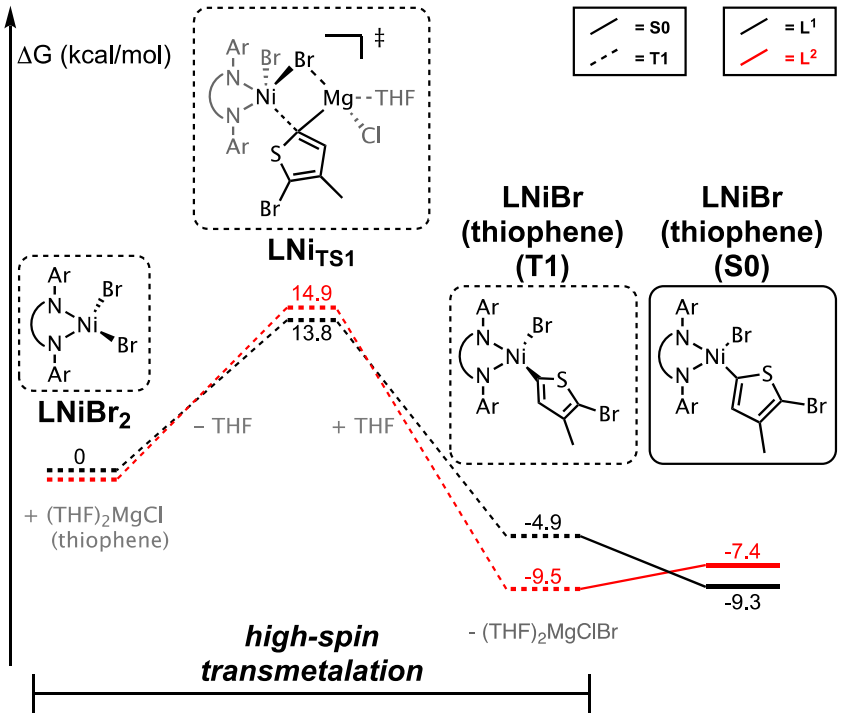

Figure 3.9: PES of the **TM1** transmetalation reaction for $LNiBr_2$ precatalysts.

The second transmetalation reaction (**TM2**) illustrates reactive and ancillary ligand interactions, producing a broader range of barrier heights (Figure 3.10) than **TM1**. **TM1** barriers are relatively low because Br reactive ligands are less sterically demanding than thiophene. Additionally, L^2 produces a higher barrier (18.0 kcal/mol) than L^1 (12.0 kcal/mol) due to the

added steric bulk of the L^2 gem-dimethyl group. Grignard loss and rearrangement to a square-planar geometry give LNi(thiophene)$_2$, which now strongly favors the low-spin state with both ligands. This spin switch entails a strongly exergonic reaction (>15 kcal/mol downhill) to complete initial transmetalations.

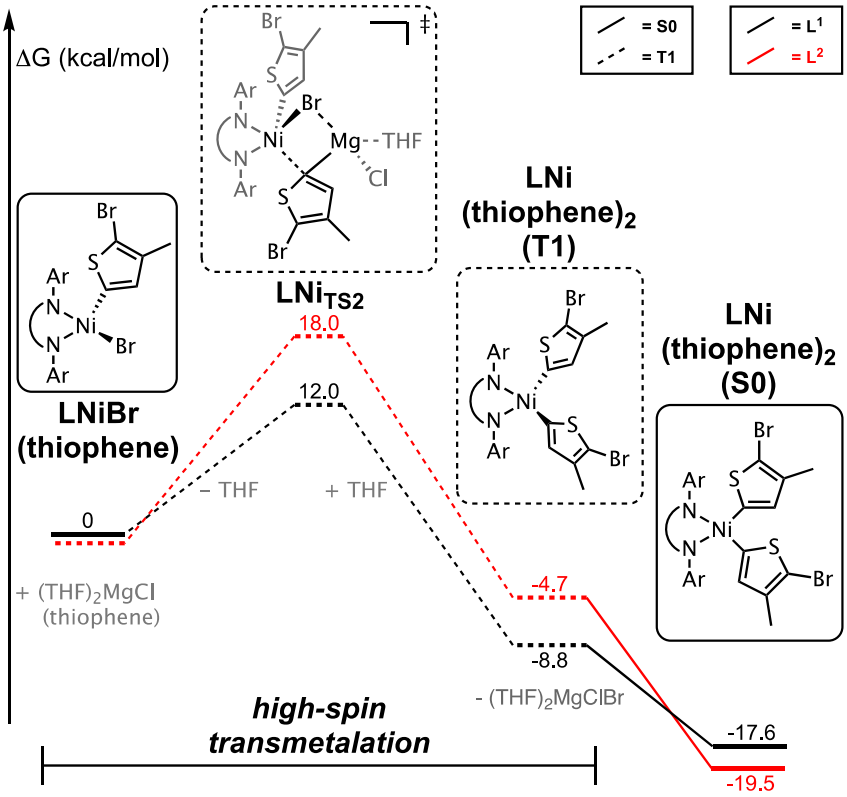

Figure 3.10: PES of the **TM2** transmetalation reaction of LNiBr(thiophene) catalytic intermediates.

As steric bulk around the metal center increases from **TM1** to **TM2**, the transmetalation transition states become more geometrically strained. Similarly, transition states with L^2 will be more strained than L^1. To quantify these effects, the Ni–C bond distance ($\mathbf{d_{Ni\text{-}C}}$), which measures the degree that thiophene is bonded to the metal center, is examined for these transition states. For **TM2**, the crowded L^2 ligand indeed features a more strained $\mathbf{d_{Ni\text{-}C}}$ bond compared to for the L^1 ligand (2.91 Å (L^2) versus 3.01 Å (L^1)), Figure 3.11). When comparing **TM2** transition state geometries (Figure 3.11) to those of **TM1** (see Figure 5.16 in Appendix A), $\mathbf{d_{Ni\text{-}C}}$ for L^2 contracts by ~0.1 Å from **TM1** to **TM2**. In contrast, $\mathbf{d_{Ni\text{-}C}}$ for the L^1 ligand remains largely unchanged (+0.02 Å from **TM1** to **TM2**) due to its low steric encumbrance compared to L^2. Therefore, as the reactive ligands' steric bulk increases (from **TM1** to **TM2**) and the ancillary ligand bulk

increases (from L^1 to L^2), both $\mathbf{d_{Ni\text{-}C}}$ contraction and higher transmetalation barriers are observed. This effect shows that sterically bulkier ligands—both ancillary and reactive—correspond to later transition states.

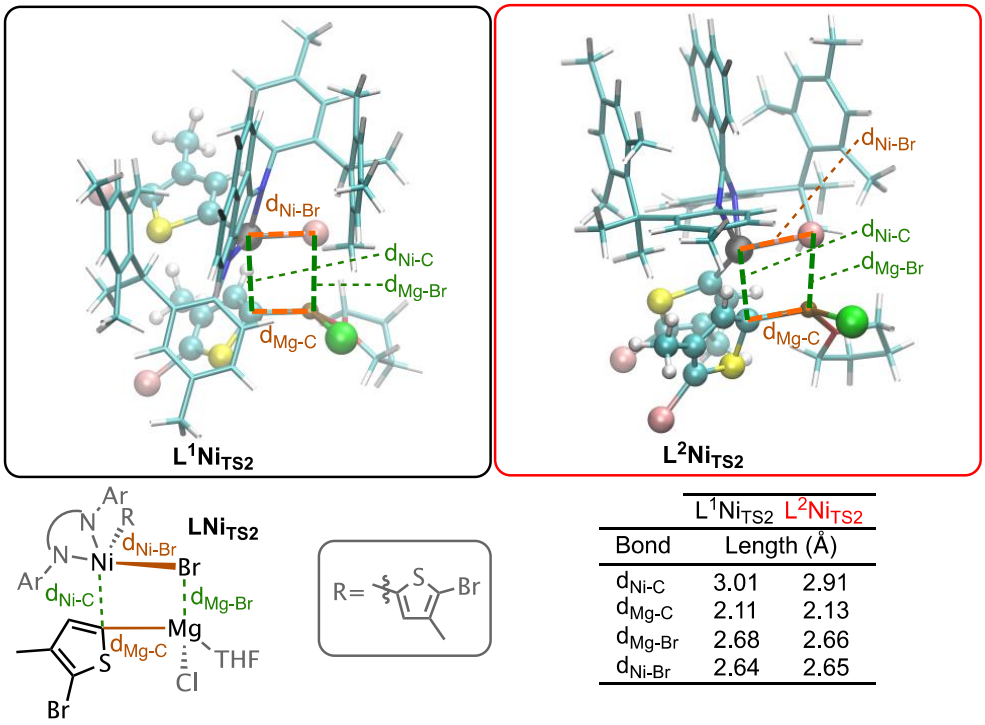

	L^1Ni_{TS2}	L^2Ni_{TS2}
Bond	Length (Å)	
$d_{Ni\text{-}C}$	3.01	2.91
$d_{Mg\text{-}C}$	2.11	2.13
$d_{Mg\text{-}Br}$	2.68	2.66
$d_{Ni\text{-}Br}$	2.64	2.65

Figure 3.11: Transition state geometries of **TM2** reactions at LNiBr(thiophene) catalytic intermediates showing bonds broken (orange) and bonds formed (green) during the reaction.

3.6 Transmetalation Propagation Mechanism

Propagation begins with the third transmetalation step, **TM3** (Figure 3.12). Similar to **TM2**, L^2NiRL_2 demonstrates a higher barrier than $L^1NiBrRL_2$ (c.f., 7.2 kcal/mol). The increased bulk of dithiophene relative to thiophene entails higher barriers for both ancillary ligands when compared to **TM2**: 1.5 kcal/mol (L^1) and 2.7 kcal/mol (L^2). Similar to the **TM2** initiation step, **TM3** results in a low-spin square planar LNi(thiophene)$_2$ product.

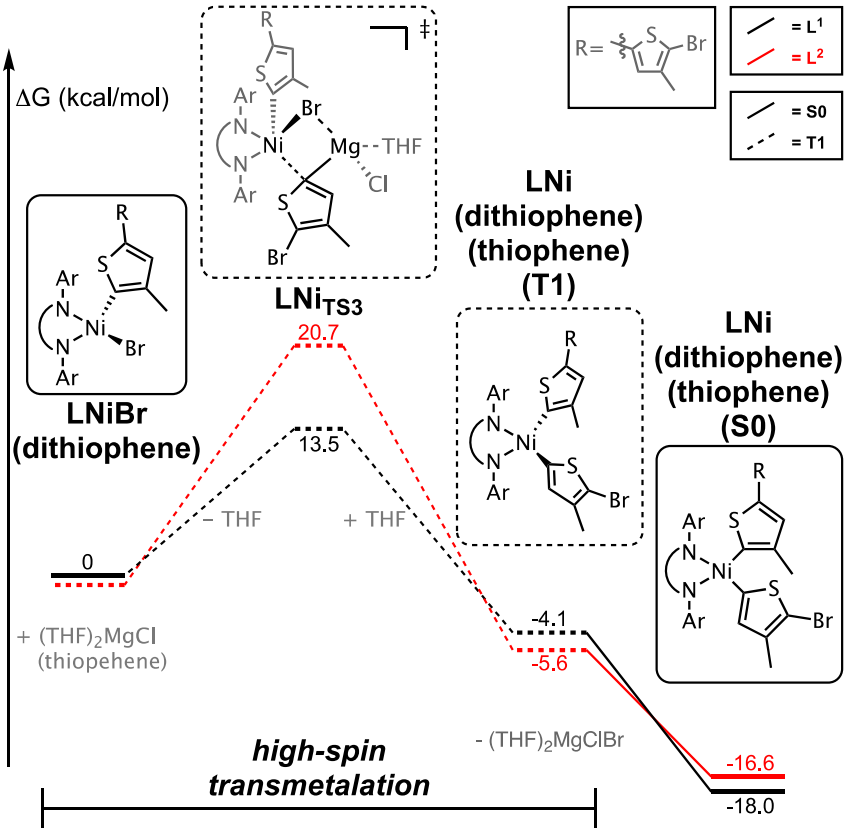

Figure 3.12: PES of the **TM3** transmetalation reaction of LNiBr(dithiophene) catalytic intermediates.

The most distinct difference between **TM3** transition state geometries (Figure 3.13) and those from **TM2** (Figure 3.11) are the shortened Ni–C distances ($\mathbf{d_{Ni\text{-}C}}$). Specifically, $\mathbf{d_{Ni\text{-}C}}$ in **TM3** are shorter than in **TM2**, a similar trend was observed comparing **TM2**'s $\mathbf{d_{Ni\text{-}C}}$ to **TM1** (see Figure 5.16 in Appendix A). In total, the average $\mathbf{d_{Ni\text{-}C}}$ contraction of >0.3 Å from **TM1** to **TM3** demonstrates how increased steric strains result in later transition states, and overall higher barriers for transmetalation compared to **TM1**.

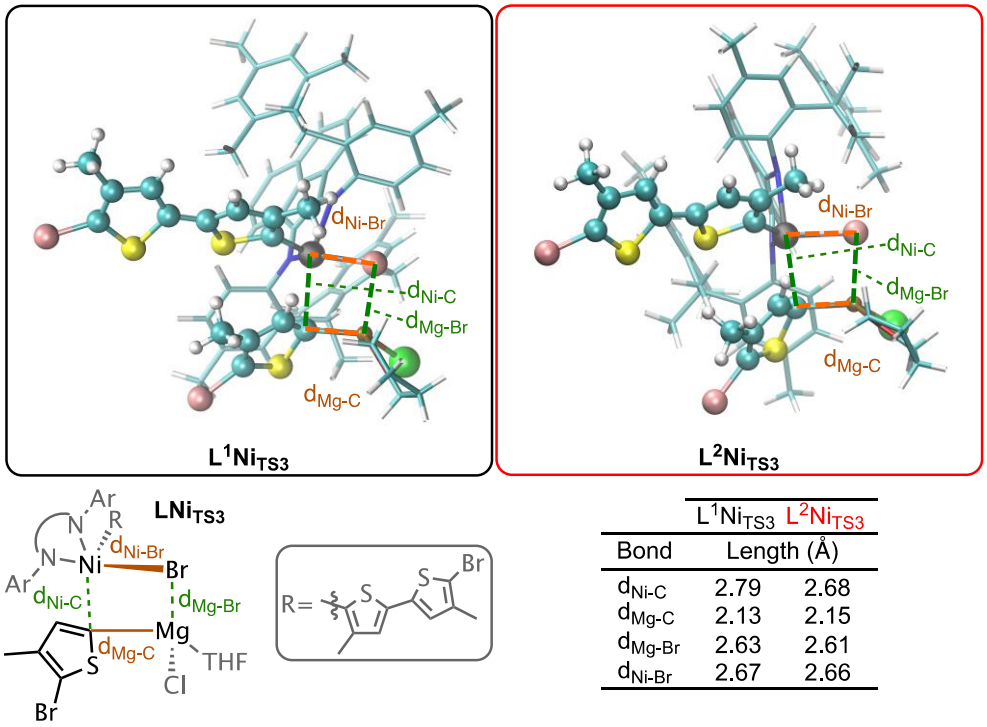

Bond	L^1Ni_{TS3} Length (Å)	L^2Ni_{TS3} Length (Å)
d_{Ni-C}	2.79	2.68
d_{Mg-C}	2.13	2.15
d_{Mg-Br}	2.63	2.61
d_{Ni-Br}	2.67	2.66

Figure 3.13: Transition state geometries for transmetalation reactions (**TM3**) of the LNiBr(dithiophene) intermediates showing bonds broken (orange) and bonds formed (green) during the reaction.

Combined, these results demonstrate how small changes in the reactive and ancillary ligands (methyl versus gem-dimethyl) significantly influence transmetalation barriers for initiation and propagation. Assuming transmetalation is rate-determining during these polymerizations, L^1Ni and L^2Ni are expected to demonstrate significantly different polymerization characteristics. For example, initiation for L^1NiBr(thiophene) would be ~1,400 times faster than L^2NiBr(thiophene) and propagation with L^1NiBr(dithiophene) would be ~200,000 times faster (at room temperature) than with L^2NiBr(dithiophene), which could significantly influence the resulting polymer's molecular weight and dispersity.[11] These rates can be traced to differences in lateness of the transition states for **TM1**–**TM3**, as dictated by the steric environment around the metal center. As the reactive and ancillary ligands substantially influence spin-state energetics (e.g., Figure 3.7), transmetalation barriers must be evaluated at both high- and low-spin pathways. In the example of this study, if one incorrectly assumes a singlet manifold, activation barriers could be misleading by ~20 kcal/mol.

3.7 Conclusion

Ni diimine complexes provide a compelling model system for studying transmetalation reactions, as they demonstrate a range of chemically specific details that tune reactivity. This study evaluated transmetalation of C(sp^2) Grignard reagents that have high relevance for electronic material development,[24,25] where the factors affecting these reactions will likely be important in many other transition-metal-mediated coupling reactions. These factors—which include changing spin states over the catalytic cycle and strong steric effects in the ligands (both ancillary and reactive)—provide a qualitatively new description of transmetalation reactions for Ni diimine complexes.

This study's explanation of ligand-dependent spin-state gaps is especially pertinent to designing catalytic systems involving transmetalation at Ni. As the transmetalations investigated in this study occur exclusively from the high-spin state in $LNiRL_2$ complexes, tailoring conditions for these reactions should take into account factors that affect the relative energies of each spin state, which can be metal-, ligand-, monomer-, and halide-dependent. In this study, it was shown that these factors can be quantified using relative displacements from idealized tetrahedral and square planar structures (i.e., Figure 3.7). For the class of diimine ligands (e.g., L^1 and L^2) the switch in spin state during Kumada coupling also indicates that one should take into account the catalyst binding-pocket formed by the tetrahedral geometry during transmetalation, while additionally accounting for the square planar geometry when the two reactive ligands are organic. The distortion model presented herein provides an initial indication of what is advantageous (e.g., L^1), and what should be avoided (e.g., L^2), in designing these complexes.

3.8 Experimental Details

L^1NiBr_2: An aliquot of an **L^1NiBr_2** stock solution (0.0226 M in THF-d_8, 0.25 mL) was transferred to a screw-cap NMR tube. An NMR tube insert containing THF-d_8 was placed in the screw-cap NMR tube, which was sealed with a Teflon cap and electrical tape, then removed from the glovebox for NMR spectroscopic analysis (see Figure 5.5 in Appendix A).

L^1NiBr(thiophene): Freshly prepared **L^1NiBr_2** stock solution (0.0226 M in THF-d_8, containing 10.9 mg, 0.0125 mmol, 1.00 equiv) was cooled to –30 °C for 5 min. Then, freshly prepared (5-bromo-3,4-dimethylthiophen-2-yl)magnesium chloride (SI3) (cooled to –30 °C for 5 min, 0.095 M in THF-d_8, 138 µL, 0.0125 mmol, 1.00 equiv) was added dropwise to the **L^1NiBr_2** solution.

The solution immediately changed from red to blue at which time it was moved to the –30 °C freezer for 2 min. Then, an aliquot of the blue solution (0.25 mL) was transferred to a screw cap NMR tube. An NMR tube insert (see Figure 5.5 in Appendix A) containing THF-d_8 was placed in the screw-cap NMR tube, which was sealed with a Teflon cap and electrical tape and removed from the glovebox for NMR spectroscopic analysis. Spectroscopic analysis revealed complete consumption of **SI3** (indicated by absence of singlets at 2.19 and 1.17 ppm) as well as minimal unreacted $\mathbf{L^1NiBr_2}$ (indicated by broad peaks > 10 ppm, see Figure 5.8 in Appendix A).

3.9 Computational Details

Investigation of the thiophene polymerization pathway used a combination of reaction mechanism discovery methods developed by the Zimmerman group. All initial geometries for intermediates and transition states were obtained using the unrestricted framework and in the gas phase and using the B3LYP density functional[80–83] and LANL2DZ basis set and corresponding effective core potentials.[84–86] Energies for initial geometries were refined by applying the ωB97X density functional,[87] the cc-pVDZ[88] and cc-pVTZ basis sets,[88–91] and the SMD implicit solvent model.[92–94] All energies listed are Gibbs free energies with enthalpy and entropy corrections, and all geometries were confirmed to have the appropriate number of imaginary frequencies. See the Appendix A for a more detailed description of the computational methods and comparison of the reported results to other density functionals and coupled-cluster.

3.10 References

(1) Heravi, M. M.; Hajiabbasi, P. Recent Advances in Kumada-Tamao-Corriu Cross-Coupling Reaction Catalyzed by Different Ligands. *Monatshefte fur Chemie* **2012**, *143* (12), 1575–1592.

(2) Harvey, J.; Poli, R.; Smith, K. M. Understanding the Reactivity of Transition Metal Complexes Involving Multiple Spin States. *Coord. Chem. Rev.* **2003**, *238–239*, 347–361.

(3) Bryan, Z. J.; McNeil, A. J. Conjugated Polymer Synthesis via Catalyst-Transfer Polycondensation (CTP): Mechanism, Scope, and Applications. *Macromolecules* **2013**, *46* (21), 8395–8405.

(4) Verheyen, L.; Leysen, P.; Van Den Eede, M. P.; Ceunen, W.; Hardeman, T.; Koeckelberghs, G. Advances in the Controlled Polymerization of Conjugated Polymers. *Polym. (United Kingdom)* **2017**, *108*, 521–546.

(5) Bryan, Z. J.; McNeil, A. J. Evidence for a Preferential Intramolecular Oxidative Addition in Ni-Catalyzed Cross-Coupling Reactions and Their Impact on Chain-Growth Polymerizations. *Chem. Sci.* **2013**, *4*, 1620–1624.

(6) Lanni, E. L.; Locke, J. R.; Gleave, C. M.; McNeil, A. J. Ligand-Based Steric Effects in Ni-Catalyzed Chain-Growth Polymerizations Using Bis(Dialkylphosphino)Ethanes. *Macromolecules* **2011**, *44* (13), 5136–5145.

(7) Smith, M. L.; Leone, A. K.; Zimmerman, P. M.; McNeil, A. J. Impact of Preferential π-Binding in Catalyst-Transfer Polycondensation of Thiazole Derivatives. *ACS Macro Lett.* **2016**, *5* (12), 1411–1415.

(8) Lanni, E. L.; McNeil, A. J. Mechanistic Studies on Ni(dppe)Cl_2 -Catalyzed Chain-Growth Polymerizations: Evidence for Rate-Determining Reductive Elimination. *J. Am. Chem. Soc.* **2009**, *131* (45), 16573–16579.

(9) Bryan, Z. J.; Hall, A. O.; Zhao, C. T.; Chen, J.; McNeil, A. J. Limitations of Using Small Molecules to Identify Catalyst-Transfer Polycondensation Reactions. *ACS Macro Lett.* **2016**, *5* (1), 69–72.

(10) Lee, S. R.; Bloom, J. W. G.; Wheeler, S. E.; McNeil, A. J. Accelerating Ni(II) Precatalyst Initiation Using Reactive Ligands and Its Impact on Chain-Growth Polymerizations. *Dalt. Trans.* **2013**, *42* (12), 4218.

(11) Hall, A. O.; Lee, S. R.; Bootsma, A. N.; Bloom, J. W. G.; Wheeler, S. E.; McNeil, A. J. Reactive Ligand Influence on Initiation in Phenylene Catalyst-Transfer Polymerization. *J. Polym. Sci. Part A Polym. Chem.* **2017**, *55* (9), 1530–1535.

(12) Lee, S. R.; Bryan, Z. J.; Wagner, A. M.; McNeil, A. J. Effect of Ligand Electronic Properties on Precatalyst Initiation and Propagation in Ni-Catalyzed Cross-Coupling Polymerizations. *Chem. Sci.* **2012**, *3* (5), 1562.

(13) Bryan, Z. J.; Smith, M. L.; McNeil, A. J. Chain-Growth Polymerization of Aryl Grignards Initiated by a Stabilized NHC-Pd Precatalyst. *Macromol. Rapid Commun.* **2012**, *33* (9), 842–847.

(14) Leone, A. K.; McNeil, A. J. Matchmaking in Catalyst-Transfer Polycondensation: Optimizing Catalysts Based on Mechanistic Insight. *Acc. Chem. Res.* **2016**, *49* (12), 2822–2831.

(15) Geng, Y.; Huang, L.; Wu, S.; Wang, F. Kumada Chain-Growth Polycondensation as a Universal Method for Synthesis of Well-Defined Conjugated Polymers. *Sci. China Chem.* **2010**, *53* (8), 1620–1633.

(16) Sheina, E. E.; Liu, J.; Lovu, M. C.; Laird, D. W.; McCullough, R. D. Chain Growth Mechanism for Regioregular Nickel-Initiated Cross-Coupling Polymerizations. *Macromolecules* **2004**, *37* (10), 3526–3528.

(17) Yokoyama, A.; Miyakoshi, R.; Yokozawa, T. Chain-Growth Polymerization for Poly(3-Hexylthiophene) with a Defined Molecular Weight and a Low Polydispersity. *Macromolecules* **2004**, *37* (4), 1169–1171.

(18) Loewe, R. S.; Ewbank, P. C.; Liu, J.; Zhai, L.; McCullough, R. D. Regioregular, Head-to-Tail Coupled Poly(3-Alkylthiophenes) Made Easy by the GRIM Method: Investigation of the Reaction and the Origin of Regioselectivity. *Macromolecules* **2001**, *34* (13), 4324–4333.

(19) Loewe, R. S.; Khersonsky, S. M.; McCullough, R. D. A Simple Method to Prepare Head-to-Tail Coupled, Regioregular Poly(3-Alkylthiophenes) Using Grignard Metathesis. *Adv. Mater.* **1999**, *11* (3), 250–253.

(20) Iovu, M. C.; Sheina, E. E.; Gil, R. R.; McCullough, R. D. Experimental Evidence for the Quasi-"Living" Nature of the Grignard Metathesis Method for the Synthesis of Regioregular Poly(3-Alkylthiophenes). *Macromolecules* **2005**, *38* (21), 8649–8656.

(21) Yokozawa, T.; Ohta, Y. Transformation of Step-Growth Polymerization into Living Chain-Growth Polymerization. *Chem. Rev.* **2016**, *116* (4), 1950–1958.

(22) Zhang, Y.; Tajima, K.; Hirota, K.; Hashimoto, K. Synthesis of All-Conjugated Diblock Copolymers by Quasi-Living Polymerization and Observation of Their Microphase Separation. *J. Am. Chem. Soc.* **2008**, *130* (25), 7812–7813.

(23) Zhang, Y.; Tajima, K.; Hashimoto, K. Nanostructure Formation in Poly(3-Hexylthiophene- Block -3-(2-Ethylhexyl)Thiophene)S. *Macromolecules* **2009**, *42* (18),

7008–7015.

(24) Van den Bergh, K.; Cosemans, I.; Verbiest, T.; Koeckelberghs, G. Expression of Supramolecular Chirality in Block Copoly(Thiophene)S. *Macromolecules* **2010**, *43* (8), 3794–3800.

(25) Song, I. Y.; Kim, J.; Im, M. J.; Moon, B. J.; Park, T. Synthesis and Self-Assembly of Thiophene-Based All-Conjugated Amphiphilic Diblock Copolymers with a Narrow Molecular Weight Distribution. *Macromolecules* **2012**, *45* (12), 5058–5068.

(26) Palermo, E. F.; McNeil, A. J. Impact of Copolymer Sequence on Solid-State Properties for Random, Gradient and Block Copolymers Containing Thiophene and Selenophene. *Macromolecules* **2012**, *45* (15), 5948–5955.

(27) Locke, J. R.; McNeil, A. J. Syntheses of Gradient π-Conjugated Copolymers of Thiophene. *Macromolecules* **2010**, *43* (21), 8709–8710.

(28) Tkachov, R.; Senkovskyy, V.; Komber, H.; Kiriy, A. Influence of Alkyl Substitution Pattern on Reactivity of Thiophene-Based Monomers in Kumada Catalyst-Transfer Polycondensation. *Macromolecules* **2011**, *44* (7), 2006–2015.

(29) Magurudeniya, H. D.; Sista, P.; Westbrook, J. K.; Ourso, T. E.; Nguyen, K.; Maher, M. C.; Alemseghed, M. G.; Biewer, M. C.; Stefan, M. C. Nickel(II) α-Diimine Catalyst for Grignard Metathesis (GRIM) Polymerization. *Macromol. Rapid Commun.* **2011**, *32* (21), 1748–1752.

(30) Bhatt, M. P.; Magurudeniya, H. D.; Sista, P.; Sheina, E. E.; Jeffries-EL, M.; Janesko, B. G.; McCullough, R. D.; Stefan, M. C. Role of the Transition Metal in Grignard Metathesis Polymerization (GRIM) of 3-Hexylthiophene. *J. Mater. Chem. A* **2013**, *1* (41), 12841.

(31) Sontag, S. K.; Bilbrey, J. A.; Huddleston, N. E.; Sheppard, G. R.; Allen, W. D.; Locklin, J. π-Complexation in Nickel-Catalyzed Cross-Coupling Reactions. *J. Org. Chem.* **2014**, *79* (4), 1836–1841.

(32) Bahri-Laleh, N.; Poater, A.; Cavallo, L.; Mirmohammadi, S. A. Exploring the Mechanism of Grignard Metathesis Polymerization of 3-Alkylthiophenes. *Dalt. Trans.* **2014**, *43* (40), 15143–15150.

(33) Zhao, Y.; Nett, A. J.; McNeil, A. J.; Zimmerman, P. M. Computational Mechanism for Initiation and Growth of Poly(3-Hexylthiophene) Using Palladium N-Heterocyclic Carbene Precatalysts. *Macromolecules* **2016**, *49* (20), 7632–7641.

(34) Nakamura, E.; Hatakeyama, T.; Ito, S.; Ishizuka, K.; Ilies, L.; Nakamura, M. *Chapter 1 Iron-Catalyzed Cross-Coupling Reactions*; 2014; Vol. 83.

(35) Kneebone, J. L.; Brennessel, W. W.; Neidig, M. L. Intermediates and Reactivity in Iron-

Catalyzed Cross-Couplings of Alkynyl Grignards with Alkyl Halides. *J. Am. Chem. Soc.* **2017**, *139* (20), 6988–7003.

(36) Clémancey, M.; Cantat, T.; Blondin, G.; Latour, J.-M.; Dorlet, P.; Lefèvre, G. Structural Insights into the Nature of Fe^0 and Fe^I Low-Valent Species Obtained upon the Reduction of Iron Salts by Aryl Grignard Reagents. *Inorg. Chem.* **2017**, *56* (7), 3834–3848.

(37) Kleimark, J.; Hedstrom, A.; Larsson, P.-F.; Johansson, C.; Norrby, P.-O. Mechanistic Investigation of Iron-Catalyzed Coupling Reactions. *ChemCatChem* **2009**, *1* (1), 152–161.

(38) Bauer, G.; Wodrich, M. D.; Scopelliti, R.; Hu, X. Iron Pincer Complexes as Catalysts and Intermediates in Alkyl-Aryl Kumada Coupling Reactions. *Organometallics* **2015**, *34* (1), 289–298.

(39) Hu, X. Nickel-Catalyzed Cross Coupling of Non-Activated Alkyl Halides: A Mechanistic Perspective. *Chem. Sci.* **2011**, *2* (10), 1867.

(40) Pollit, A. A.; Bridges, C. R.; Seferos, D. S. Evidence for the Chain-Growth Synthesis of Statistical π -Conjugated Donor-Acceptor Copolymers. *Macromol. Rapid Commun.* **2015**, *36* (1), 65–70.

(41) Bridges, C. R.; Yan, H.; Pollit, A. A.; Seferos, D. S. Controlled Synthesis of Fully π-Conjugated Donor-Acceptor Block Copolymers Using a Ni(II) Diimine Catalyst. *ACS Macro Lett.* **2014**, *3* (7), 671–674.

(42) Bridges, C. R.; McCormick, T. M.; Gibson, G. L.; Hollinger, J.; Seferos, D. S. Designing and Refining Ni(II)Diimine Catalysts toward the Controlled Synthesis of Electron-Deficient Conjugated Polymers. *J. Am. Chem. Soc.* **2013**, *135* (35), 13212–13219.

(43) Leone, A. K.; Souther, K. D.; Vitek, A. K.; LaPointe, A. M.; Coates, G. W.; Zimmerman, P. M.; McNeil, A. J. Mechanistic Insight into Thiophene Catalyst-Transfer Polymerization Mediated by Nickel Diimine Catalysts. *Macromolecules* **2017**, *50* (23), 9121–9127.

(44) Cherian, A. E.; Rose, J. M.; Lobkovsky, E. B.; Coates, G. W. A C_2-Symmetric, Living α-Diimine Ni(II) Catalyst: Regioblock Copolymers from Propylene. *J. Am. Chem. Soc.* **2005**, *127* (40), 13770–13771.

(45) Rose, J. M.; Deplace, F.; Lynd, N. A.; Wang, Z.; Hotta, A.; Lobkovsky, E. B.; Kramer, E. J.; Coates, G. W. C_2-Symmetric Ni(II) α -Diimines Featuring Cumyl-Derived Ligands: Synthesis of Improved Elastomeric Regioblock Polypropylenes. *Macromolecules* **2008**, *41* (24), 9548–9555.

(46) Rose, J. M.; Cherian, A. E.; Coates, G. W. Living Polymerization of α-Olefins with an α-Diimine Ni(II) Catalyst: Formation of Well-Defined Ethylene-Propylene Copolymers through Controlled Chain-Walking. *J. Am. Chem. Soc.* **2006**, *128* (13), 4186–4187.

(47) Vaidya, T.; Klimovica, K.; Lapointe, A. M.; Keresztes, I.; Lobkovsky, E. B.; Daugulis, O.; Coates, G. W. Secondary Alkene Insertion and Precision Chain-Walking: A New Route to Semicrystalline "Polyethylene" from α-Olefins by Combining Two Rare Catalytic Events. *J. Am. Chem. Soc.* **2014**, *136* (20), 7213–7216.

(48) O'Connor, K. S.; Watts, A.; Vaidya, T.; LaPointe, A. M.; Hillmyer, M. A.; Coates, G. W. Controlled Chain Walking for the Synthesis of Thermoplastic Polyolefin Elastomers: Synthesis, Structure, and Properties. *Macromolecules* **2016**, *49* (18), 6743–6751.

(49) Liu, F.-S.; Hu, H.-B.; Xu, Y.; Guo, L.-H.; Zai, S.-B.; Song, K.-M.; Gao, H.-Y.; Zhang, L.; Zhu, F.-M.; Wu, Q. Thermostable α-Diimine Nickel(II) Catalyst for Ethylene Polymerization: Effects of the Substituted Backbone Structure on Catalytic Properties and Branching Structure of Polyethylene. *Macromolecules* **2009**, *42* (20), 7789–7796.

(50) Liu, J.; Chen, D.; Wu, H.; Xiao, Z.; Gao, H.; Zhu, F.; Wu, Q. Polymerization of α-Olefins Using a Camphyl α-Diimine Nickel Catalyst at Elevated Temperature. *Macromolecules* **2014**, *47* (10), 3325–3331.

(51) Zhong, L.; Li, G.; Liang, G.; Gao, H.; Wu, Q. Enhancing Thermal Stability and Living Fashion in α-Diimine–Nickel-Catalyzed (Co)Polymerization of Ethylene and Polar Monomer by Increasing the Steric Bulk of Ligand Backbone. *Macromolecules* **2017**, *50* (7), 2675–2682.

(52) Souther, K. D.; Leone, A. K.; Vitek, A. K.; Palermo, E. F.; LaPointe, A. M.; Coates, G. W.; Zimmerman, P. M.; McNeil, A. J. Trials and Tribulations of Designing Multitasking Catalysts for Olefin/Thiophene Block Copolymerizations. *J. Polym. Sci. Part A Polym. Chem.* **2017**, 1–6.

(53) Li, M. W.; Pendleton, I. M.; Nett, A. J.; Zimmerman, P. M. Mechanism for Forming B,C,N,O Rings from NH_3 BH_3 and CO_2 via Reaction Discovery Computations. *J. Phys. Chem. A* **2016**, *120* (8), 1135–1144.

(54) Khomutnyk, Y. Y.; Argüelles, A. J.; Winschel, G. A.; Sun, Z.; Zimmerman, P. M.; Nagorny, P. Studies of the Mechanism and Origins of Enantioselectivity for the Chiral Phosphoric Acid-Catalyzed Stereoselective Spiroketalization Reactions. *J. Am. Chem. Soc.* **2016**, *138* (1), 444–456.

(55) Ellington, B. R.; Paul, B.; Das, D.; Vitek, A. K.; Zimmerman, P. M.; Marsh, E. N. G. An Unusual Iron-Dependent Oxidative Deformylation Reaction Providing Insight into Hydrocarbon Biosynthesis in Nature. *ACS Catal.* **2016**, *6* (5), 3293–3300.

(56) Pendleton, I. M.; Pérez-Temprano, M. H.; Sanford, M. S.; Zimmerman, P. M. Experimental and Computational Assessment of Reactivity and Mechanism in C(Sp 3)–N Bond-Forming Reductive Elimination from Palladium(IV). *J. Am. Chem. Soc.* **2016**, *138* (18), 6049–6060.

(57) Ludwig, J. R.; Zimmerman, P. M.; Gianino, J. B.; Schindler, C. S. Iron(III)-Catalysed Carbonyl–olefin Metathesis. *Nature* **2016**, *533* (7603), 374–379.

(58) Sun, Z.; Winschel, G. a.; Zimmerman, P. M.; Nagorny, P. Enantioselective Synthesis of Piperidines through the Formation of Chiral Mixed Phosphoric Acid Acetals: Experimental and Theoretical Studies. *Angew. Chemie Int. Ed.* **2014**, *53* (42), 11194–11198.

(59) Nett, A. J.; Zhao, W.; Zimmerman, P. M.; Montgomery, J. Highly Active Nickel Catalysts for C?H Functionalization Identified through Analysis of Off-Cycle Intermediates. *J. Am. Chem. Soc.* **2015**, *137* (24), 7636–7639.

(60) Nett, A. J.; Montgomery, J.; Zimmerman, P. M. Entrances, Traps, and Rate-Controlling Factors for Nickel-Catalyzed C–H Functionalization. *ACS Catal.* **2017**, *7* (10), 7352–7362.

(61) Zimmerman, P. M. Single-Ended Transition State Finding with the Growing String Method. *J. Comput. Chem.* **2015**, *36* (9), 601–611.

(62) Zimmerman, P. M. Growing String Method with Interpolation and Optimization in Internal Coordinates: Method and Examples. *J. Chem. Phys.* **2013**, *138* (18), 184102.

(63) Zimmerman, P. Reliable Transition State Searches Integrated with the Growing String Method. *J. Chem. Theory Comput.* **2013**, *9* (7), 3043–3050.

(64) Zimmerman, P. M. Navigating Molecular Space for Reaction Mechanisms: An Efficient, Automated Procedure. *Mol. Simul.* **2015**, *41* (1–3), 43–54.

(65) Zimmerman, P. M. Automated Discovery of Chemically Reasonable Elementary Reaction Steps. *J. Comput. Chem.* **2013**, *34* (16), 1385–1392.

(66) In this study, high-spin square planar complexes relaxed to a tetrahedral geometry and low-spin tetrahedral geometries relaxed to a square planar geometry during optimization.

(67) The weak crystal-field splitting results in three nearly degenerate orbitals (t_{2g}), and causes a stable tetrahedral geometry.

(68) Thomson, J.; Baird, M. C. Trends in the Spectrochemical Series and 31 P Chemical Shifts of Five-Coordinated Cyclopentadienylnickel(II) Complexes. *Can. J. Chem.* **1973**, *51* (8), 1179–1182.

(69) Evans, D. F. 400. The Determination of the Paramagnetic Susceptibility of Substances in Solution by Nuclear Magnetic Resonance. *J. Chem. Soc.* **1959**, 2003.

(70) Sur, S. K. Measurement of Magnetic Susceptibility and Magnetic Moment of Paramagnetic Molecules in Solution by High-Field Fourier Transform NMR

Spectroscopy. *J. Magn. Reson.* **1989**, *82* (1), 169–173.

(71) Attempts to synthesize the L^2NiBr_2 precatalyst were not successful.

(72) Note that THF-d_8 displaces L^1 causing an equilibrium between bound and unbound ligand, hence small but visible L^1 peaks.

(73) Guggenberger, L. J.; Rundle, R. E. Crystal Structure of the Ethyl Grignard Reagent, Ethylmagnesium Bromide Dietherate. *J. Am. Chem. Soc.* **1968**, *90* (20), 5375–5378.

(74) Spek, A. L.; Voorbergen, P.; Schat, G.; Blomberg, C.; Bickelhaupt, F. The Structure of the Grignard Reagent. *J. Organomet. Chem.* **1974**, *77* (2), 147–151.

(75) Engelhardt, L. M.; Harvey, S.; Raston, C. L.; White, A. H. Organo-Magnesium Reagents: The Crystal Structures of [Mg(Anthracene)(THF)3] and [Mg(Triphenylmethyl)Br(OEt2)2]. *J. Organomet. Chem.* **1988**, *341* (1–3), 39–51.

(76) Tammiku-Taul, J.; Burk, P.; Tuulmets, A. Theoretical Study of Magnesium Compounds: The Schlenk Equilibrium in the Gas Phase and in the Presence of Et 2 O and THF Molecules. *J. Phys. Chem. A* **2004**, *108* (1), 133–139.

(77) Mori, T.; Kato, S. Grignard Reagents in Solution: Theoretical Study of the Equilibria and the Reaction with a Carbonyl Compound in Diethyl Ether Solvent. *J. Phys. Chem. A* **2009**, *113* (21), 6158–6165.

(78) Mehmood, U.; Al-Ahmed, A.; Hussein, I. A. Review on Recent Advances in Polythiophene Based Photovoltaic Devices. *Renew. Sustain. Energy Rev.* **2016**, *57*, 550–561.

(79) Ewbank, P. C.; Stefan, M. C.; Sauv, G.; McCullough, R. D. Synthesis, Characterization and Properties of Regioregular Polythiophene-Based Materials. In *Handbook of Thiophene-Based Materials*; John Wiley & Sons, Ltd: Chichester, UK, 2009; pp 157–217.

(80) Becke, A. D. Density-Functional Thermochemistry. III. The Role of Exact Exchange. *J. Chem. Phys.* **1993**, *98* (7), 5648.

(81) Lee, C.; Yang, W.; Parr, R. G. Development of the Colle-Salvetti Correlation-Energy Formula into a Functional of the Electron Density. *Phys. Rev. B* **1988**, *37* (2), 785–789.

(82) Vosko, S. H.; Wilk, L.; Nusair, M. Accurate Spin-Dependent Electron Liquid Correlation Energies for Local Spin Density Calculations: A Critical Analysis. *Can. J. Phys.* **1980**, *58* (8), 1200–1211.

(83) Stephens, P. J.; Devlin, F. J.; Chabalowski, C. F.; Frisch, M. J. Ab Initio Calculation of Vibrational Absorption and Circular Dichroism Spectra Using Density Functional Force Fields. *J. Phys. Chem.* **1994**, *98* (45), 11623–11627.

(84) Hay, P. J.; Wadt, W. R. Ab Initio Effective Core Potentials for Molecular Calculations. Potentials for K to Au Including the Outermost Core Orbitals. *J. Chem. Phys.* **1985**, *82* (1), 299–310.

(85) Hay, P. J.; Wadt, W. R. Ab Initio Effective Core Potentials for Molecular Calculations. Potentials for the Transition Metal Atoms Sc to Hg. *J. Chem. Phys.* **1985**, *82* (1), 270.

(86) Wadt, W. R.; Hay, P. J. Ab Initio Effective Core Potentials for Molecular Calculations. Potentials for Main Group Elements Na to Bi. *J. Chem. Phys.* **1985**, *82* (1), 284–298.

(87) Chai, J.-D.; Head-Gordon, M. Systematic Optimization of Long-Range Corrected Hybrid Density Functionals. *J. Chem. Phys.* **2008**, *128* (8), 084106.

(88) Dunning, T. H. Gaussian Basis Sets for Use in Correlated Molecular Calculations. I. The Atoms Boron through Neon and Hydrogen. *J. Chem. Phys.* **1989**, *90* (2), 1007–1023.

(89) Woon, D. E.; Dunning, T. H. Gaussian Basis Sets for Use in Correlated Molecular Calculations. V. Core-valence Basis Sets for Boron through Neon. *J. Chem. Phys.* **1995**, *103* (11), 4572–4585.

(90) Balabanov, N. B.; Peterson, K. A. Systematically Convergent Basis Sets for Transition Metals. I. All-Electron Correlation Consistent Basis Sets for the 3d Elements Sc-Zn. *J. Chem. Phys.* **2005**, *123* (6).

(91) Wilson, A. K.; Woon, D. E.; Peterson, K. A.; Dunning, T. H. Gaussian Basis Sets for Use in Correlated Molecular Calculations. IX. The Atoms Gallium through Krypton. *J. Chem. Phys.* **1999**, *110* (16), 7667–7676.

(92) Cammi, R.; Tomasi, J. Remarks on the Use of the Apparent Surface Charges (ASC) Methods in Solvation Problems: Iterative versus Matrix-Inversion Procedures and the Renormalization of the Apparent Charges. *J. Comput. Chem.* **1995**, *16* (12), 1449–1458.

(93) Tomasi, J.; Mennucci, B.; Cammi, R. Quantum Mechanical Continuum Solvation Models. *Chem. Rev.* **2005**, *105* (8), 2999–3093.

(94) Aleksandr V. Marenich, Christopher J. Cramer, and D. G. T. Universal Solvation Model Based on Solute Electron Density and on a Continuum Model of the Solvent Defined by the Bulk Dielectric Constant and Atomic Surface Tensions. *J. Phys. Chem. B* **2009**, *113* (18), 6378–6396.

Chapter 4: Revealing the Strong Relationships between Ligand Conformers and Activation Barriers: A Case Study of Bisphosphine Reductive Elimination

4.1 Abstract

Quantum chemical models of reaction pathways can provide deep insight into the inner workings of transition metal complexes. Largely, these simulations have relied on atomistic models where a single or a few conformational isomers of the complex are investigated. This article will show that for bisphosphine Ni complexes used to forge C-C bonds, a large number of conformers must be studied to provide confidence that the overall model is meaningful. Conformer effects do not only modify particular reaction barriers, but often the lowest barrier reaction pathway proceeds from a conformer that is not the lowest energy conformer. This finding suggests that errors on the order of a more than a few kcal/mol are likely present in single-conformer studies. The particular reaction pathway and conformer preferences for a series of eight common Ni bisphosphine complexes will provide some guidance as to when the effects of conformer will be large or small.

4.2 Introduction

Atomistic simulations of transition metal complexes have provided amazing insight into the underlying mechanisms of catalysis. The major goals of these simulations include providing deeper insight into the sequences and character of elementary steps as well as giving quantitative analysis of the energy landscape such as activation barriers. This research is most often done using quantum chemistry, allowing predictions to be made in an *ab initio* fashion that gives some degree of independence from prior experimental results. Altogether, computational models have attempted to shed light on the structure-activity relationships that govern reactivity and selectivity, with the hope of tuning catalysts for optimal performance.[1–3] Despite continued interest in using computational techniques for catalyst design, it is not currently obvious that one

can simply “compute the right transition metal catalyst” for a specific transformation in a predictive and accurate fashion. There is nothing in principle that should forbid the *ab initio* design process from succeeding, however, but significant challenges clearly remain.[4–7]

The intent of this article is to identify and promote one key, somewhat neglected, factor that strongly influences catalyst activity: ligand conformation. The majority of quantum chemical studies of transition metal catalysts presume a single, or a few, conformers of the ancillary and reactive ligands are relevant. While in some cases high symmetry of the ligands may make this choice reasonable,[8] in many others the catalyst conformation will have a large effect on the resulting properties from simulation.[9–11] Organometallic catalysts with flexible ligands are expected to adopt a number of unique conformations, and reactions at these catalysts will be sensitive to catalyst-substrate binding modes, rotations in the ancillary ligand side chains, geometry of the transition metal, as well as regioselectivity and stereoselectivity of the transformation.[12,13] Conformationally induced ground and transition state effects for less chemically selective reactions, however, are rarely investigated thoroughly. These conformational effects impart a high degree of uncertainty in calculated reaction paths when predicting the global minimum or the lowest energy transition state for a given chemical structure.[13,14] While comparison to experimental structures can be made for relatively stable species (especially precatalysts), geometric information for short-lived intermediates and transition states is much more scarce. Furthermore, even if a non-exhaustive conformational search identifies the most stable conformer for a given elementary step, the lowest energy transition state may begin from a different, higher energy initial conformation. The degree of sensitivity in the energetics of reactive intermediates and transition states to conformational variation therefore is ambiguous, unless thorough sampling has been performed.

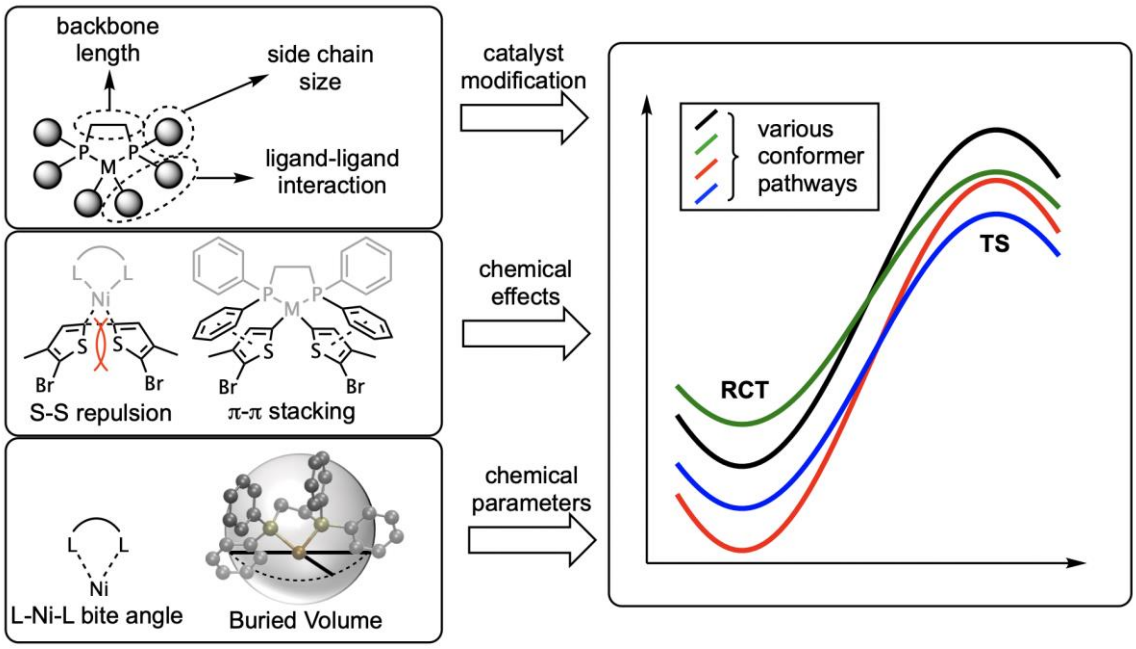

Figure 4.1: Chemical effects that lead to conformers with varied catalyst geometries and conformer effects on the energy landscape.

Transition metal catalysts have enabled a variety of cross-coupling reactions and are an indispensable tool for C-C and C-heteroatom bond formation. For select cross-coupling reactions, bidentate phosphine ligands in particular are known to impart a highly useful degrees of stereo- and regio-control.[15–19] For example, bisphosphine nickel complexes are established, high-performing catalysts for synthesizing conjugated polymers by enchaining thiophene and other aromatic monomers.[20] This reaction depends sensitively on a number of required steps, including transmetalation, reductive elimination, and chain-walking, that must proceed in a controlled manner to obtain polymers with desirable materials properties. The reductive elimination step is often found to be rate limiting for conjugated polymer synthesis using nickel bisphosphine catalysts,[21,22] and it also represents an vital step for a wide variety of other important cross-coupling reactions. To our knowledge, no study to date has reported a computational analysis of the effects of reactive and ancillary ligand conformation on the reductive elimination process, or a comparison of different ancillary ligands and their resulting effect on conformational degrees of freedom.

Herein, the conformational effects on the C-C bond forming elementary step at Ni bisphosphine catalysts with varying phosphine side chains (R=methyl, phenyl, cyclohexyl, and

tert-butyl) and alkyl backbones (ethyl and propyl) are described (Figure 4.2). This study will show that ancillary and reactive ligand flexibility give rise to a significant number of stable conformers, and therefore a distribution of properties even within each type of ancillary ligand. Importantly, there is not a one-to-one relationship between the most stable reactant complex and the lowest energy transition state. This is shown qualitatively in Figure 4.1, which provides an example where the lowest energy reactant and transition state come from two unique conformers (red and blue pathways, respectively). Computing only a single or limited number of reactant conformers could lead to inaccurate reaction barriers and decrease the reliability of first principles predictions. In sum, this study will detail the causes and magnitudes of ligand conformer effects on reductive elimination, and show that conformers have diverse, interesting properties that have real impact on catalysis.

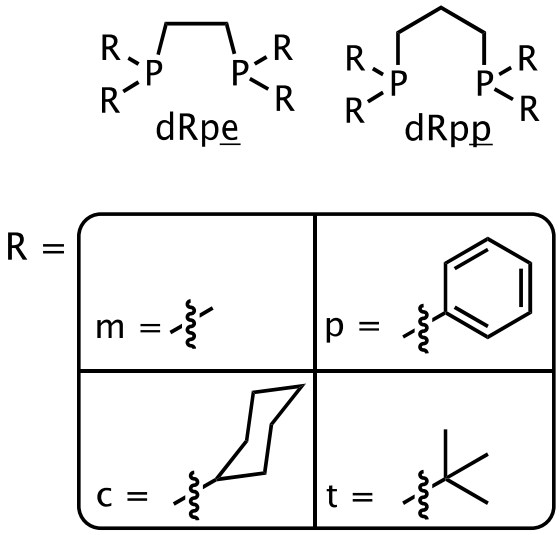

Figure 4.2: Bisphosphine ligands surveyed for reductive elimination in this study. Naming conventions for the backbone length and the phosphine side chains are included for clarity.

4.3 Results and Discussion

This study evaluates the energetics and geometries of Ni bisphosphine transition metal complexes with a pair of thiophene reactive ligands. The reaction pathways studied in this work therefore are a single-step C-C bond formations that reduce Ni(II) to Ni(0) and result in the dithiophene complex bound to the metal center through a metal-thiophene π-complex.[23,24] The intermediate that immediately precedes reductive elimination adopts different conformations that

depend on the flexibility of the bisphosphine ancillary ligand and the thiophene reactive ligands. The geometric degrees of freedom that allow for these conformers include the rotation of phosphine side chains, rotation of the thiophene reactive ligands, and distortion of the square planar intermediate via torsions of ancillary and reactive ligands (see section B.3 in Appendix B for the method to generate these conformers).

The number of unique conformers and the degree of energetic and geometric variations vary widely with properties of the ancillary ligand. For example, the methyl side chains of dmpe freely rotate but have little consequence on the stability of the metal complex, resulting in conformers that are nearly isoenergetic. The phenyl side chains of dppe, however, demonstrate a wide range of inner sphere steric interactions and π-π stacking interactions and therefore a larger spread of energies when the phenyl groups and backbone are twisted. Figure 4.3(a) and 4.3(b) show the conformers for the dppe and dmpe ancillary ligands to illustrate the effects of a flexible ligand compared to a more static ligand.

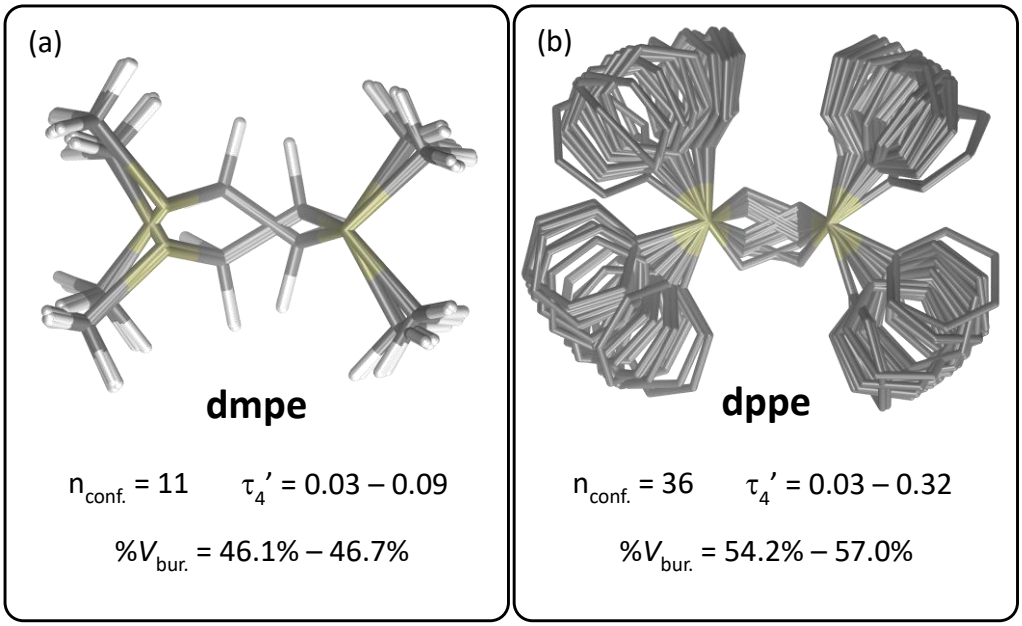

Figure 4.3: Conformer ensembles for dmpe and dppe complexes. The reactive ligands and nickel are removed to highlight the ancillary ligand flexibility. Planarity metrics (τ_4') and steric parameter (% buried volume ($\%V_{bur.}$)) ranges are provided of the two conformer ensembles.

In dppe, the phenyl groups permit a range (Figure 4.3(b)) of π-π stacking interactions with the each other and with the thiophene reactive ligands (not shown). This interaction and the

nontrivial steric encumbrance that is present with the phenyl side chains allow for the large number of stable conformers for dppe compared to dmpe. Two geometric parameters shown in Figure 4.3, square planarity (τ_4')[25,26] and buried volume (%$V_{bur.}$),[27] are useful chemical descriptors for quantifying structural differences of these conformers. τ_4' indicates the degree to which a complex exhibits a square planar (τ_4'=0) or tetrahedral (τ_4'=1) geometry. %$V_{bur.}$ quantifies steric encumbrance of an ancillary ligand by providing the percentage of the total volume of a sphere occupied or "buried" by that ligand. These metrics can be important to determining the kinetic viability of the reductive elimination step and designing catalysts to reduce this reaction barrier and have been used in prior studies.[28,29] In ideal cases, it is thought that a single descriptor or combination of descriptors might be used to predict reaction rates or other chemical quantities of interest for catalyst and reaction design. In comparing our first two ligands, dppe conformers exhibit ~5X more flexibility in the two geometric parameters compared to dmpe. These conformer-induced energetic effects of the geometrically varied dppe conformers manifests itself in nontrivial changes in the ground and transition state energetics (Figure 4.4).

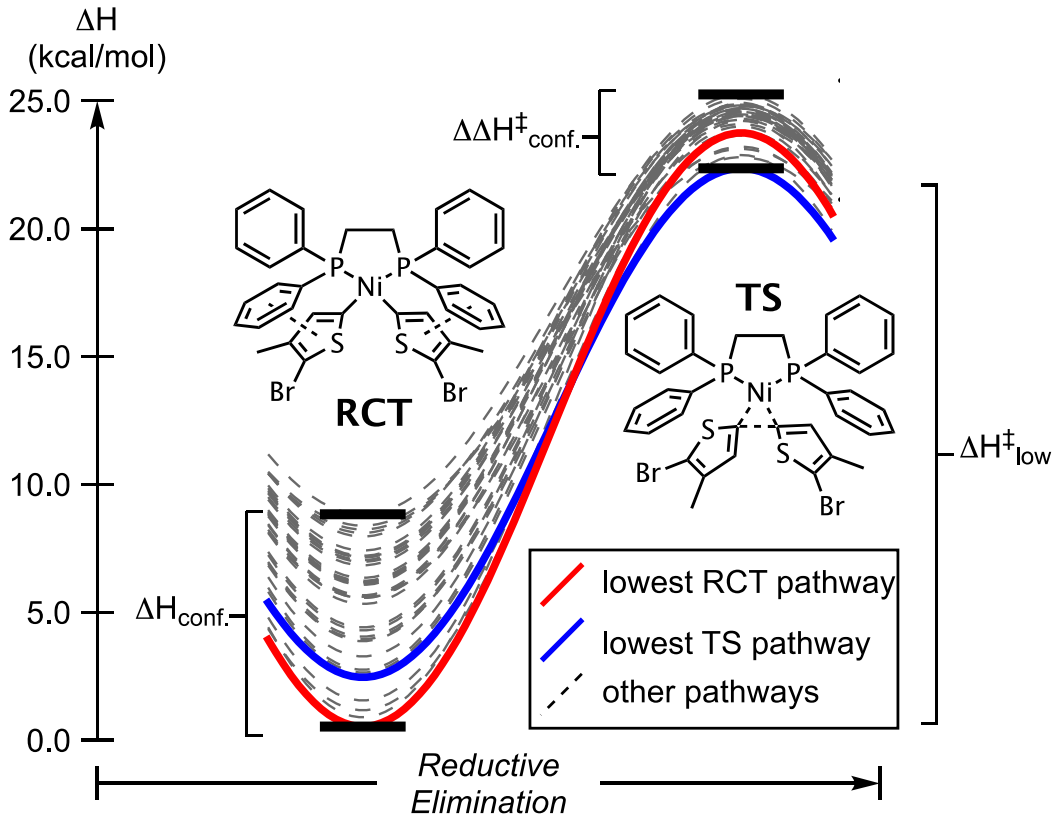

Figure 4.4: Enthalpic profiles for all reductive elimination pathways found for the Ni(dppe) catalyst conformers. Pathways for the most stable conformer (red) and transition state (blue) are highlighted. Enthalpies are referenced to the most stable conformer.

Dppe is a nicely illustrative example for conformational effects due to the flexibility of its phenyl side chains and the π-π stacking interactions that occur between the side chains and thiophene ligands. These characteristics result in a range of relative conformer energies ($\Delta H_{conf.}$) and transition state energies ($\Delta\Delta H^{\ddagger}_{conf.}$). In the 36 dppe intermediates that precede reductive elimination, the reactant conformers (RCT) demonstrate a substantial range of energies (9.5 kcal/mol). The transition state effect exhibited by the dppe conformers is roughly half the ground state effect (4.6 kcal/mol). Most reductive elimination transition state (TS) conformers are within the 23.0-24.6 kcal/mol range (31 of the 36 pathways found). Assuming all RCT species are in equilibrium, the lowest energy RCT species would isomerize to the fifth-lowest RCT species, and proceed to form a C-C bond with an enthalpic barrier of 21.2 kcal/mol (blue pathway in Figure 4.4). Statistically, it is unlikely that this particular conformer would be found by accident among the other 35 conformers. The range in $\Delta H_{conf.}$ and $\Delta\Delta H^{\ddagger}$ values illustrates a significant challenge of predicting activation barriers for conformationally flexible complexes. Even if one

identifies the most stable conformer, that conformer does not necessarily proceed to the most stable transition state. This conformer effect introduces a significant source of error in predicting the activation energy, and therefore we now turn to analyze how this effect generalizes to the other ancillary ligands.

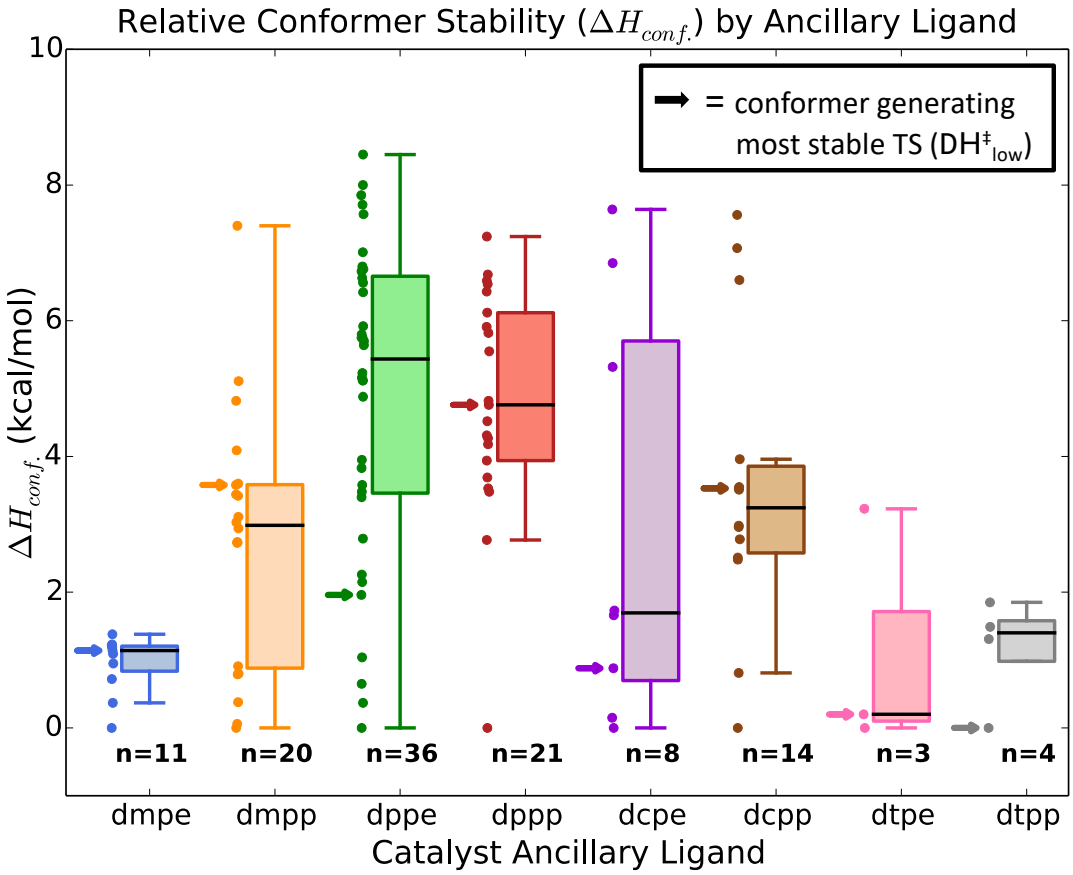

Figure 4.5: Boxplot representation of relative conformer enthalpy distribution sorted by catalyst ancillary ligand. $\Delta H_{conf.}$ is referenced from the most stable conformer for each catalyst.

Figure 4.5 depicts $\Delta H_{conf.}$ of the intermediate that precedes reductive elimination, for the metal complexes ligated by the 8 bisphosphines of Figure 4.2. The least encumbering ligand, dmpe, demonstrates that sterically compact phosphine sidechains can lead to conformers of similar energy. The methyl side chains with propyl backbone of dmpp, however, imparts more geometric variation in its conformers, and results in a larger range of RCT enthalpies ($\Delta H_{conf.}$ is 1.9 kcal/mol for dmpe and 6.5 kcal/mol for dmpp). The relatively larger phenyl and cyclohexyl side chains tend to give highly varied geometries of the conformers, correspondingly large

$\Delta H_{conf.}$ values (dppe: 8.5 kcal/mol, dppp: 7.2 kcal/mol, dcpe: 6.8 kcal/mol, dcpp: 7.6 kcal/mol). Tert-butyl side chains result in fewer conformers, and relatively narrow ranges of conformer energies ($\Delta H_{conf.}$ for dtpe and dtpp are 3.2 and 1.9 kcal/mol, respectively) due to their massive steric bulk and relative unimportance of rotational degrees of freedom. Interestingly, the most stable conformer for dppp is a special case that seems to be unique among the eight bisphosphines. In dppp, there exists a high-symmetry π-π stacking effect that is not seen in dppe or other conformers (see Figure 5.19 in Appendix B), resulting in a lowest energy structure that is separated by almost 3 kcal/mol from the next lowest energy conformer.

The inherent ancillary ligand flexibility corresponds well to the number of accessible conformers as well as the range of conformer energies, $\Delta H_{conf.}$. Increasing the alkyl backbone size generally increases the flexibility and number of conformers available for a given phosphine side chain, except for the most encumbering ancillary ligands. Unencumbering side chains may be flexible, but also have weak effects on the relative stability of each conformer. On the other hand, the flexibility of the phenyl and cyclohexyl side chains has larger a consequence on $\Delta H_{conf.}$ due to the many orientations these four side chains can adopt in each bisphosphine complex.

The arrows in Figure 4.5 show that the lowest enthalpy TSs are often produced from high enthalpy conformers. For only the 3 least flexible ligands (dcpe, dtpe, and dtpp), the lowest enthalpy transition state is found from a conformer within 1 kcal/mol of the most stable conformer. In the other cases, the conformers that reach the lowest energy TSs are 1.1 to 4.8 kcal/mol above the lowest energy RCT conformer. This affirms the earlier indication that a thorough conformer search may be needed to find the lowest enthalpy transition state for phosphine ligands with highly encumbering side chains. Of course, the lowest energy RCT conformer must be found as well to attain a meaningful reference energy for the barrier height.

Catalyst	Minimum-Maximum (Average) Values		
	Bite Angle (°)	**%$V_{bur.}$ (%)**	**τ_4'**
dmpe	87.7-88.2 (88.0)	46.1-46.7 (46.4)	0.03-0.09 (0.05)
dmpp	93.1-98.0 (95.4)	47.6-48.8 (48.2)	0.05-0.24 (0.13)
dppe	84.5-88.7 (86.0)	54.2-57.0 (55.8)	0.03-0.32 (0.19)
dppp	89.6-97.5 (91.8)	56.2-59.2 (57.4)	0.12-0.34 (0.25)
dcpe	86.9-88.8 (87.6)	58.9-61.1 (59.6)	0.06-0.30 (0.14)
dcpp	91.7-97.9 (94.9)	58.3-61.1 (59.9)	0.09-0.40 (0.29)
dtpe	91.0-91.2 (91.1)	61.9-62.1 (62.0)	0.27-0.30 (0.28)
dtpp	97.9-99.1 (98.7)	64.4-65.9 (65.1)	0.33-0.41 (0.37)

Table 4.1: Key geometric parameters (bisphosphine bite angle, %$V_{bur.}$, and τ_4') of the eight bisphosphine catalyst conformer ensembles.

The geometric variation in conformers amongst the 8 catalysts can be quantified using geometric parameters such as the bite angle of the bisphosphine,[30] %$V_{bur.}$, a measure of the "buried" volume that is inaccessible to the reactive ligands, and τ_4', which quantifies the distortion of the square planar geometries towards tetrahedral structures. Unsurprisingly, bisphosphine P-Ni-P bite angles increase when the alkyl backbone is lengthened from ethyl to propyl (increases by ~6-8°). Absolute bite angles, however, do not necessarily increase for more encumbering side chains. For example, ancillary ligands where R=phenyl have smaller bite angles than R=methyl (average bite angles are 86.0°/91.8° for dppe/dppp and 88.0°/95.4° for dmpe/dmpp). This is likely due to the thiophene-phenyl π-π stacking interactions restricting the bisphosphine bite angle when R=phenyl compared to methyl. %$V_{bur.}$ increases in a predictable fashion as the sidechain steric size increases (methyl<phenyl<cyclohexyl<tert-butyl) and as the alkyl backbone lengthens.

The τ_4' values reflect similar qualitative trends of steric size and ligand flexibility as the two other parameters. For instance, dmpe exhibits a narrow range of geometric distortion (τ_4' range of 0.03-0.09), indicating that the combination of unencumbering methyl side chains and inflexible ethyl backbone does not significantly destabilize reactant geometries. The dppe ligand is an interesting example with a large range of distortion (0.03-0.32), even though its ethyl

backbone is somewhat restricted in flexibility. This effect can be attributed to π-π stacking interactions that pull the ancillary and reactive ligands away from the ideal square planar geometry. Ligands where R=tert-butyl have fairly high τ_4' (>0.25 for dtpe and dtpp), showing the great degree of distortion from these highly encumbering ligands. Tert-butyl ligands therefore should give significantly lower reductive elimination barriers compared to complexes with less encumbering ancillary ligands. Having examined the reactant conformer effect and the geometric parameters that describe this effect, we now turn to the effect of conformers on the TS.

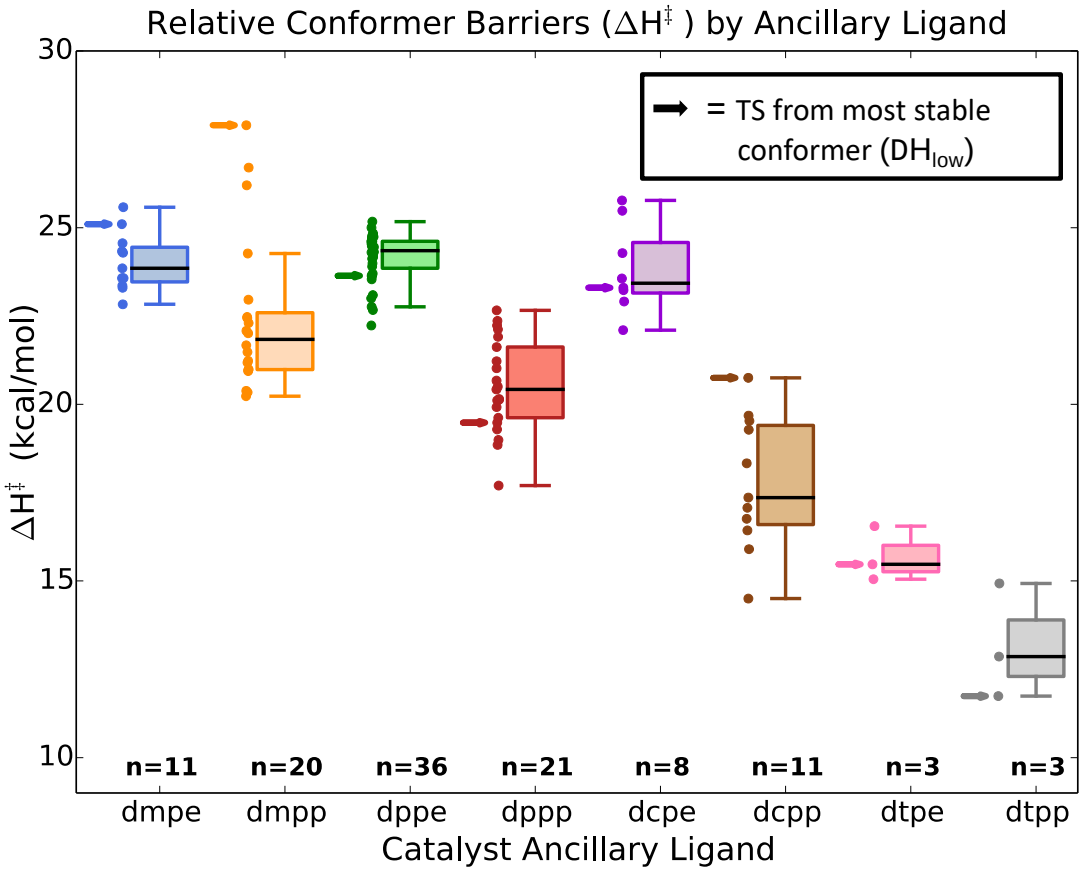

Figure 4.6: Boxplot representation of conformer reductive elimination transition state energies (ΔH‡) is sorted by catalyst ancillary ligand. ΔH‡ is referenced from the most stable conformer for each catalyst.

The activation barriers for reductive elimination across the 8 transition metal complexes are shown in Figure 4.6. The transition states produced from the lowest enthalpy conformers for each ancillary ligand (arrows in Figure 4.6) show that the lowest energy RCT state can lead to the highest barrier TS. This occurs for dmpp and dcpp, which would result in errors in the activation energy of over 5 kcal/mol. These effects are kinetically significant, as a change of 1.4

kcal/mol at room temperature corresponds to a factor of 10 difference in the rate. The trends in energy range differ somewhat from the range of RCT energies. For example, extending the bisphosphine backbone from ethyl to propyl increases the range of reductive elimination transition state energies. The lowest enthalpy transition states for each catalyst demonstrate that the propyl backbone leads to significantly lower barriers for reductive elimination. This is expected because the larger alkyl backbone results in a larger bisphosphine bite angle, a smaller C-Ni-C angle for the two thiophene reactive ligands, and a reactant that is closer to the transition state. In moderate cases (dmpe to dmpp and dppe to dppp), the reductive elimination barrier is reduced by ~2 kcal/mol when substituting a propyl phosphine backbone for the ethyl backbone. This effect increases for the cyclohexyl and *t*-butyl containing ancillary ligands where the propyl backbone ligands result in ~4 and ~6 kcal/mol reduction in the activation barrier. This relationship is reflected in the R^2=0.55 correlation between bite angle and the lowest calculated activation barrier for the 8 bisphosphine complexes (a stronger relationship will be shown further below).

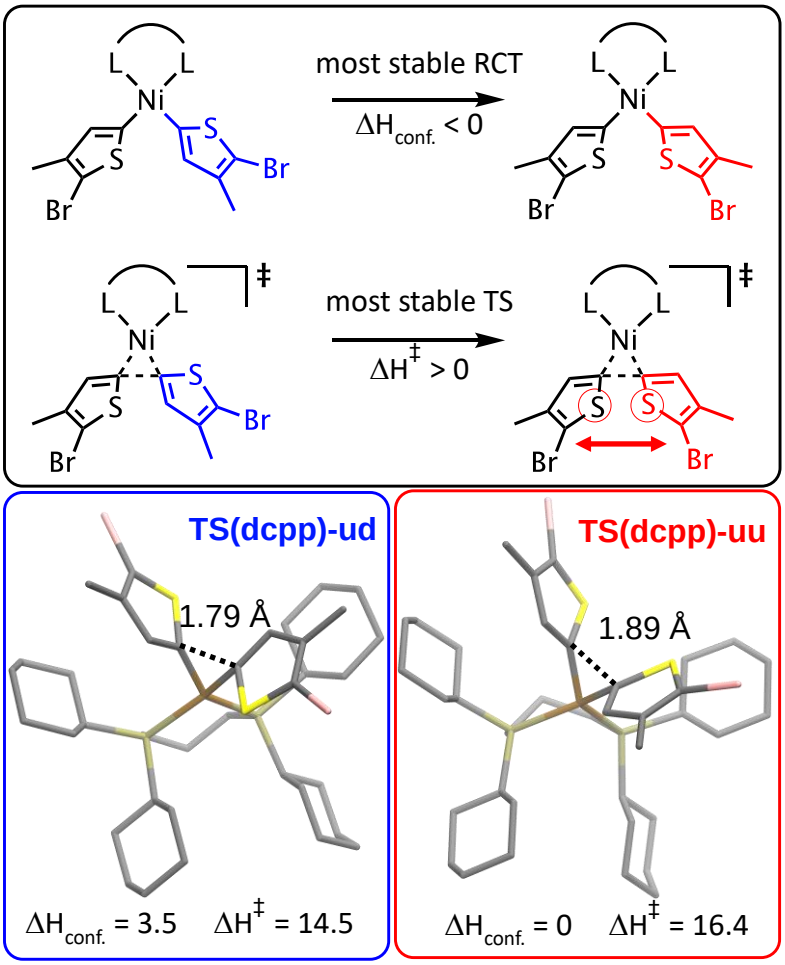

Figure 4.7: Geometry comparison of dcpp conformations with thiophene "up-down" and "up-up" orientations. $\Delta H_{conf.}$ and $\Delta H^{\ddagger}$ is referenced from the most stable conformer for each catalyst and in units kcal*mol^{-1}.

Close examination of the ensemble of conformer geometries across the 8 catalysts provided more insight into the underlying reasons for variation in RCT and TS energetics. For example, the thiophene-thiophene reactive ligand orientation appears to determine the lowest enthalpy transition state (Figure 4.7). While up until this point the ancillary ligand has been our focus, the thiophene reactive ligands are another major component to the flexibility of the metal complexes. The thiophene ligands can adopt conformations where each ligand has the same orientation, or opposite orientations ("up-down" or "up-up" orientation). The two dcpp transition states, TS(dcpp)-ud and TS(dcpp)-uu, demonstrate this relationship and are shown in Figure 4.7.

TS(dcpp)-ud adopts the "up-down" orientation and allows for the lowest calculated reductive elimination barrier (14.5 kcal/mol) despite originating from a nominally less stable RCT geometry (by 3.5 kcal/mol). The source of the low barrier for the "up-down" orientation is apparent when comparing TS(dcpp)-ud with the "up-up" orientation of TS(dcpp)-uu. In particular, the lone pair repulsions between the two sulfur atoms results in a destabilized transition state (16.4 kcal/mol) because the two sulfurs are brought close together during the C-C bond formation process. This repulsion results in a 0.10 Å increase in the $d_{C\text{-}C}$ bond distance at the TS when comparing the two orientations. All eight catalysts featured conformer ensembles where the lowest enthalpy reductive elimination transition state adopted the "up-down" thiophene ligand orientation. The thiophene orientation of the lowest enthalpy RCT conformer, however, are ancillary ligand-dependent, with seven of the eight catalysts preferring the "up-up" and only the dtpp ligand preferring the "up-down" orientation. The unique preference of dtpp is likely due the S-S repulsive effect at the RCT rather than the TS, where the tert-butyl side chains and the large bite angle of the propyl backbone (Table 4.1) push the thiophene ligands into close proximity.

So far, the thorough conformer search has provided heuristics for relating ligand flexibility to the energy landscape for reductive elimination. At first, the large number of conformers and variety of effects may make it seem unlikely that any single metric could be used to quantify the lowest activation barrier for each bisphosphine catalyst. Such a predictive metric for reductive elimination barriers, however, would be a valuable tool for catalyst design, so such a metric was sought out.

The first predictive geometry metric analyzed was the metal-ligand bite angle[31,32] of the bisphosphine due to the established effects between the bite angle of catalysts ligated with

bidentate phosphines and chemical rates, selectivities, and other quantities of interest for various reactions (e.g., hydroformylation,[33–37] hydrocyanation,[38,39] allylic alkylation,[40] and cross-coupling reactions[41,42]). The bisphosphine bite angle is a useful metric for explaining how varying the alkyl backbone length and side chain of bisphosphine ancillary ligand relates to its steric encumbrance. For reductive elimination, increased bisphosphine bite angles results in a decrease in the C-Ni-C angle and provides a destabilizing ground state effect that accelerates reductive elimination for sterically encumbered phosphine ligands. Despite the evident qualitative effect of increasing bisphosphine bite angles leading to reduced reductive elimination barriers (see Figure 4.6), weak correlation was found between bite angle and barriers (R^2=0.13 for all conformers). The poor ability of bite angle in predicting barriers was evident when comparing conformers with the same bisphosphine ligand and when comparing across the eight bisphosphine ligands studied (see Table 5.9 in Appendix B). These results suggest that steric size of an ancillary ligand is insufficient to predict reaction barriers in this system and more geometric information is needed to fully explain the ground state destabilization effect of increasing bisphosphine size.

Next, we searched for a geometry metric that more comprehensively describes the destabilization of the reactant geometry. τ_4', a geometry index parameter, uses the two largest valence angles at the metal center (the two C-Ni-P bond angles) to describe the square planarity of a given complex (see Equation 5.1 in Appendix B). For the studied set of catalyst conformers, τ_4' is similar to commonly used steric parameters (e.g., ligand bite angle and cone angle) in that it nominally increases as the steric bulk of an ancillary ligand increases. τ_4', however, provides a more complete description of ground state distortion because it includes all atoms coordinated to the nickel center rather than just the ancillary ligand. Sterically encumbered bisphosphine ligands

result in greater distortion to the square planar reactants for reductive elimination, leading to a better prediction of the ancillary ligand ground state effect on reductive elimination. The correlation between bite angle and τ_4' is moderate (R^2=0.40), which suggests that bite angle does not sufficiently describe the square planar distortion induced by increasing the side chain steric encumbrance and alkyl backbone length. For example, the correlation between barrier height and the bite angle and τ_4' geometry metrics for a set of all conformers generated from the eight bisphosphine ligands are 0.13 and 0.71, respectively. The supporting information (Table 5.9 in Appendix B) provides a comparison of correlations found between these two geometry metrics and calculated reductive elimination barriers and demonstrates that τ_4' has stronger correlation when comparing across all catalysts.

Figure 4.8 illustrates the relationship between reductive elimination barrier and τ_4', which was the metric that showed the largest correlation. While individual conformers (red points in Figure 4.8) provided some relationship to their individual activation energies, the most useful relationship is from the lowest energy conformer to the lowest energy transition state for a given ancillary ligand (blue points in Figure 4.8). The blue points therefore represent the most likely pathway for reductive elimination, as the complex would mostly exist in the lowest energy state prior to reaction, conformationally isomerize, and then pass through the lowest energy barrier. A moderate correlation (R^2=0.87) was found between reductive elimination barriers and τ_4' for the blue points. This suggests that the degree of distortion of the square planar complex encapsulates many of the chemical properties relevant to tuning the reductive elimination barrier height (bisphosphine bite angle, π-π stacking interactions, and steric interactions). Ultimately, however, a thorough conformer search of both reactants and transition states was necessary for identifying this structure-activity relationship.

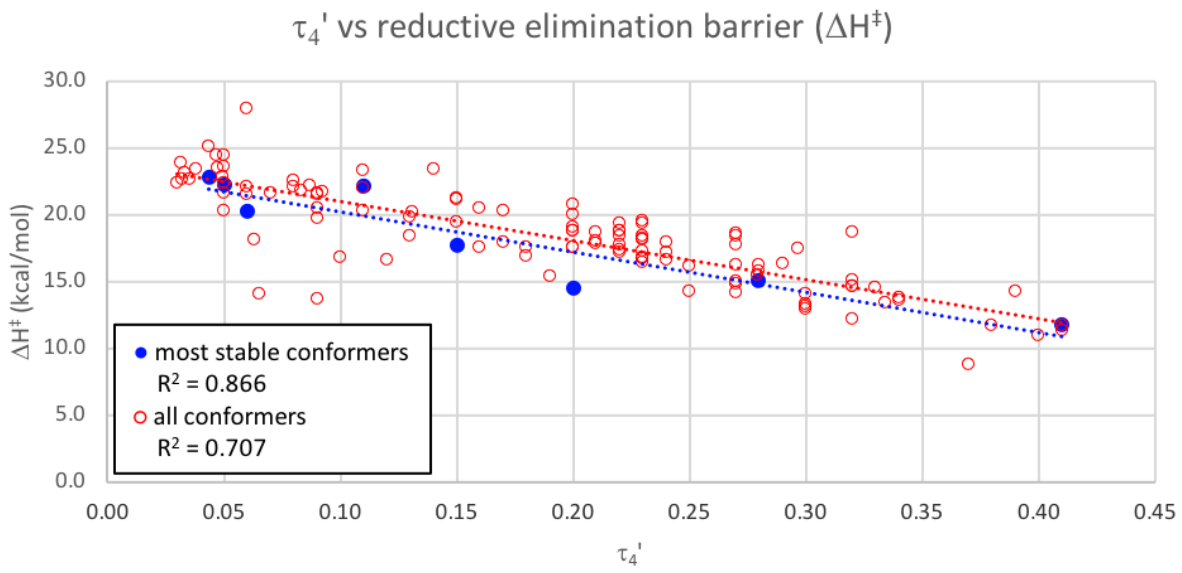

Figure 4.8: Linear relationship between reductive elimination enthalpy of activation and geometric τ_4' parameter.

4.4 Conclusions

The effects of conformational flexibility on reductive elimination for several representative nickel bisphospine catalysts were studied. Flexible bisphosphine ancillary ligands and rotations of thiophene reactive ligands together often allow for a large number of possible conformers for the intermediates that precede reductive elimination. The geometric and energetic variations found in these catalyst conformers gave rise to several unique reductive elimination pathways where the most stable conformers rarely produced the lowest enthalpy transition states. The range of reductive elimination reactant conformer energies was 2-9 kcal/mol, while the range of transition state energies was 4-7 kcal/mol. This high variance in reductive elimination barriers demonstrates that conformational analyses may be vital to accurately predicting reaction rates involving transition metal complexes with flexible ligands.

A number of intriguing, specific interactions between the bisphosphines and the thiophene reactive ligands were also uncovered in this study. For example, while bite angle increases from ethyl to propyl phosphine backbones, increasing the size of the side chains does not always increase bite angle. This is particularly true with phenyl side chains, which π-stack with the thiophene and reduce the bite angle compared to methyl. Care must be taken in considering the effects of phenyl-based bisphosphines but because of the significant variations in conformer energies when π-stacking is accounted for. In another example, there exist multiple alignments that are possible for the thiophene ligands, in addition to conformers of the ancillary ligand. The lone pair interactions between the sulfur atoms were found to be particularly important in this regard, as the reactant structures usually prefer and different orientation than the transition state. These mismatches between reactant state and transition state—where each state prefers specific orientations over others—gives a high degree of chemical complexity to the bisphosphine class of ligand. Further investigations will be required to better understand the generality of these effects, which are likely present in many related systems. In the future, we will continue to probe the exciting effects of conformers on the reactivity of transition metal catalysts.

4.5 Computational Details

A new conformer generation method designed for transition metal complexes was created to produce all reductive elimination intermediates. The eight catalyst conformer ensembles were generated using a combination of computational methods. Conformational isomers of the ancillary ligands were generated using the Confab method of OpenBabel,[43] which rotates all of the flexible bonds contained in the ancillary ligand. Next, ancillary ligand conformers are optimized with molecular mechanics methods and aligned to prime the ancillary ligand to bond to an optimized nickel dthiophene complex. The Growing String Method (GSM)[44] was then utilized to form two phosphorus-nickel bonds between the ancillary ligand and nickel dithiophene complex. All conformers generated with this workflow are then optimized with the PM6 semi-empirical method[45] and reoptimized using DFT. Energy thresholds are in place during all optimization steps to remove high energy structures and all conformers generated were compared via RMSD in XYZ structure to ensure uniqueness. Reductive elimination transition states from these conformers were then obtained using single-ended GSM.[46] Refer to section B.3 in Appendix B for a more detailed description of the conformer generation workflow.

All initial geometries for intermediates and transition states were obtained using the restricted framework in the gas phase and using the B3LYP-D3 density functional[47] and the 6-31G* basis set.[48–50] All stationary points were refined by single point calculations applying the B3LYP-D3 density functional and the 6-311G** basis set[51–53] as well as the SMD implicit solvent model[54–56] using THF as the solvent. All enthalpies listed are at typical catalytic conditions (298 K, 1 atm). Entropy corrections were omitted to avoid inherent inaccuracies of the harmonic oscillator approximation.

4.6 References

(1) Sperger, T.; Sanhueza, I. A.; Schoenebeck, F. Computation and Experiment: A Powerful Combination to Understand and Predict Reactivities. *Acc. Chem. Res.* **2016**, *49* (6), 1311–1319.

(2) Jindal, G.; Kisan, H. K.; Sunoj, R. B. Mechanistic Insights on Cooperative Catalysis through Computational Quantum Chemical Methods. *ACS Catal.* **2015**, *5* (2), 480–503.

(3) Lin, Z. Interplay between Theory and Experiment: Computational Organometallic and Transition Metal Chemistry. *Acc. Chem. Res.* **2010**, *43* (5), 602–611.

(4) Ryu, H.; Park, J.; Kim, H. K.; Park, J. Y.; Kim, S. T.; Baik, M. H. Pitfalls in Computational Modeling of Chemical Reactions and How to Avoid Them. *Organometallics* **2018**, *37* (19), 3228–3239.

(5) Tsang, A. S. K.; Sanhueza, I. A.; Schoenebeck, F. Combining Experimental and Computational Studies to Understand and Predict Reactivities of Relevance to Homogeneous Catalysis. *Chem. - A Eur. J.* **2014**, *20* (50), 16432–16441.

(6) Foscato, M.; Venkatraman, V.; Occhipinti, G.; Alsberg, B. K.; Jensen, V. R. Automated Building of Organometallic Complexes from 3D Fragments. *J. Chem. Inf. Model.* **2014**, *54* (7), 1919–1931.

(7) Bartol, J.; Comba, P.; Melter, M.; Zimmer, M. Conformational Searching of Transition Metal Compounds. *J. Comput. Chem.* **1999**, *20* (14), 1549–1558.

(8) Albright, T. A. Rotational Barriers and Conformations in Transition Metal Complexes. *Acc. Chem. Res.* **1982**, *15* (5), 149–155.

(9) Armstrong, A.; Boto, R. A.; Dingwall, P.; Contreras-García, J.; Harvey, M. J.; Mason, N. J.; Rzepa, H. S. The Houk–List Transition States for Organocatalytic Mechanisms Revisited. *Chem. Sci.* **2014**, *5* (5), 2057–2071.

(10) Liu, C.; Besora, M.; Maseras, F. Computational Characterization of the Origin of Selectivity in Cycloaddition Reactions Catalyzed by Phosphoric Acid Derivatives. *Chem. - An Asian J.* **2016**, *11* (3), 411–416.

(11) Brown, J. M.; Deeth, R. J. Is Enantioselectivity Predictable in Asymmetric Catalysis? *Angew. Chemie Int. Ed.* **2009**, *48* (25), 4476–4479.

(12) Butts, C. P.; Filali, E.; Lloyd-Jones, G. C.; Norrby, P.-O.; Sale, D. A.; Schramm, Y. Structure-Based Rationale for Selectivity in the Asymmetric Allylic Alkylation of Cycloalkenyl Esters Employing the Trost 'Standard Ligand' (TSL): Isolation, Analysis and Alkylation of the Monomeric Form of the Cationic η 3 -Cyclohexenyl Complex [(η 3 - C. *J. Am. Chem. Soc.* **2009**, *131* (29), 9945–9957.

(13) Besora, M.; Braga, A. A. C.; Ujaque, G.; Maseras, F.; Lledós, A. The Importance of Conformational Search: A Test Case on the Catalytic Cycle of the Suzuki–Miyaura Cross-Coupling. *Theor. Chem. Acc.* **2011**, *128* (4–6), 639–646.

(14) Minenkov, Y.; Sharapa, D. I.; Cavallo, L. Application of Semiempirical Methods to Transition Metal Complexes: Fast Results but Hard-to-Predict Accuracy. *J. Chem. Theory Comput.* **2018**, *14* (7), 3428–3439.

(15) Tu, T.; Hou, X. L.; Dai, L. X. Highly Regio- and Enantioselective Heck Reaction of N-Methoxycarbonyl-2- Pyrroline with Planar Chiral Diphosphine-Oxazoline Ferrocenyl Ligands. *Org. Lett.* **2003**, *5* (20), 3651–3653.

(16) Gao, K.; Lee, P. S.; Fujita, T.; Yoshikai, N. Cobalt-Catalyzed Hydroarylation of Alkynes through Chelation-Assisted C-H Bond Activation. *J. Am. Chem. Soc.* **2010**, *132* (35), 12249–12251.

(17) den Hartog, T.; Harutyunyan, S. R.; Font, D.; Minnaard, A. J.; Feringa, B. L. Catalytic Enantioselective 1,6-Conjugate Addition of Grignard Reagents to Linear Dienoates. *Angew. Chemie Int. Ed.* **2008**, *47* (2), 398–401.

(18) Ilies, L.; Matsubara, T.; Ichikawa, S.; Asako, S.; Nakamura, E. Iron-Catalyzed Directed Alkylation of Aromatic and Olefinic Carboxamides with Primary and Secondary Alkyl Tosylates, Mesylates, and Halides. *J. Am. Chem. Soc.* **2014**, *136* (38), 13126–13129.

(19) Chen, J. F.; Li, C. Enol Ester Synthesis via Cobalt-Catalyzed Regio- and Stereoselective Addition of Carboxylic Acids to Alkynes. *Org. Lett.* **2018**, *20* (21), 6719–6724.

(20) Leone, A. K.; McNeil, A. J. Matchmaking in Catalyst-Transfer Polycondensation: Optimizing Catalysts Based on Mechanistic Insight. *Acc. Chem. Res.* **2016**, *49* (12), 2822–2831.

(21) Lanni, E. L.; Locke, J. R.; Gleave, C. M.; McNeil, A. J. Ligand-Based Steric Effects in Ni-Catalyzed Chain-Growth Polymerizations Using Bis(Dialkylphosphino)Ethanes. *Macromolecules* **2011**, *44* (13), 5136–5145.

(22) Lanni, E. L.; McNeil, A. J. Evidence for Ligand-Dependent Mechanistic Changes in Nickel-Catalyzed Chain-Growth Polymerizations. *Macromolecules* **2010**, *43* (19), 8039–8044.

(23) He, W.; Patrick, B. O.; Kennepohl, P. Identifying the Missing Link in Catalyst Transfer Polymerization. *Nat. Commun.* **2018**, *9* (1), 3866.

(24) Baker, M. A.; Tsai, C.-H.; Noonan, K. J. T. Diversifying Cross-Coupling Strategies, Catalysts and Monomers for the Controlled Synthesis of Conjugated Polymers. *Chem. - A Eur. J.* **2018**, *24* (50), 13078–13088.

(25) Okuniewski, A.; Rosiak, D.; Chojnacki, J.; Becker, B. Coordination Polymers and Molecular Structures among Complexes of Mercury(II) Halides with Selected 1-Benzoylthioureas. *Polyhedron* **2015**, *90*, 47–57.

(26) Yang, L.; Powell, D. R.; Houser, R. P. Structural Variation in Copper^{I} Complexes with Pyridylmethylamide Ligands: Structural Analysis with a New Four-Coordinate Geometry Index, τ_4. *Dalt. Trans.* **2007**, No. 9, 955–964.

(27) Clavier, H.; Nolan, S. P. Percent Buried Volume for Phosphine and N-Heterocyclic Carbene Ligands: Steric Properties in Organometallic Chemistry. *Chem. Commun.* **2010**, *46* (6), 841–861.

(28) Algarra, A. G.; Basallote, M. G.; Castillo, C. E.; Clares, M. P.; Ferrer, A.; García-España, E.; Llinares, J. M.; Máñez, M. A.; Soriano, C. Geometric Isomerism in Pentacoordinate Cu 2+ Complexes: Equilibrium, Kinetic, and Density Functional Theory Studies Reveal the Existence of Equilibrium between Square Pyramidal and Trigonal Bipyramidal Forms for a Tren-Derived Ligand. *Inorg. Chem.* **2009**, *48* (3), 902–914.

(29) Koehne, I.; Graw, N.; Teuteberg, T.; Herbst-Irmer, R.; Stalke, D. Introducing NacNac-Like Bis(4,6-Isopropylbenzoxazol-2-yl)Methanide in s-Block Metal Coordination. *Inorg. Chem.* **2017**, *56* (24), 14968–14978.

(30) Dierkes, P.; van Leeuwen, P. W. N. M. The Bite Angle Makes the Difference: A Practical Ligand Parameter for Diphosphine Ligands. *J. Chem. Soc. Dalt. Trans.* **1999**, *65* (10), 1519–1530.

(31) van Leeuwen, P. W. N. M.; Kamer, P. C. J.; Reek, J. N. H.; Dierkes, P. Ligand Bite Angle Effects in Metal-Catalyzed C−C Bond Formation. *Chem. Rev.* **2000**, *100* (8), 2741–2770.

(32) Dierkes, P.; van Leeuwen, P. W. N. M. The Bite Angle Makes the Difference: A Practical Ligand Parameter for Diphosphine Ligands. *J. Chem. Soc. Dalt. Trans.* **1999**, No. 10, 1519–1530.

(33) Yamamoto, K.; Momose, S.; Funahashi, M.; Ebata, S.; Ohmura, H.; Komatsu, H.; Miyazawa, M. New Ligands with a Wide Bite Angle. Efficient Catalytic Activity in the Rh(I)-Catalyzed Hydroformylation of Olefins. *Chem. Lett.* **1994**, *23* (2), 189–192.

(34) Kranenburg, M.; van der Burgt, Y. E. M.; Kamer, P. C. J.; van Leeuwen, P. W. N. M.; Goubitz, K.; Fraanje, J. New Diphosphine Ligands Based on Heterocyclic Aromatics Inducing Very High Regioselectivity in Rhodium-Catalyzed Hydroformylation: Effect of the Bite Angle. *Organometallics* **1995**, *14* (6), 3081–3089.

(35) Casey, C. P.; Whiteker, G. T.; Melville, M. G.; Petrovich, L. M.; Gavney, J. A.; Powell, D. R. Diphosphines with Natural Bite Angles near 120.Degree. Increase Selectivity for n-Aldehyde Formation in Rhodium-Catalyzed Hydroformylation. *J. Am. Chem. Soc.* **1992**,

114 (14), 5535–5543.

(36) Kawabata, Y.; Hayashi, T.; Ogata, I. Platinum–diphosphine–tin Systems as Active and Selective Hydroformylation Catalysts. *J. Chem. Soc., Chem. Commun.* **1979**, No. 10, 462–463.

(37) Hayashi, T.; Kawabata, Y.; Isoyama, T.; Ogata, I. Platinum Chloride–Diphosphine–Tin(II) Halide Systems as Active and Selective Hydroformylation Catalysts. *Bull. Chem. Soc. Jpn.* **1981**, *54* (11), 3438–3446.

(38) Kranenburg, M.; Kamer, P. C. J.; van Leeuwen, P. W. N. M.; Vogt, D.; Keim, W. Effect of the Bite Angle of Diphosphine Ligands on Activity and Selectivity in the Nickel-Catalysed Hydrocyanation of Styrene. *J. Chem. Soc. Chem. Commun.* **1995**, No. 21, 2177.

(39) Goertz, W.; Kamer, P. C. J.; van Leeuwen, P. W. N. M.; Vogt, D. Application of Chelating Diphosphine Ligands in the Nickel-Catalysed Hydrocyanation of Alk-l-Enes and ω-Unsaturated Fatty Acid Esters. *Chem. Commun.* **1997**, No. 16, 1521–1522.

(40) Trost, B. M.; Van Vranken, D. L.; Bingel, C. A Modular Approach for Ligand Design for Asymmetric Allylic Alkylations via Enantioselective Palladium-Catalyzed Ionizations. *J. Am. Chem. Soc.* **1992**, *114* (24), 9327–9343.

(41) Hayashi, T.; Tamao, K.; Katsuro, Y.; Nakae, I.; Kumada, M. Asymmetric Hydrosilylation of Olefins Catalyzed by a Chiral Ferrocenylphosphine-Palladium Complex. Asymmetric Synthesis of Optically Active Alcohols and Bromides from Olefins. *Tetrahedron Lett.* **1980**, *21* (19), 1871–1874.

(42) Hayashi, T.; Konishi, M.; Kobori, Y.; Kumada, M.; Higuchi, T.; Hirotsu, K. Dichloro[1,1'-Bis(Diphenylphosphino)Ferrocene]Palladium(II): An Effective Catalyst for Cross-Coupling of Secondary and Primary Alkyl Grignard and Alkylzinc Reagents with Organic Halides. *J. Am. Chem. Soc.* **1984**, *106* (1), 158–163.

(43) O'Boyle, N. M.; Banck, M.; James, C. A.; Morley, C.; Vandermeersch, T.; Hutchison, G. R. Open Babel: An Open Chemical Toolbox. *J. Cheminform.* **2011**, *3* (1), 33.

(44) Zimmerman, P. M. Growing String Method with Interpolation and Optimization in Internal Coordinates: Method and Examples. *J. Chem. Phys.* **2013**, *138* (18), 184102.

(45) Stewart, J. J. P. Optimization of Parameters for Semiempirical Methods V: Modification of NDDO Approximations and Application to 70 Elements. *J. Mol. Model.* **2007**, *13* (12), 1173–1213.

(46) Zimmerman, P. M. Single-Ended Transition State Finding with the Growing String Method. *J. Comput. Chem.* **2015**, *36* (9), 601–611.

(47) Grimme, S.; Antony, J.; Ehrlich, S.; Krieg, H. A Consistent and Accurate Ab Initio

Parametrization of Density Functional Dispersion Correction (DFT-D) for the 94 Elements H-Pu. *J. Chem. Phys.* **2010**, *132* (15), 154104.

(48) Hariharan, P. C.; Pople, J. A. The Influence of Polarization Functions on Molecular Orbital Hydrogenation Energies. *Theor. Chim. Acta* **1973**, *28* (3), 213–222.

(49) Francl, M. M.; Pietro, W. J.; Hehre, W. J.; Binkley, J. S.; Gordon, M. S.; DeFrees, D. J.; Pople, J. A. Self-Consistent Molecular Orbital Methods. XXIII. A Polarization-Type Basis Set for Second-Row Elements. *J. Chem. Phys.* **1982**, *77* (7), 3654–3665.

(50) Rassolov, V. A.; Ratner, M. A.; Pople, J. A.; Redfern, P. C.; Curtiss, L. A. 6-31G* Basis Set for Third-Row Atoms. *J. Comput. Chem.* **2001**, *22* (9), 976–984.

(51) Krishnan, R.; Binkley, J. S.; Seeger, R.; Pople, J. A. Self-consistent Molecular Orbital Methods. XX. A Basis Set for Correlated Wave Functions. *J. Chem. Phys.* **1980**, *72* (1), 650–654.

(52) McLean, A. D.; Chandler, G. S. Contracted Gaussian Basis Sets for Molecular Calculations. I. Second Row Atoms, Z =11–18. *J. Chem. Phys.* **1980**, *72* (10), 5639–5648.

(53) Curtiss, L. A.; McGrath, M. P.; Blaudeau, J.; Davis, N. E.; Binning, R. C.; Radom, L. Extension of Gaussian-2 Theory to Molecules Containing Third-row Atoms Ga–Kr. *J. Chem. Phys.* **1995**, *103* (14), 6104–6113.

(54) Cammi, R.; Tomasi, J. Remarks on the Use of the Apparent Surface Charges (ASC) Methods in Solvation Problems: Iterative versus Matrix-Inversion Procedures and the Renormalization of the Apparent Charges. *J. Comput. Chem.* **1995**, *16* (12), 1449–1458.

(55) Tomasi, J.; Mennucci, B.; Cammi, R. Quantum Mechanical Continuum Solvation Models. *Chem. Rev.* **2005**, *105* (8), 2999–3093.

(56) Aleksandr V. Marenich, Christopher J. Cramer, and D. G. T. Universal Solvation Model Based on Solute Electron Density and on a Continuum Model of the Solvent Defined by the Bulk Dielectric Constant and Atomic Surface Tensions. *J. Phys. Chem. B* **2009**, *113* (18), 6378–6396.

Chapter 5: Final Remarks

Advances in computing power, the development of faster and more accurate computational methods, and techniques for automated exploration of relevant chemical space are accelerating the pace of chemical discovery and expanding our chemical knowledge. Although construction of reasonable models that provide meaningful chemical explanations is a difficult task when complex chemistry is involved, the number of tools available to computational chemists and the amount of information of related systems is increasing. The advancements in these fields enables directed exploration of relevant chemical spaces to gradually improve our understanding of chemical reactivity. Increased accessibility of computational and automation tools will lead to a stronger synergy between experiment and theory. The pace of these advancements allows computational chemistry to inch closer to a more equal relationship between experiment and theory where each half guides the other and both synergistically discover new chemistry in real time.

5.1 Research Summary

The studies contained in this work demonstrate the utility of simulated reaction path exploration to investigate chemical reactivity. The brief computational studies found in Chapter 2 were used to reinforce or explain chemical observations for various polymerization reactions. In this chapter, a method developed by Souther and McNeil for generating olefin-thiophene block copolymer was described that involved a single catalyst switching between two polymerizations with distinct mechanisms. The switching mechanism for the olefin-thiophene block copolymerization was computed and revealed a high reductive elimination barrier that

occurs when the catalyst initiates thiophene polymerization after olefin has been polymerized. This study helped to identify the difficulties associated with the switching mechanism and identified the high-barrier reductive elimination as the source of incomplete switching. The combined experimental and computational work of this study identified the problem step with a single pot olefin-thiophene copolymerization and may be useful in designing a new catalytic system that can seamlessly switch between the two mechanisms to generate polymers with broader monomer scope and more control over copolymer sequence and size.

Next, a study by Leone and McNeil revealed how diimine side chains can drastically affect the living nature of nickel catalysts during 3-hexylthiophene polymerization. Experimental polymerization results showed drastically lower molecular weight and higher dispersity for diimine catalysts with naphthyl side chains compared to less sterically encumbered proximal side chains. This curious result was thought to be the result of the naphthyl side chain catalysts exhibiting a disrupted catalyst-polymer π-complex during polymerization. We turned to computational studies of the productive ring walking step and the unproductive dissociation pathway to better understand the catalyst-polymer π-complex and what characteristics of this complex lead to poor CTP performance. Surprisingly, ring walking pathways for all investigated catalysts had low barriers with stable π-complex intermediates. Separated catalyst and polymer geometries were obtained in order to calculate the catalyst-polymer binding energies and revealed a self-association between nickel and naphthyl side chains. This association was unique to catalysts featuring the flexible naphthyl side chains and not found in catalysts with aliphatic or mesityl groups in the side chain. This interaction between the ancillary ligand and nickel is likely the source of poor CTP performance of these catalysts. This heuristic can be used when designing prospective CTP catalysts to avoid facile catalyst-polymer dissociation via self-

association between nickel and pendant groups of the ancillary ligand. This study demonstrated that flexible and labile pendant groups of ancillary ligands can destabilize the important catalyst-polymer π-complex and result in poor CTP performance.

The last study found in Chapter 2 describes the enantioselective polymerization of propylene oxide catalyzed by a bimetallic chromium salalen catalyst developed by the Coates group. This reaction has novel utility because enantiomers of the bimetallic catalyst can be prepared in a single pot, and each enantiomeric form of the catalyst reacts with a matching enantiomeric propylene oxide monomer. The catalyst is also compatible with diol chain shuttling agents, which can be added to the polymerization to generate isotactic poly(propylene oxide) with low dispersity and controlled length of stereoblocks. Due to the large number of possible catalytically active species, computations were used to identify the most stable form of the catalyst with considerations for chromium spin state, ancillary ligand conformational flexibility, additives, and binding sites of the monomer. We identified a stable form of the *S* enantiomer of the catalyst that preferentially reacts with (*S*)-propylene oxide by over 5 kcal/mol. Comparing ring-opening transition state geometries for the (*S*) and (*R*) enantiomers illustrated the enantioselectivity of the bimetallic catalytic cleft where the mismatched (*R*) enantiomer exhibits a destabilizing steric interaction with the naphthyl linker group of the catalyst. Ultimately, this computational study provides a useful example for how to simulate enantioselective catalyzed reactions.

Chapter 3 of this work highlighted the transmetalation reaction of nickel-catalyzed thiophene polymerization. This study focused on building realistic models of reagents and reactive intermediates in order to better understand how the transmetalation reaction and active catalytic intermediates change during the polymerization cycle. In this study, we found that

adding two explicit THF solvent molecules form strong associations with the magnesium atom of an unsolvated Grignard reagent (binding energies of ~10 kcal/mol for each association with THF). The strong binding of the first two THF molecules suggests that explicit solvation of Grignard reagents is needed to model accurate steric and electronic effects for related reactions. Another aspect of the transmetalation reaction is that the catalyst spin-state and geometry changes during the catalytic cycle. We determined that the catalytically active nickel species switches between a high-spin state with a tetrahedral geometry and a low-spin state square planar geometry during polymerization. This is the result of the alternating crystal field strength of the bromide (weak) and thiophene (strong) reactive ligands. We found that although the spin state and geometry of the reactive nickel intermediate alternated during polymerization, transmetalation transition states were always more stable in a high-spin, tetrahedral geometry. No previous studies on nickel-catalyzed Kumada coupling reactions have accounted for the high-spin, tetrahedral pathway to the best of our knowledge. Lastly, we found that ancillary ligand steric effects greatly modulate transmetalation barrier. Increasing the steric bulk of the ancillary ligand side chain by a single methyl group led to a significant increase in transmetalation barriers, providing further insight toward designing efficient nickel catalysts for Kumada coupling reactions. This study will hopefully provide a framework for modeling similar reactions in the context of catalyzed polymerization reactions and Kumada coupling reactions.

Chapter 4 focused on often-neglected conformational effects and the reaction barrier errors that arise from them. This study illustrated that ligand flexibility can dramatically change for related ancillary ligands and highlighted how conformational effects induce large ground and transition state effects in a ligand-dependent fashion. Conformational variation was generally described with geometry metrics to illustrate the differences in catalyst ancillary ligands. Fine

chemical details about the most stable reactants and transition states for reductive elimination were identified and could provide useful guidelines for future studies of related reactions. This study demonstrated that changing the ancillary ligand of a catalyst can also change the number, geometry, and relative stability of the total ensemble of accessible conformers. Finally, the metrics used to describe how the conformer geometries vary were also used to predict the lowest energy reductive elimination barriers. We identified that a metric describing the degree of distortion of the square planar reactant geometries, τ_4', had strong correlation with reductive elimination barrier height. This work demonstrates that conformational variation results in significant energetic and geometric variation for ground and transition state structures. These conformational studies, however, are useful in identifying ground state metrics that can predict reaction barrier heights.

5.2 Future Considerations for Related Works

Although the computational studies contained in this work make several contributions to a better understanding of the studied organometallic polymerization reactions, many important mechanistic questions remain. An efficient, single-pot method for synthesizing olefin-thiophene copolymers remains elusive due to the high barrier reductive elimination when switching between the two distinct polymerization mechanism (Section 2.1). An efficient switch may be possible via switching the ancillary ligand catalytic intermediates with growing polymer chains to activate the species toward the polymerization of a particular monomer. For example, switching between bisphosphine and diimine ancillary ligands could promote thiophene and olefin polymerization respectively. Additionally, identifying catalyst-polymer dissociation mechanisms may provide the information needed to design catalysts that prevent the dissociation and chain termination from occurring. For example, the ideal catalyst-polymer combination

would exhibit a stable π-complex that was resistant to dissociation but labile enough to facilitate ring-walking across the conjugated backbone. Catalyst-polymer dissociation mechanisms may be unique to the types of catalysts and π-conjugated monomers used (e.g. metal-ligand self-association described in Section 2.2). Despite this, elucidation of these important pathways and development of metrics describing catalyst-monomer compatibility may lead to the design of new catalysts capable of polymerizing monomers that demonstrate improved materials properties (e.g. charge-mobility, charge transfer, tunable band gap, etc.).

Enantioselective epoxide polymerization via bimetallic chromium catalysts (described in Section 2.3) is possible due to the selectivity of the catalysts but also due to the catalyst's compatibility with diol chain transfer agents. The mechanism of chain transfer, which enables controlled lengths of poly(propylene oxide) stereoblocks, and metrics that predict polymerization and chain transfer are not yet known. Computational investigation of these pathways and discovery of chemical descriptors that control their relative rates could enable unique control of copolymerization. For example, tandem catalysis could be used to generate currently inaccessible copolymer sequences with increased monomer scope via chain shuttling growing polymers between two or more catalysts.

Chemical considerations for more accurate computational models of nickel-catalyzed transmetalation reactions are outlined in Chapter 3. Transmetalation is often a crucial step in cross-coupling reactions, and discovering predictive structure-reactivity relationships would greatly broaden the utility of such reactions. Our computational results suggest that transmetalation is only operative when the nickel catalyst adopts a high-spin, tetrahedral geometry, but this result has not been confirmed by experiment. A combined computational and experimental study that investigates a more numerous and diverse set of nickel transmetalation

catalysts could definitively establish the operative pathway for transmetalation. Better understanding of how low-spin and high-spin states of nickel catalysts affect reactivity could also provide an additional catalyst design tool where ligand-dependent spin states are used to control catalyst reactivity and selectivity. The demonstrated preference for the examined nickel catalysts to undergo transmetalation in the high-spin state could be applied to accelerating a diverse set of catalyzed reactions that feature a similar spin state preference of the metal center (e.g. transmetalation and reductive elimination). Investigation of a diverse set of nickel transmetalation catalysts would also prove useful in discovering steric and electronic parameters that can be used to better design catalysts for desired reactions.

The conformational study of nickel bisphosphine catalysts in Chapter 4 described how conformational effects generates several unique pathways for a single reaction. This investigation revealed that the most stable conformer rarely produces the pathways with the lowest energy transition state, which could lead to high inaccuracy of calculated barriers. Designing computational methodologies that identify and efficiently sample the conformational flexibility of various chemical systems would be a useful tool for providing accurate computational predictions. Such methods could also produce large datasets used to more rapidly discover structure-reactivity relationships and identify the most useful chemical descriptors for certain reactions.

5.3 Final Thoughts

The studies contained in this work demonstrate that advances in computational reaction exploration methods can be used to greatly inform experiment and chemical understanding. Accurate chemical models enable the discovery of relationships between meaningful chemical descriptors and chemical reactivity and selectivity. These heuristics are powerful tools for

expanding our chemical knowledge. Significant challenges remain in the way of accurately modeling complex chemical reactions and being able to efficiently predict chemical reactivity. These challenges, however, are becoming increasingly easier to overcome via improved computational modeling and better chemical understanding. Increasing computational power is enabling the study of larger systems that approach real chemistry conducted in the lab. Improved computational methods and more sophisticated chemical models are leading to more accurate predictions. Additionally, automation of reaction path discovery is making computational chemistry much more accessible than in the past. These advancements will improve the synergy between theory and experiment in such a way that allows for accelerated discovery of insightful structure-reactivity relationships and novel chemical reactions.

Appendix A: Supporting Information for Chapter 3

A.1 Experimental Details

The following experimental studies were performed by Amanda K. Leone.

A.1.1 Experiment Materials

Flash chromatography was performed on SiliCycle silica gel (40–63 μm). Thin layer chromatography was performed on Merck TLC plates (pre-coated with silica gel 60 F254). iPrMgCl (2M in THF) was purchased from Aldrich and titrated using salicylaldehyde phenylhydrazone. All other reagent grade materials and solvents were purchased from Aldrich, Acros, or Fisher and were used without further purification unless otherwise noted. Tetrahydrafuran (THF) and dichloromethane (DCM) were dried and deoxygenated using an Innovative Technology (IT) solvent purification system composed of activated alumina, copper catalyst, and molecular sieves. Acetonitrile (ACN) was dried over molecular sieves (4Å). N-Bromosuccinimide (NBS) was recrystallized from hot water. The glovebox in which specified procedures were carried out was an MBraun LABmaster 130 with a N_2 atmosphere.

A.1.2 General Experimental Procedure

NMR Spectroscopy: Unless otherwise noted, ^{1}H, and ^{13}C NMR spectra for all compounds were acquired at rt. Chemical shift data are reported in units of δ (ppm) relative to tetramethylsilane (TMS) and referenced with residual solvent. Multiplicities are reported as follows: singlet (s), doublet (d), doublet of doublets (dd), triplet (t), quartet (q), multiplet (m), broad signal (br). Residual water is denoted by an asterisk (*). Compounds **SI2**,[80] **L^2**,[80] and **L^1NiBr_2**[80] were prepared according to modified literature procedures.

Mass Spectrometry: High-resolution mass spectrometry data were obtained on a Micromass AutoSpec Ultima Magnetic Sector mass spectrometer.

iPrMgCl titration:[81] In a glovebox, salicylaldehyde phenylhydrazone (106 mg, 0.500 mmol) was dissolved in THF (5.0 mL) to make a 0.10 M solution. For titration, iPrMgCl was added dropwise using a 100 µL syringe into a known amount of the salicylaldehyde phenylhydrazone solution. Titration was complete when the solution turned bright orange.

A.1.3 Synthetic Procedures

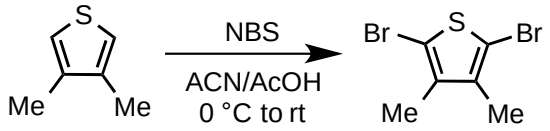

SI1

2,5-dibromo-3,4-dimethylthiophene (SI1). In a 50 mL round-bottom flask, 3,4-dimethylthiophene (0.885 g, 7.90 mmol, 1.00 equiv) was dissolved in ACN/AcOH (24 mL/1.4 mL) and cooled 0 °C using an ice-water bath for 5 min. Then NBS (3.09 g, 17.4 mmol, 2.20 equiv) was added over 5 min. The stirring solution was warmed to rt over 2.5 h, and then transferred to a separatory funnel using Et_2O (20 mL). The organic layer was washed with sat. aq. Na_2CO_3 (3 x 15 mL) and brine (3 x 20 mL), then dried over $MgSO_4$, concentrated using rotary evaporation, and purified by filtering through a silica plug and a neutral alumina plug using hexanes. Drying under reduced pressure resulted in 1.73 g of **SI1** as a pale-yellow oil (82 % yield). HRMS (EI): Calcd. for $C_6H_6Br_2S$ [M+] 267.8557; found 267.8566.

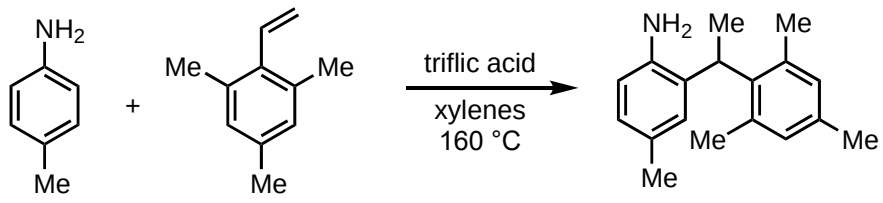

SI2

***rac*-4-methyl-2-(sec-(2,4,6-trimethylphenethyl)aniline (SI2)**. To a 15 mL bomb flask equipped with a stir bar, *p*-toluidine (1.36 g, 13.0 mmol, 1.50 equiv) was dissolved in xylenes (1.1 mL). Subsequently, 2,4,6-trimethylstyrene (1.40 mL, 8.64 mmol, 1.00 equiv) and triflic acid (16 µL, 2.6 mmol, 0.20 equiv) were added to the reaction flask, which was sealed and placed behind a blast shield. After 17 h at 160 °C, the heterogeneous mixture was transferred to a 250 mL round-bottom flask with EtOAc (50 mL), concentrated in vacuo, and purified via column chromatography on silica gel (100% hexanes to 80:20 hexanes/EtOAc (v:v)) to give a brown oil which was recrystallized in 10:1 hexanes:EtOAc (v:v) to yield 1.25 g of **SI2** as a white solid (57% yield). HRMS (ESI+): Calcd. for $C_{18}H_{23}N$ [M+H]+ 254.1903; found 254.1899.

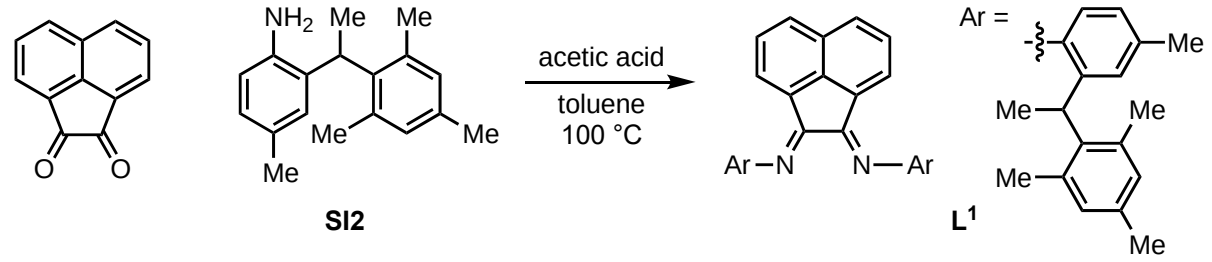

***rac*-ArN=C(An)C=NAr (Ar = 4-methyl-2-(sec-(2,4,6-trimethylphenethyl)phenyl; An = acenaphthene) (L^1).** To a 20 mL vial equipped with a stir bar, acenaphthenequinone (438 mg, 2.41 mmol, 0.490 equiv) and amine **SI2** (1.25 mg, 4.92 mmol, 1.00 equiv) were dissolved in toluene (2.8 mL) and glacial acetic acid (5.50 mL, 96.0 mmol, 19.5 equiv). After 3 h at 100 °C, the resulting heterogeneous mixture was filtered over a fine frit, washed with cold MeOH (3 x 10 mL) and cold hexanes (3 x 10 mL) and dried under reduced pressure to give 1.13 g of $\mathbf{L^1}$ as a yellow powder (72% yield). HRMS (ESI+): Calcd. for $C_{48}H_{48}N_2$ [M+H]+ 653.3890; found 653.3897.

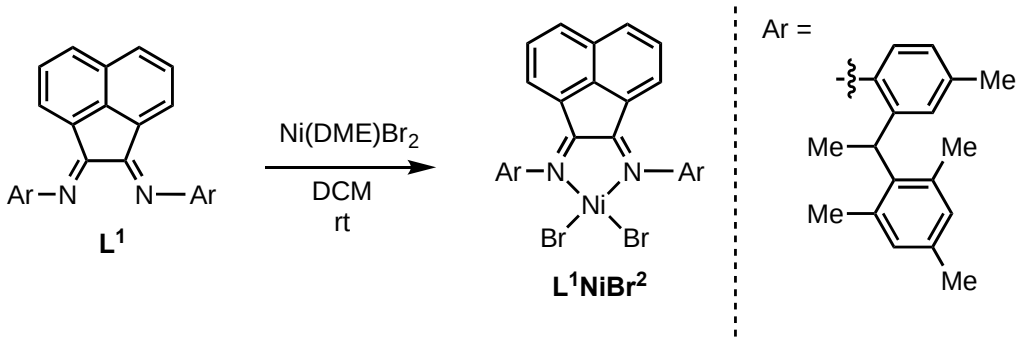

***rac*-(ArN=C(An)C=NAr)$NiBr_2$ (Ar = 4-methyl-2-(sec-(2,4,6-trimethylphenethyl)-phenyl; An = acenaphthene) (L^1NiBr_2).** In a 50 mL Schlenk flask equipped with a stir bar, Ni(II)

bromide ethylene glycol dimethyl ether ($Ni(DME)Br_2$, 156 mg, 0.505 mmol, 1.17 equiv) and diimine $\mathbf{L^1}$ (300. mg, 0.430 mmol, 1.00 equiv) were dissolved in dry methylene chloride (DCM, 15 mL) and stirred at rt under N_2 for 16 h. Then, the dark maroon liquid was concentrated, dissolved in DCM (20 mL), filtered through a celite plug, layered with pentane (60 mL), and cooled to –20 °C. The resulting solid was collected by filtration over a course frit, washed with cold pentane (3 x 10 mL), and dried under reduced pressure to give 338 mg of $\mathbf{L^1NiBr_2}$ as a dark maroon solid (90% yield).

A.1.4 NMR Spectra

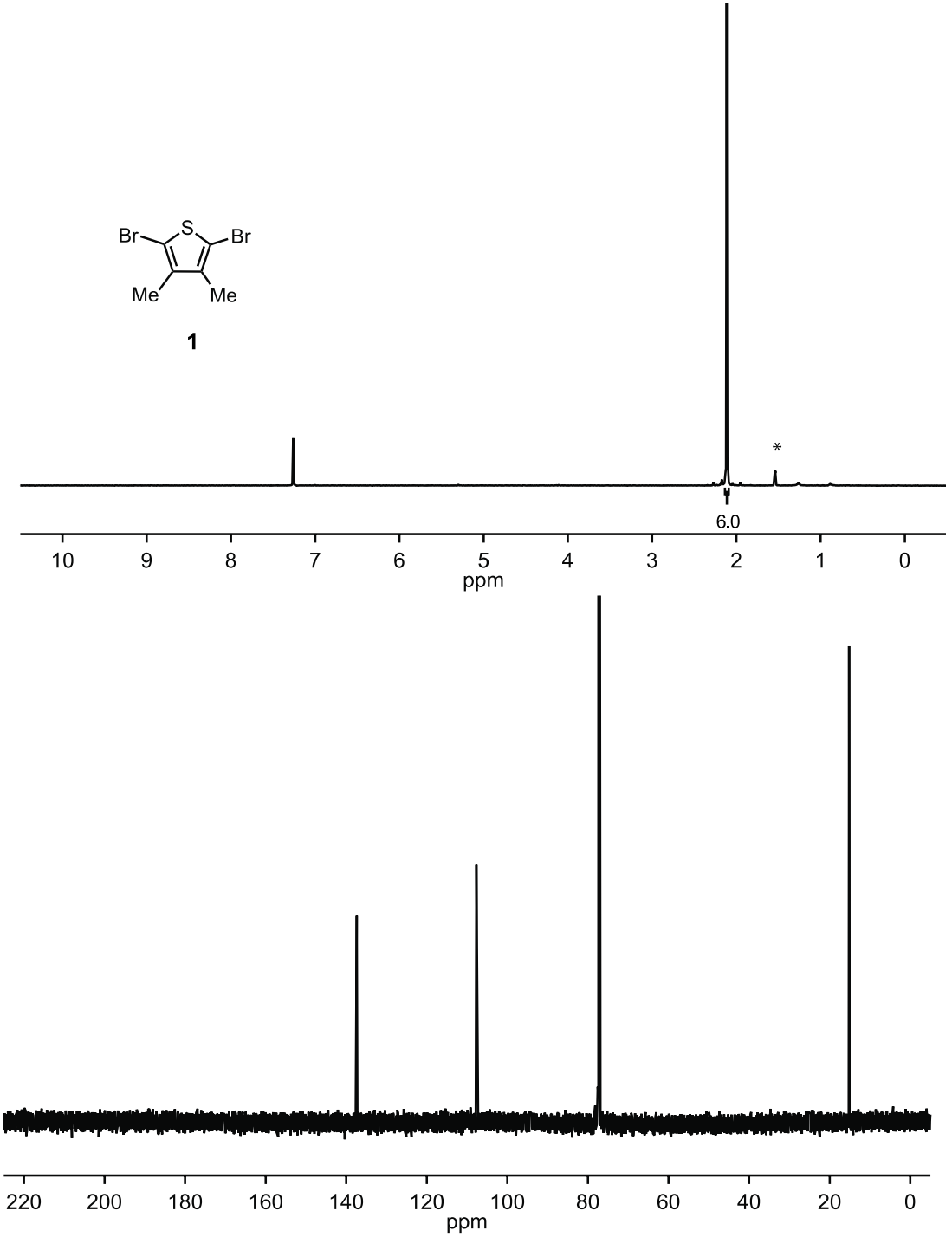

Figure 5.1: ^{1}H and ^{13}C NMR Spectra of 1. ^{1}H NMR (400 MHz, $CDCl_3$) δ 2.11 (s, 6H). ^{13}C NMR (176 MHz, $CDCl_3$) δ 137.38, 107.68, 15.19. Taken by Amanda Leone.

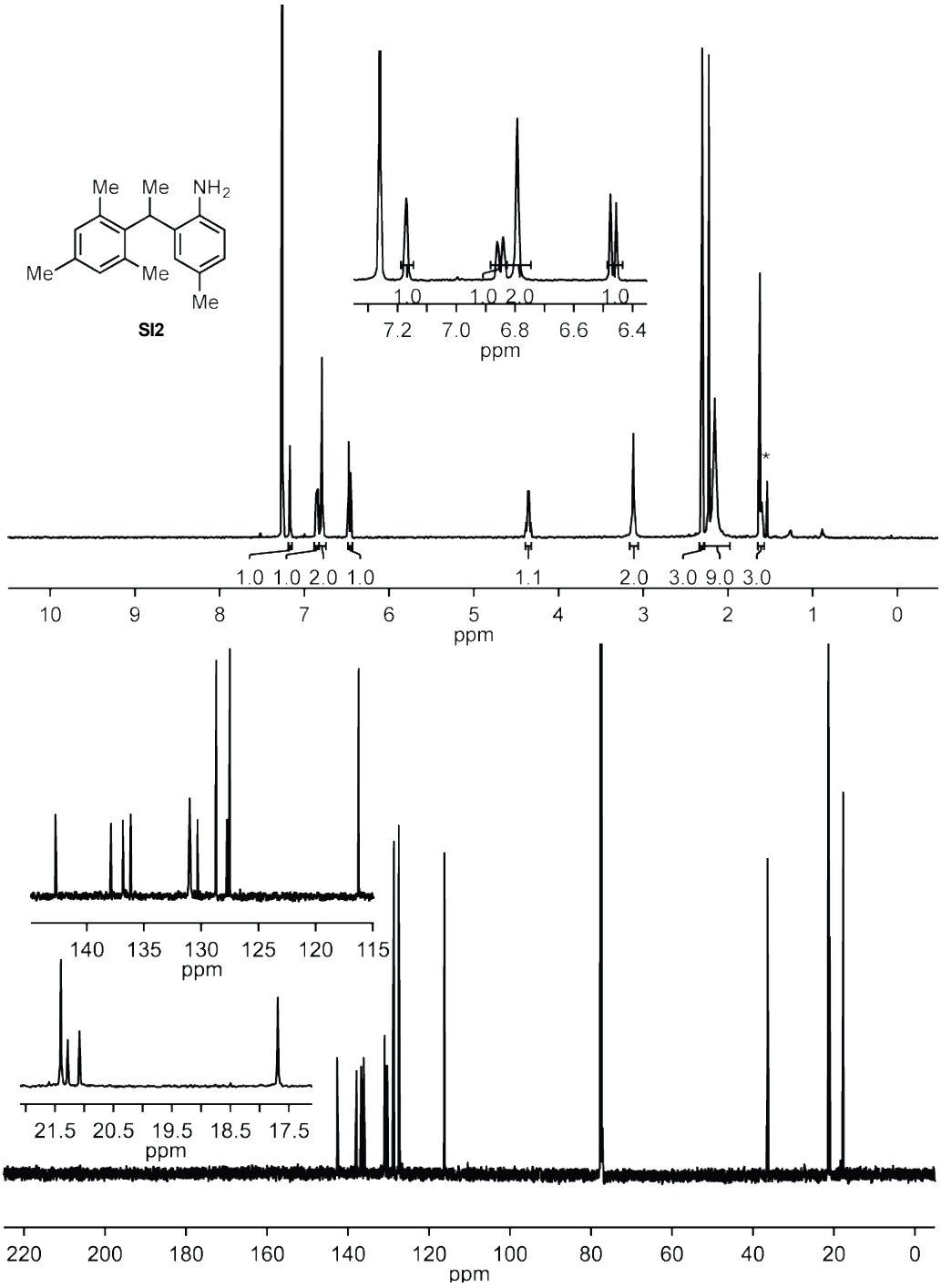

Figure 5.2: ^{1}H and ^{13}C NMR spectra of SI2. ^{1}H NMR (500 MHz, $CDCl_3$) δ 7.17 (s, 1H), 6.85 (dd, J = 7.9, 1.9 Hz, 1H), 6.80 (s, 2H), 6.47 (d, J = 7.9 Hz, 1H), 4.35 (q, J = 7.3 Hz, 1H), 3.12 (s, 2H), 2.30 (s, 3H), 2.19 (overlapping peaks, 9H), 1.61 (d, J = 7.3 Hz, 3H). ^{13}C NMR (126 MHz, $CDCl_3$) δ 142.22, 137.37, 136.33, 135.65, 130.49, 129.81, 128.20, 128.18, 127.25, 127.00, 126.99, 115.72, 35.92, 20.90, 20.89, 20.78, 20.57, 17.18. Taken by Amanda Leone.

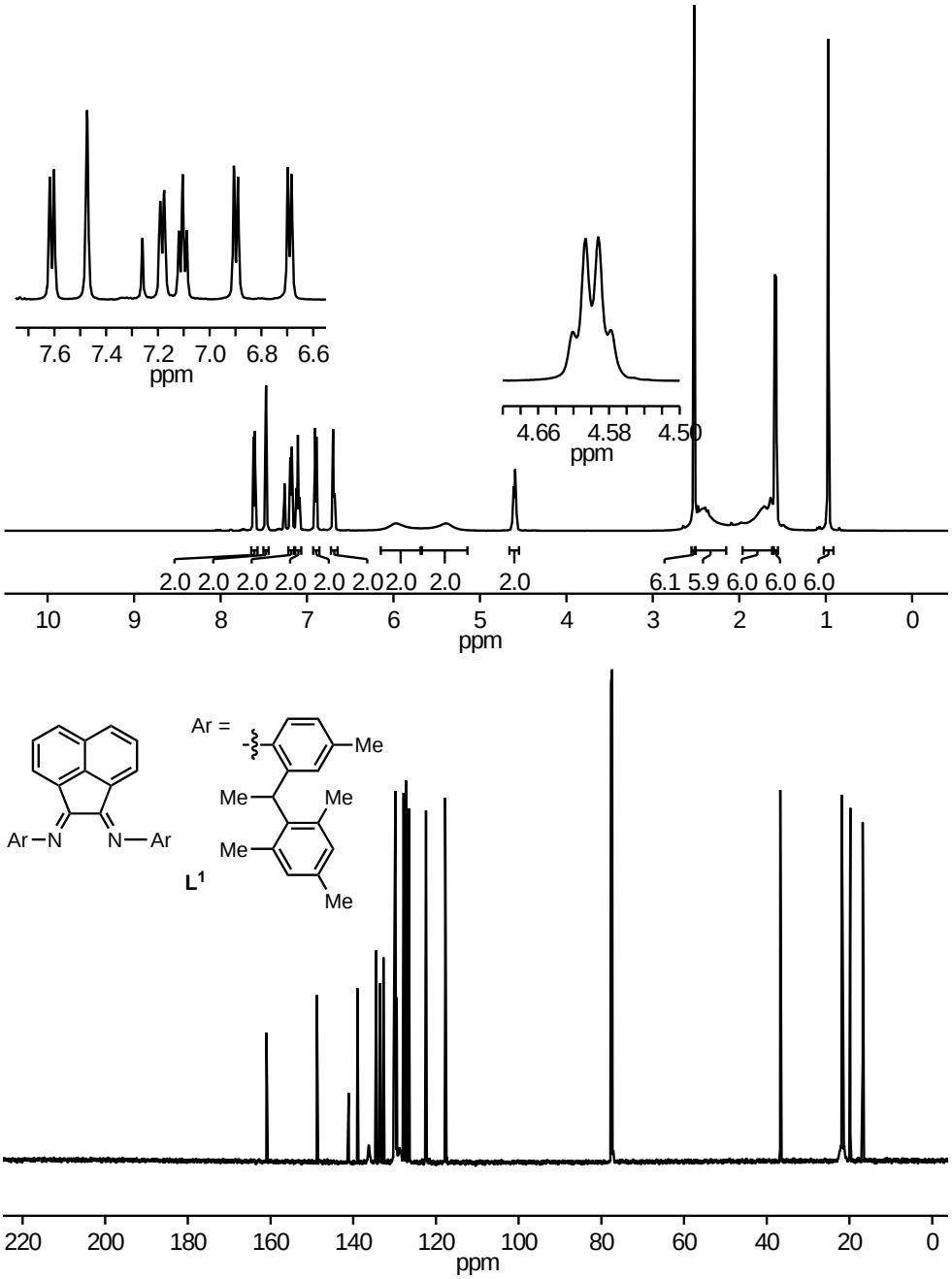

Figure 5.3: ^{1}H and ^{13}C NMR spectra of L^{1}. ^{1}H NMR (500 MHz, $CDCl_3$) δ 7.61 (d, J = 8.2 Hz, 2H), 7.47 (s, 2H), 7.18 (d, J = 7.7 Hz, 2H), 7.10 (t, J = 7.7 Hz, 2H), 6.90 (d, J = 7.8 Hz, 2H), 6.69 (d, J = 7.2 Hz, 2H), 5.97 (br s, 2H), 5.39 (br s, 2H), 4.60 (q, J = 7.4 Hz, 2H), 2.52 (s, 6H), 2.41 (br s 6H), 1.62 (br s, 6H), 1.58 (d, J = 7.4 Hz, 6H), 0.97 (s, 6H). ^{13}C NMR (126 MHz, $CDCl_3$) δ 161.00, 148.78, 141.11, 138.97, 136.22 (br), 134.46, 133.56, 132.70, 130.25, 129.80, 129.48, 128.78 (br), 127.85, 127.28, 126.57, 122.40, 117.77, 36.74, 21.84, 21.65 (br), 19.80, 16.80. Taken by Amanda Leone.

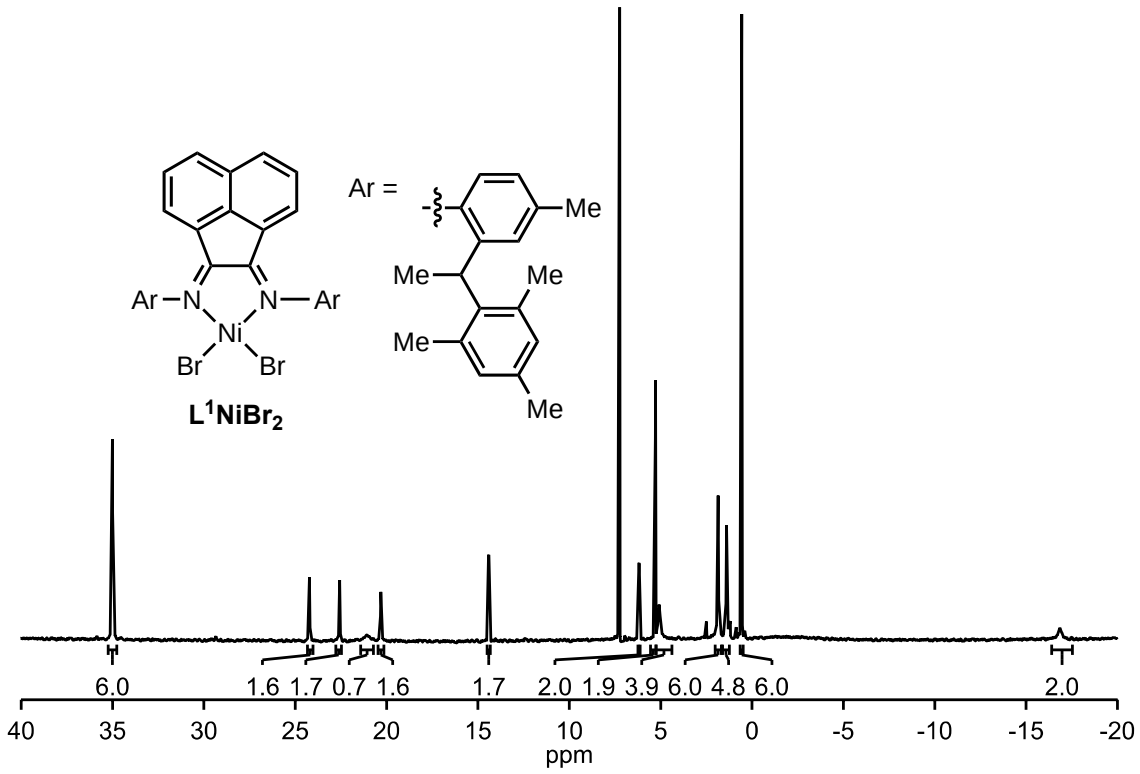

Figure 5.4: ^{1}H NMR Spectrum of L^{1}NiBr$_2$. ^{1}H NMR (400 MHz, $CDCl_3$) δ 35.02 (s, 6H), 24.24 (s, 2H), 22.59 (s, 2H), 21.06 (br s, 2H), 20.33 (s, 2H), 14.43 (d, J = 7.7 Hz, 2H), 6.20 (s, 2H), 5.30 (s, 2H), 5.09 (br s, 4H), 1.87 (s, 6H), 1.41 (s, 5H), 0.58 (s, 6H), –16.84 (br s, 2H). Unaccounted for hydrogens due to peak broadening. Taken by Amanda Leone.

A.1.5 Evan's Method[82,83]

For the following experiments, an NMR tube insert was made—by soldering a 4 mm glass tube (12.4 cm long) with a 3 mm glass tube (6 cm long)—to fit into a screw-cap NMR tube to enable air-free analysis (Figure 5.5).

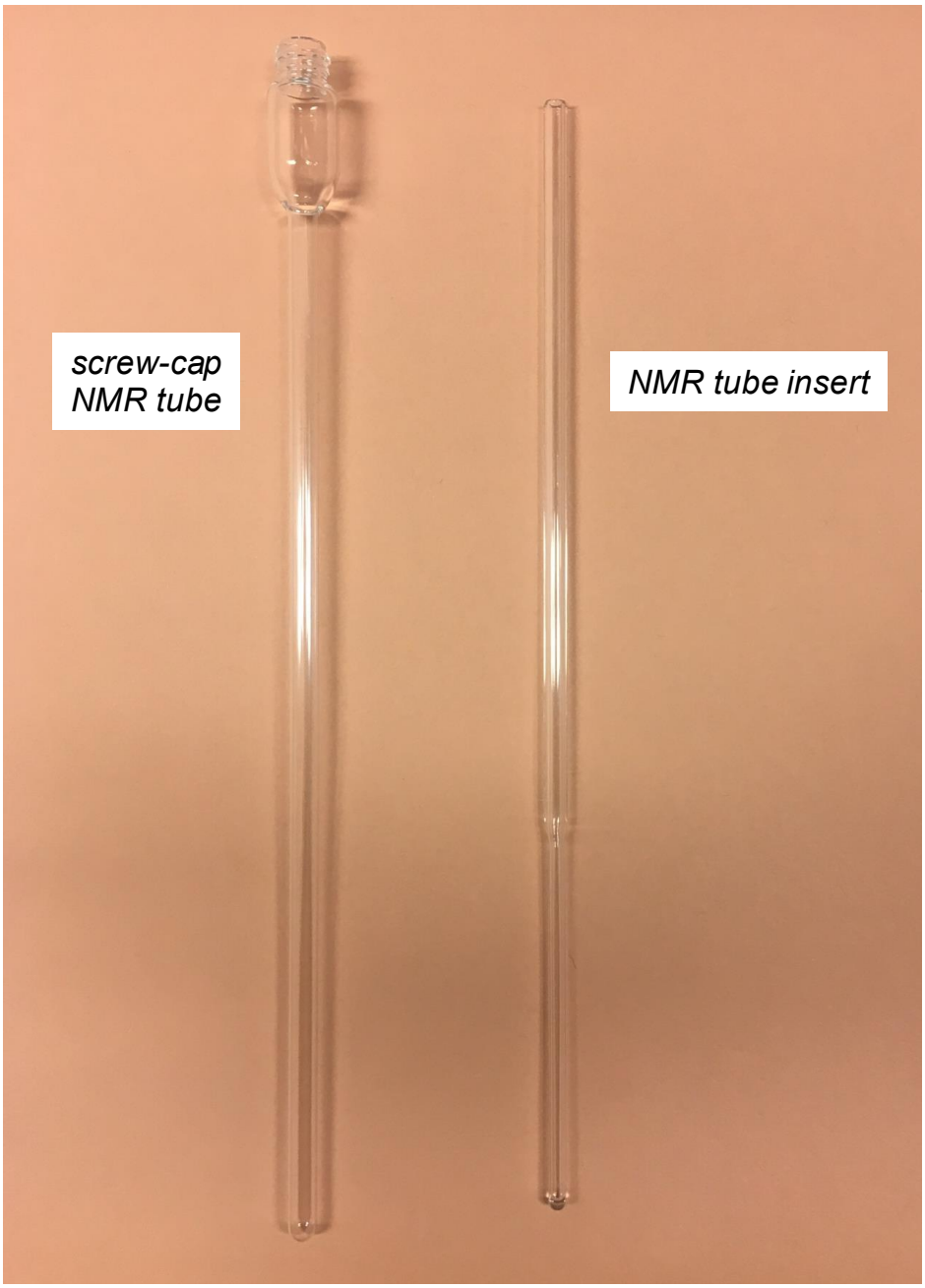

Figure 5.5: Image of a screw-cap NMR tube and NMR tube insert by Amanda Leone.

In a glovebox, THF-d_8 (0.1 mL) was added to two NMR tube inserts. Note that L^1Ni(thiophene)Br decomposes in CD_2Cl_2.

Preparing stock solutions

Complex **L[1]NiBr2** (15.8 mg, 0.0181 mmol) was dissolved in THF-d_8 (0.8 mL).

L[1]NiBr2: *Evan's Method Experiment*

An aliquot of the **L[1]NiBr2** (0.25 mL) stock solution was transferred to a screw-cap NMR tube. An NMR tube insert was carefully placed in the screw-cap NMR tube, which was sealed with a Teflon cap and electrical tape and removed from the glovebox for NMR spectroscopic analysis (Figure 5.6).

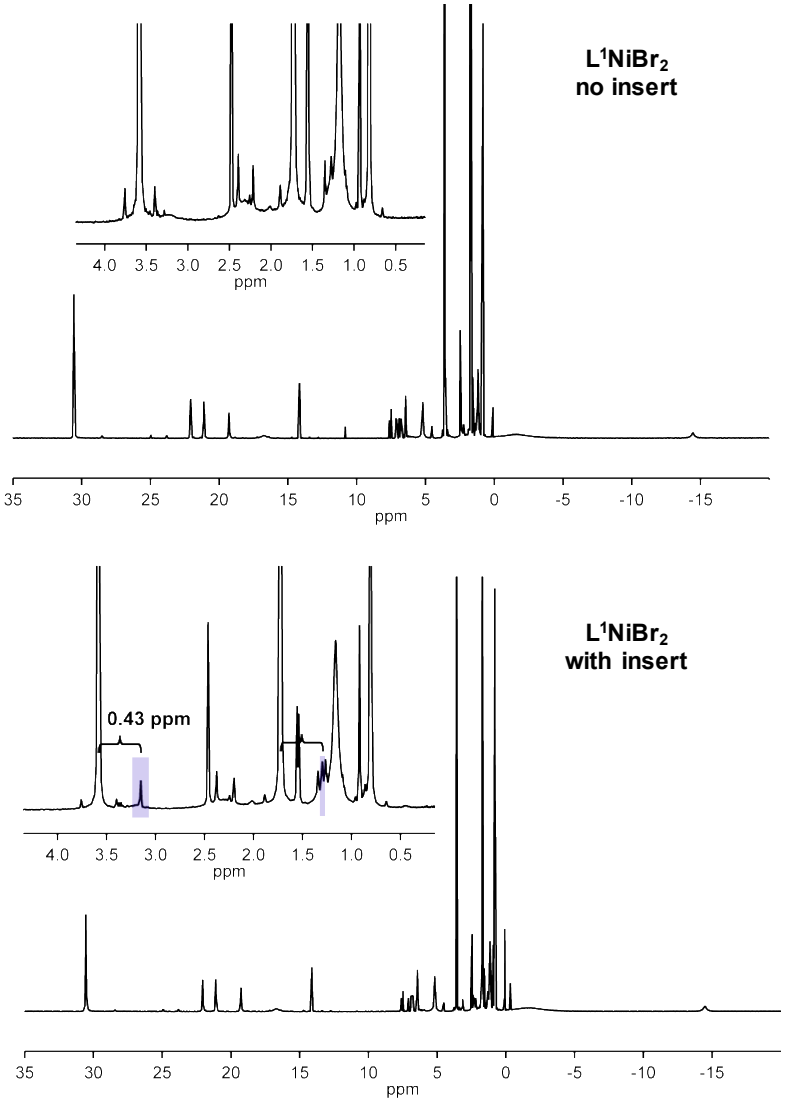

Figure 5.6: ^{1}H NMR spectra of the Evan's method **L[1]NiBr2** in THF-d_8 demonstrating THF-d_8 shift of 0.43 ppm. (Note that THF displaces **L[1]** causing an equilibrium between bound and unbound ligand, hence small but visible **L[1]** peaks.). Taken by Amanda Leone.

L[1]NiBr(thiophene): ***Evan's Method Experiment***

Preparing thiophene Grignard stock solution

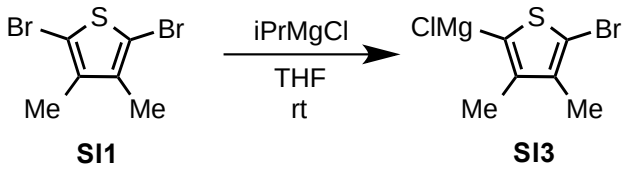

(5-bromo-3,4-dimethylthiophen-2-yl)magnesium chloride (SI3). A solution of **SI1** (16.7 mg, 0.0623 mmol, 1.00 equiv) and iPrMgCl (1.85 M in THF, 30.3 µL, 0.0561 mmol, 0.900 equiv) in THF-d_8 (0.593 mL) was stirred for 30 min at rt and then cooled to –30 °C for 5 min.

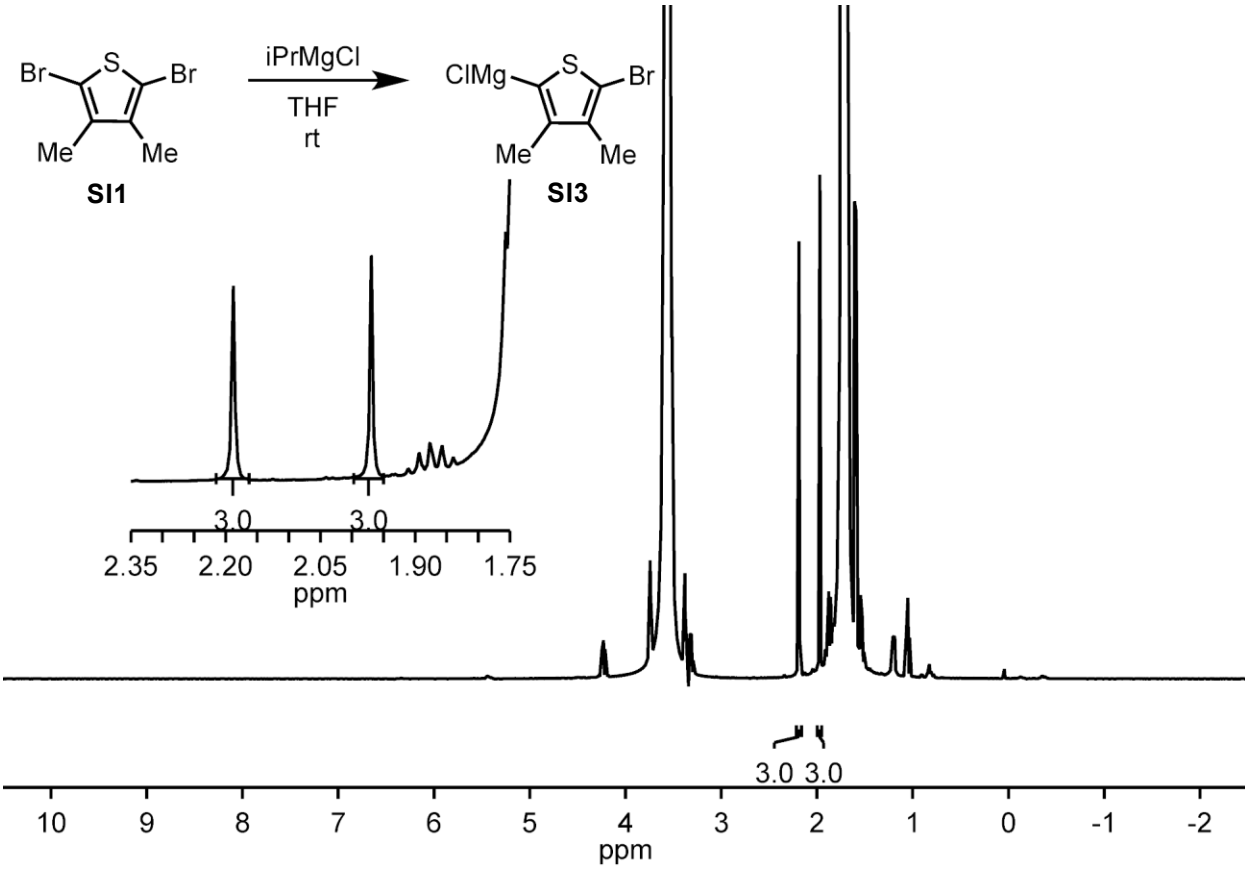

Figure 5.7: [1]H NMR spectrum for the reaction of SI1 with iPrMgCl. [1]H NMR (400 MHz, THF-d_8) δ 2.19 (s, 3H), 1.97 (s, 3H). Taken by Amanda Leone.

Generating L[1]NiBr(thiophene)

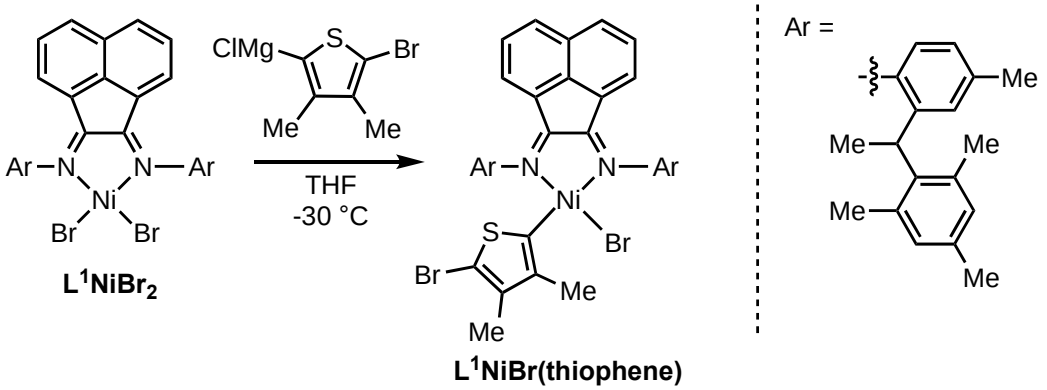

L[1]NiBr$_2$ **L[1]NiBr(thiophene)**

The prepared **L[1]NiBr$_2$** (10.9 mg, 0.0125 mmol, 1.00 equiv) stock solution was cooled to –30 °C for 5 min. Then, cold **SI3** (138 µL, 0.0125 mmol, 1.00 equiv) was added dropwise to the **L[1]NiBr$_2$** solution. The solution immediately changed from red to blue at which time it was moved to the –30 °C freezer for 2 min. Then, an aliquot of the solution (0.25 mL) was transferred to a screw cap NMR tube. An NMR tube insert was carefully placed in the screw-cap NMR tube, which was sealed with a Teflon cap and electrical tape and removed from the glovebox for NMR spectroscopic analysis. Spectroscopic analysis revealed complete consumption of **SI3** (indicated by absence of singlets at 2.19 and 1.17 ppm) as well as minimal unreacted **L[1]NiBr$_2$** (indicated by broad peaks > 10 ppm, Figure 5.7). After the NMR spectrum was acquired, the screw cap NMR tube containing **L[1]NiBr(thiophene)** and an NMR tube insert was cycled back into the glovebox and the insert was removed. To acquire an NMR spectrum without the NMR tube insert, additional **L[1]NiBr(thiophene)** solution (0.1 mL, required to shim the sample effectively) was added to the screw cap NMR tube. Note that the additional **L[1]NiBr(thiophene)** added had been stored in the –30 °C freezer during the initial NMR spectra acquiring. After adding **L[1]NiBr(thiophene)**, the screw cap NMR tube was sealed with a Teflon cap and electrical tape and removed from the glovebox for NMR spectroscopic analysis (Figure 5.8).

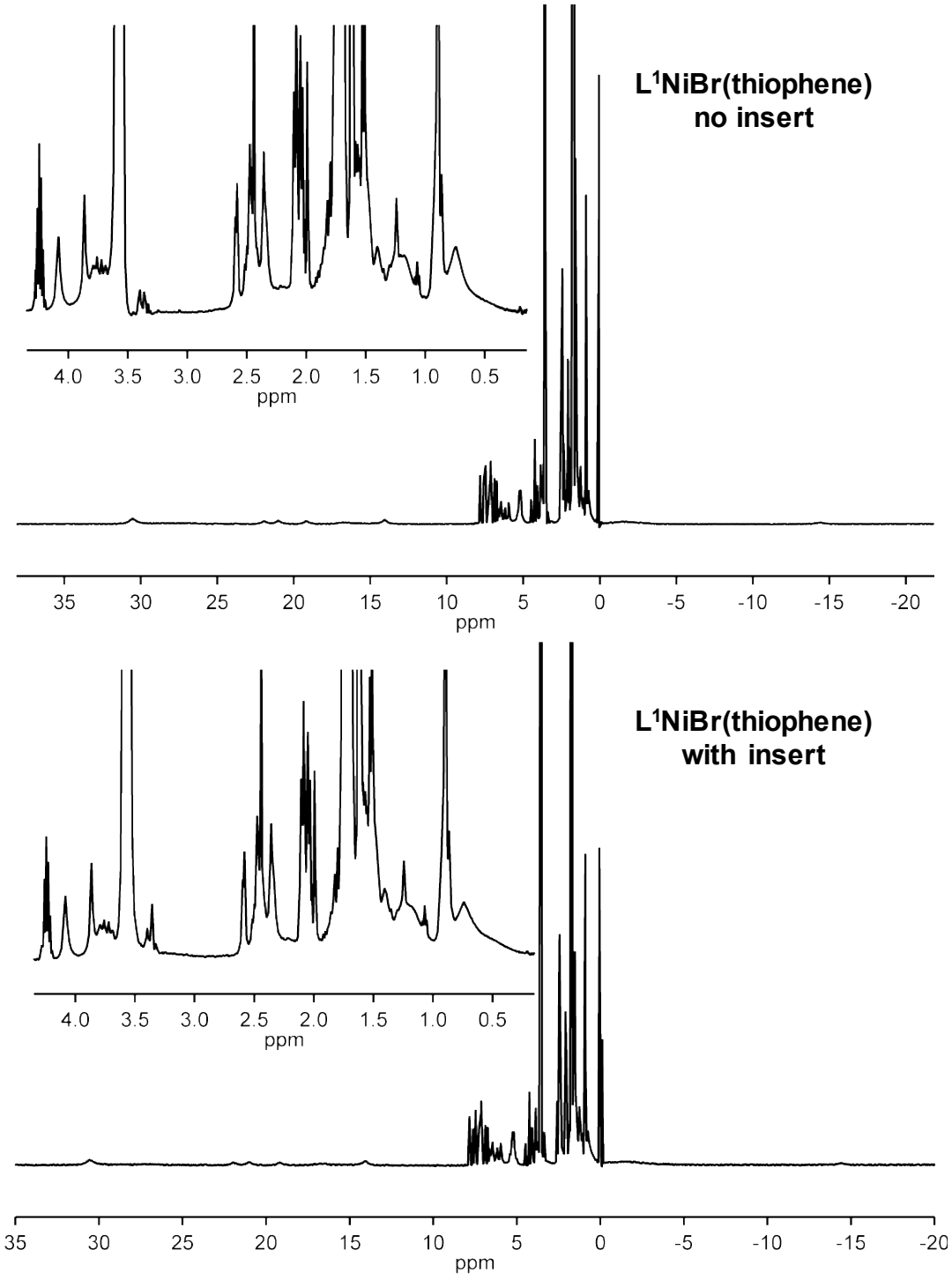

Figure 5.8: ^{1}H NMR spectra of the Evan's method **L^{1}NiBr(thiophene)** in THF-d_8 generated in situ. Taken by Amanda Leone.

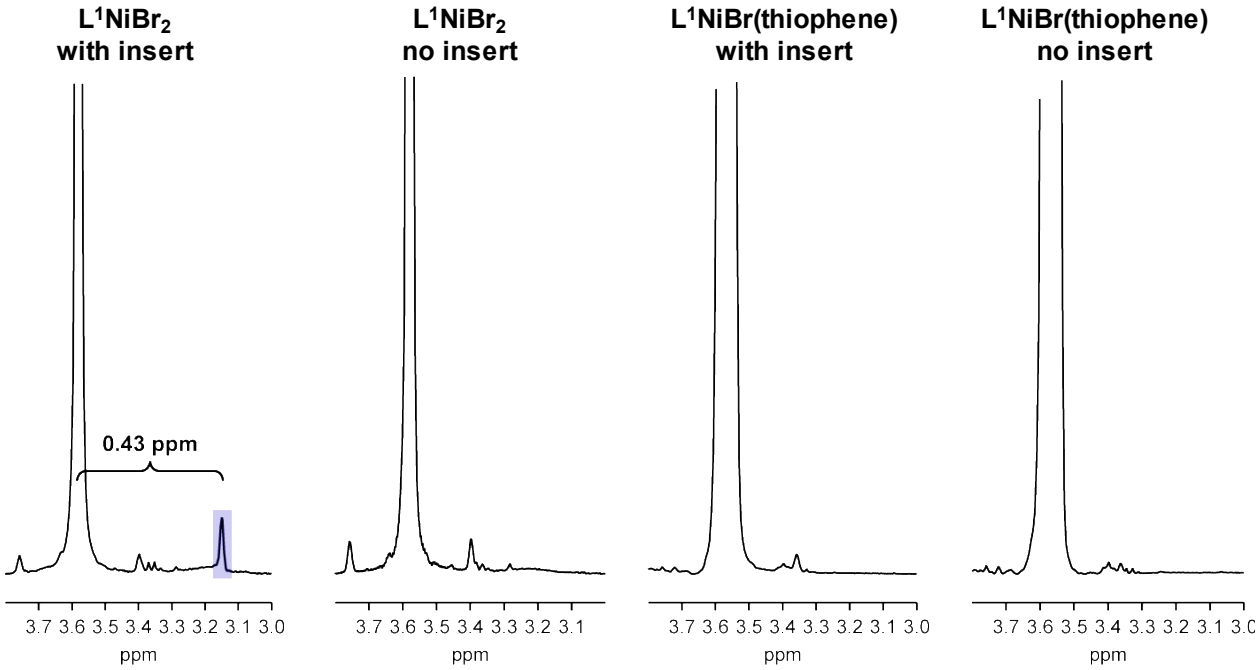

Figure 5.9: Zoomed-in region from the ^{1}H NMR spectra of **L^{1}NiBr$_2$** and **L^{1}NiBr(thiophene)** with/without NMR tube inserts in THF-d_8. Taken by Amanda Leone.

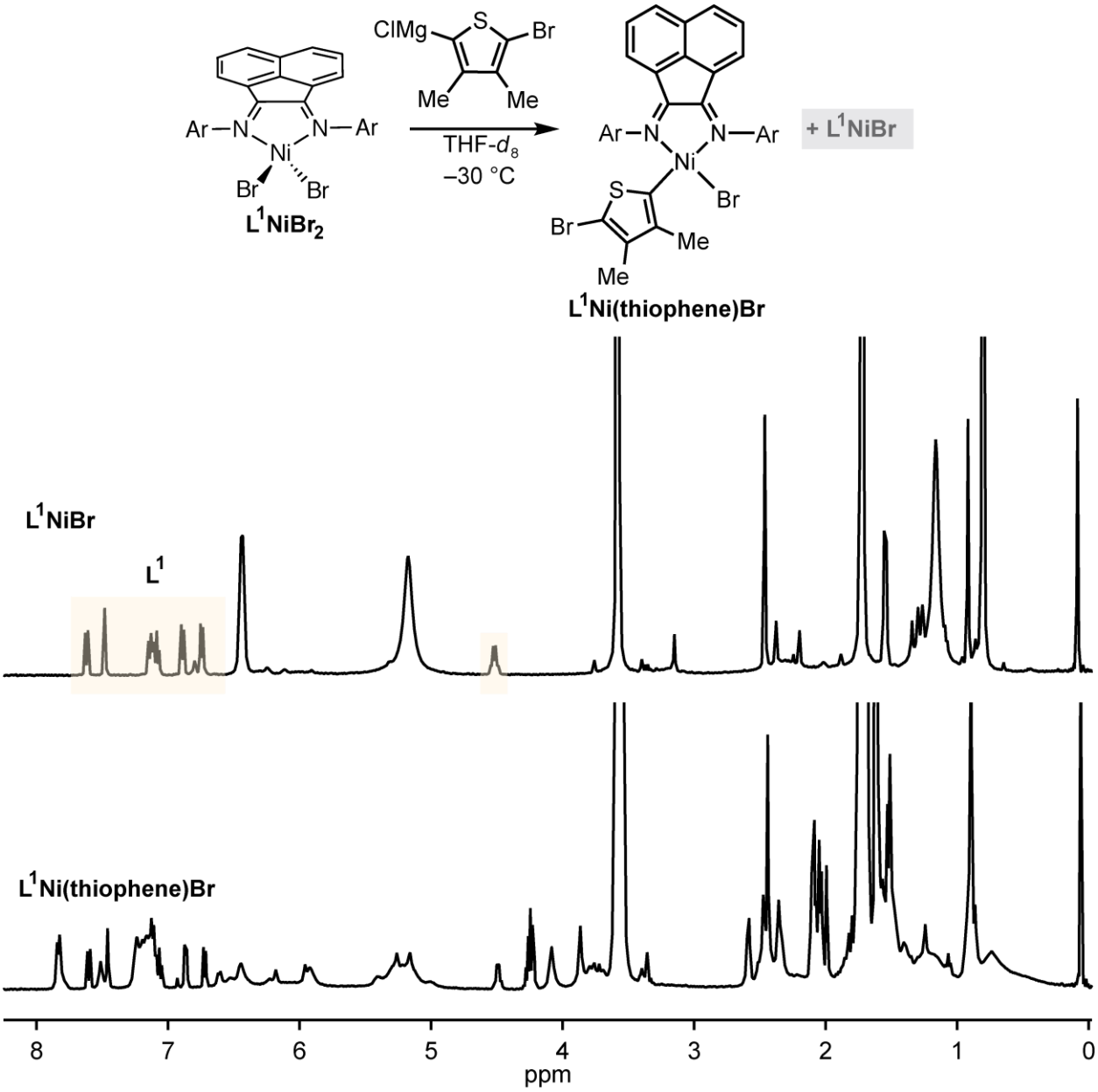

Figure 5.10: Zoomed-in region from the ^{1}H NMR spectra of **L^{1}NiBr$_2$** and **L^{1}Ni(thiophene)Br** with NMR tube inserts in THF-d_8 highlighting displaced L^{1} from the THF-d_8. Taken by Amanda Leone.

A.1.6 Variable Temperature ^{1}H NMR Spectra

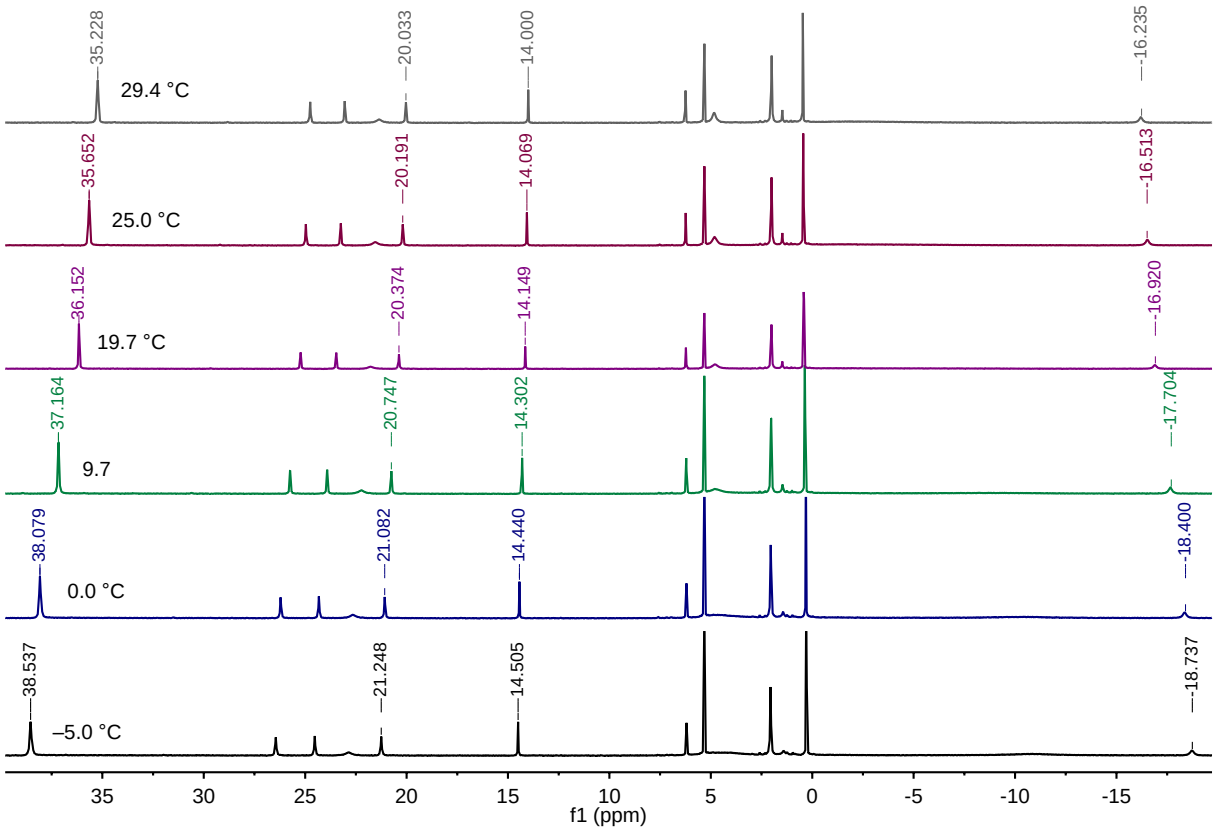

Figure 5.11: Variable temperature (–5 to 30 °C) ^{1}H NMR spectra for **L^{1}NiBr$_2$** in CD_2Cl_2. Taken by Amanda Leone.

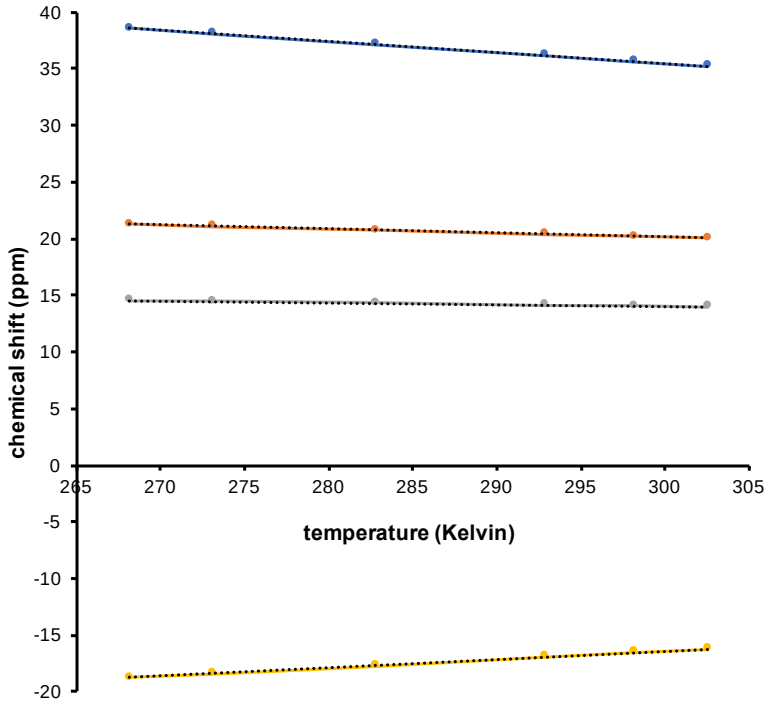

Figure 5.12: Plot of the chemical-shift-temperature dependence demonstrating that $\mathbf{L^1NiBr_2}$ follows Curie's law. Taken by Amanda Leone.

A.2 Computational Details

Density functional calculations were performed using the QChem 4.0 package.[5] All initial geometries for intermediates and transition states were obtained using the UB3LYP density functional[6-9] and LANL2DZ basis set and corresponding effective core potentials.[10-12] Energies for initial geometries were refined by applying the ωB97X density functional,[13] the cc-pVDZ[14] (on C/H atoms for ancillary ligands and THF molecules) and cc-pVTZ basis sets (for H/C atoms of Grignard reagents and reactive ligands and all N, O, Mg, S, Cl, Ni, and Br atoms, see Figure 5.13),[14-17] and the SMD implicit solvent model.[18-20] The mixed basis set treatment (cc-pVDZ/cc-pVTZ) was performed to make single point calculations more tractable while retaining chemical accuracy on all atoms involved in the discussed chemical transformations. All energies listed are Gibbs free energies with enthalpy and entropy corrections at 298.15 K. All intermediates and transition states were confirmed to have the appropriate number of imaginary frequencies. All geometry optimizations, frequency calculations, and single point calculations were performed with an SCF convergence of 10^{-6}.

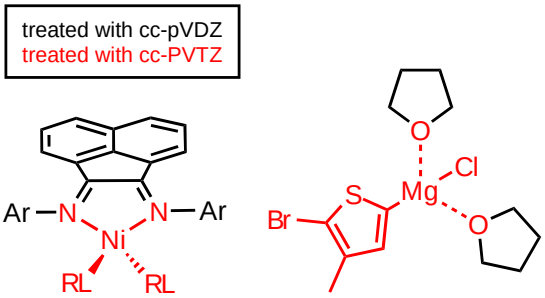

Figure 5.13: Atom-dependent basis set treatment of geometries when applying SMD corrections.

A.2.1 Electronic and steric distortions of truncated and reference Ni complexes

Steric bulk imparted by L^1 and L^2 result in unstable, twisted configurations of the reactive ligands (RLs) in $LNi(RL)_2$ complexes. The full system, which includes the two bisaryl pendant groups of L^1 and L^2, was truncated (replacing the bisaryl pendant groups with a H atom, see Figure 3.5) to quantify this RL distortion. The RLs of the truncated model complexes are frozen in unstable, twisted configurations imparted by L^1 and L^2. The energy required to twist the RLs of $LNi(RL)_2$ complexes (Figure 3.5) is shown in Table 5.1. Optimization of the truncated model complexes relaxes positions of the RLs and results in the reference model. For consistency, all energies are referenced to the appropriate high-spin (T1) reference complex. Table 5.1 shows that all reference geometries for a given $LNi(RL)_2$ complex are more stable than the corresponding truncated geometries and that L^2 imparts more distortion than L^1 for all listed complexes.

Complex	Ancillary Ligand	$\Delta H = H_{trnc.} - H_{ref.}$(T1) (kcal/mol)		α,β (°)	
		S0	T1	S0	T1
$LNiBr_2$	L^1, truncated	18.1	3.1	176.4, 171.9	106.3, 106.5
	L^2, truncated	22.8	11.9	157.7, 157.2	126.5, 127.5
	Reference	16.8	0	181.7, 184.7	102.4, 103.8
LNiBr(thiophene)	L^1, truncated	4.3	7.8	179.8, 177.7	107.5, 147.3
	L^2, truncated	12.1	13.2	155.0, 162.9	114.3, 153.3

	Reference	3.6	0	184.1, 187.0	103.3, 105.6
LNi(thiophene)$_2$	L^1, truncated	-9.8	4.1	177.3, 179.1	110.3, 140.3
	L^2, truncated	-3.1	13.7	160.8, 160.8	128.3, 135.8
	Reference	-10.3	0	186.7, 184.7	96.5, 147.3

Table 5.1: Relative energies between reference and truncated S0 and T1 geometries.

For an example calculating $\Delta H_{elec.}$ and $\Delta H_{ster.}$ using the full and truncated L^1NiBr_2 complex (see Figure 3.5 b), see Equations S1 – S10 below. For a list of all relevant energies and corrections for complexes where electronic and steric distortions are discussed, see Table 5.2.

$$H = E^{total} + H^{corr.} \quad (S1)$$

$$\Delta H = H(S0) - H(T1) \quad (S2)$$

$$\Delta H_{elec.} = \Delta H_{trunc.} - \Delta H_{ref.} \quad (S3)$$

$$\Delta H_{ster.} = \Delta H_{full} - \Delta H_{trnc.} \quad (S4)$$

Solving for $\Delta H_{elec.}$ and $\Delta H_{ster.}$ for the L^1NiBr_2 complex is explicitly shown below.

$$\Delta H_{elec.} = \left[\left(\mathrm{E}_{trunc.}^{total}(S0) + H_{trunc.}^{corr.}(S0)\right) - \left(\mathrm{E}_{trunc.}^{total}(T1) + H_{trunc.}^{corr.}(T1)\right)\right] - \left[\left(\mathrm{E}_{ref.}^{total}(S0) + H_{ref.}^{corr.}(S0)\right) - \left(\mathrm{E}_{ref.}^{total}(T1) + H_{ref.}^{corr.}(T1)\right)\right] \quad (S5)$$

$$\Delta H_{elec.} = [(-7769.14898 + 0.42367) - (-7769.17075 + 0.42143)] - [(-7769.15139 + 0.42398) - (-7769.17816 + 0.42395)] \quad (S6)$$

$$\Delta H_{elec.} = -0.00277\ Hartree = -1.74\ \frac{kcal}{mol} \quad (S7)$$

$$\Delta H_{ster.} = \left[\left(\mathrm{E}_{full}^{total}(S0) + H_{full}^{corr.}(S0)\right) - \left(\mathrm{E}_{full}^{total}(T1) + H_{full}^{corr.}(T1)\right)\right] - \left[\left(\mathrm{E}_{trunc.}^{total}(S0) + H_{trunc.}^{corr.}(S0)\right) - \left(\mathrm{E}_{trunc.}^{total}(T1) + H_{trunc.}^{corr.}(T1)\right)\right] \quad (S8)$$

$$\Delta H_{ster.} = [(-8624.25782 + 0.89532) - (-8624.27586 + 0.89504)] - [(-7769.14898 + 0.42367) - (-7769.17075 + 0.42143)] \quad (S9)$$

$$\Delta H_{ster.} = 0.00060\ Hartree = 0.38\ \frac{kcal}{mol} \quad (S10)$$

Species	S0		T1	
	E^{total} (Hartree)	$H^{corr.}$ (Hartree)	E^{total} (Hartree)	$H^{corr.}$ (Hartree)
L^1NiBr_2, trunc.	-7769.14898	0.42367	-7769.17075	0.42143
L^1NiBr_2, full	-8624.25782	0.89532	-8624.27586	0.89504
L^2NiBr_2, trunc.	-7769.14018	0.42236	-7769.15734	0.42210
L^2NiBr_2, full	-8702.81716	0.95474	-8702.83385	0.95342
$LNiBr_2$, ref.	-7769.15139	0.42398	-7769.17816	0.42395
L^1NiBr(thiophene), trunc.	-8360.24319	0.50303	-8360.23580	0.50134
L^1NiBr(thiophene), full	-9215.35264	0.97537	-9215.34217	0.97504
L^2NiBr(thiophene), trunc.	-8360.23031	0.50270	-8360.22898	0.50308
L^2NiBr(thiophene), full	-9293.90775	1.03587	-9293.90552	1.03483
LNiBr(thiophene), ref.	-8360.24548	0.50421	-8360.25092	0.50395
$L^1Ni(thiophene)_2$, trunc.	-8951.33108	0.58187	-8951.30847	0.58137
$L^1Ni(thiophene)_2$, full	-9806.44205	1.05581	-9806.41498	1.05489
$L^2Ni(thiophene)_2$, trunc.	-8951.32025	0.58162	-8951.29398	0.58215
$L^2Ni(thiophene)_2$, full	-9884.99798	1.11589	-9884.97430	1.11480
$LNi(thiophene)_2$, ref.	-8951.33434	0.58425	-8951.31746	0.58380

Table 5.2: Total electronic energies (including solvation corrections) and enthalpic corrections of low-spin (S0) and high-spin (T1) complexes under investigation for electronic/steric distortion discussion. The energies and corrections are listed in Hartree.

Figure 5.14 shows the relationship between the torsion of reactive ligands with respect to the diimine ligand versus the electronic enthalpy of distortion. All structures listed correspond to the truncated models of labeled $LNi(RL)_2$ complexes (Figure 3.5a). This graph quantifies the enthalpy of distortion as a function of the change in reactive ligand angles α and β (shown in Figure 3.4) and spin state. All enthalpies and torsional angles are referenced to the relaxed, reference model (shown in Figure 3.5a). Distortion($\Delta\alpha+\Delta\beta$) is measured as sum of absolute differences of torsional angles α and β with respect to the truncated L^1 and L^2 complexes versus the analogous reference complexes (see torsion angles listed in Table 5.1). With fairly good agreement, the truncated complexes exhibit a linear relationship with respect to electronic enthalpy of distortion and change in reactive ligand torsional angle. High-spin complexes exhibit ~0.1 kcal/mol more distortion per degree change in the reactive ligands and generally exhibit higher angles of distortion compared to low-spin complexes.

Figure 5.14 partially explains L^1 favoring the singlet state more than L^2 for the LNiBr(thiophene) complex (-7.1 kcal/mol for L^1 and -4.7 kcal/mol for L^2, see Figure 3.5b). The low-spin square planar L^1NiBr(thiophene) complex exhibits a large degree of twisting (45.9°) compared to all other L^1 complexes (6.6°–20.6°). This is due to the steric interactions of the full systems (see Figure 3.5a), which lead to distorted, high-spin tetrahedral LNiBr(thiophene) complexes. The high-spin "reference" complex only adopts a distorted tetrahedral geometry at $LNi(thiophene)_2$ when it has two bulky thiophene ligands, such that this effect is not precisely captured by the truncated model.

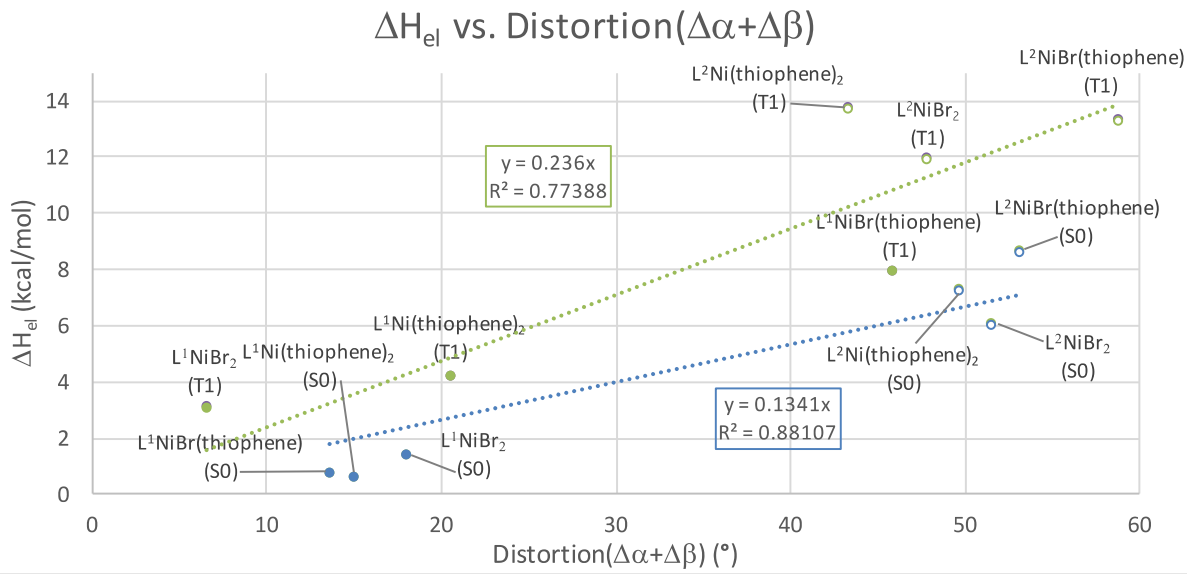

Figure 5.14: Change in electronic energy versus change in reactive ligand torsional angles compared to reference complex

A.2.2 Modeling Grignard solvation

Computational studies on Ni-catalyzed polymerizations that do not account for solvent participation often have large disagreements with experiment.[84–86] In contrast, explicit solvation of Grignard reagents for Ni- and Pd-catalyzed Kumada cross-coupling has demonstrated that solvent plays a critical role in these transformations and that explicit solvation of these systems is necessary to create an accurate model.[87–90] Furthermore, the roles of multiple pathways and spin states[80] have not been examined for Ni-catalyzed CTP.

The influence of solvent on thiophene Grignard transmetalation was evaluated with respect to the steric and electronic properties of Mg. Solvent bound to Mg of (thiophene)MgCl is required to accurately represent the transmetalating reagent, as evidenced by substantial, favorable binding energies of the solvent, tetrahydrofuran (THF), compared to the unsolvated Grignard reagent. The binding free energies and enthalpies were examined for 1–3 THF molecules binding to Mg and are shown in Figure 5.12.

a)

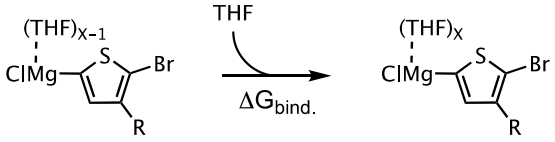

MX-1 MX

MX (# THF)	$\Delta G_{bind.}$ (kcal/mol)	$\Delta H_{bind.}$ (kcal/mol)	Mg charge	avg. Mg-O distance (Å)
0	-	-	0.79	-
1	-13.7	-25.3	0.67	2.00
2	-8.9	-20.5	0.54	2.04
3	3.0	-9.6	0.44	2.10

b)

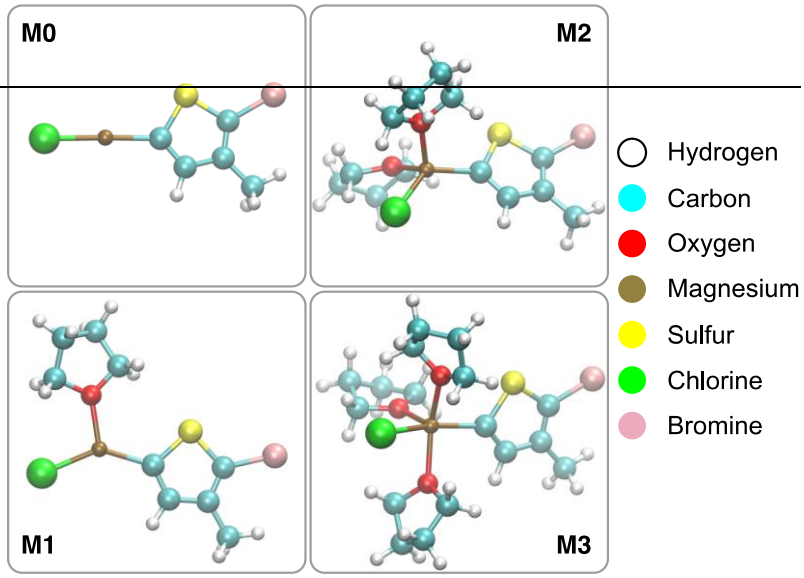

Figure 5.15: **a)** Binding energies of explicit THF solvent to Grignard reagent. **b)** Solvated Grignard reagents. **M2** will be used as the reference energy in the transmetalation reactions.

Addition of the first THF molecule (**M0→M1**) comes with a highly favorable binding enthalpy (–25.3 kcal/mol), which relieves Mg of a high partial charge (0.79 to 0.67 for **M0→M1**). Binding a second THF molecule (**M1→M2**) also shows a large, negative binding enthalpy (–20.5 kcal/mol) with further decrease in Mg charge (0.67 to 0.54 for **M1→M2**). Solvent saturation occurs at **M2** due to the less favorable binding enthalpy (–9.6 kcal/mol) for the third THF molecule (**M2→M3**). This binding enthalpy is not significant enough for the free energy to be negative, although addition of the third solvent molecule does reduce the positive Mulliken charge on the magnesium atom (0.54 to 0.44 for **M2→M3**). This can be understood by noting the average Mg-O distances increase with increased numbers of THF bound to Mg, such that each Mg-O bond is weakened by addition of each new THF (Figure 5.12a).

From these data, **M2** was selected to represent the Grignard transmetalating species in THF. The increased steric hindrance and decreased electrophilicity of the solvated Grignard are expected to significantly affect transmetalation barriers. Transmetalation pathways using **M2** will be physically relevant than the less stable **M0**, which has been shown via computations to have low to non-existent activation barriers and unfavorable thermodynamics for transmetalation.[84,85] Overall, because the most stable confirmation of Mg is **M2**, the energy of this complex will serve as part of the reference energy in the subsequent transmetalation studies. However for transmetalation process, **M1** will be utilized to allow steric accessibility between the catalyst and Grignard reagent. **M1** and **M2** are referred in the manuscript as (THF)MgCl(thiophene) and $(THF)_2$MgCl(thiophene).

A.2.3 Low-spin (S0) vs. high-spin (T1) transmetalation pathways for TM1-TM3

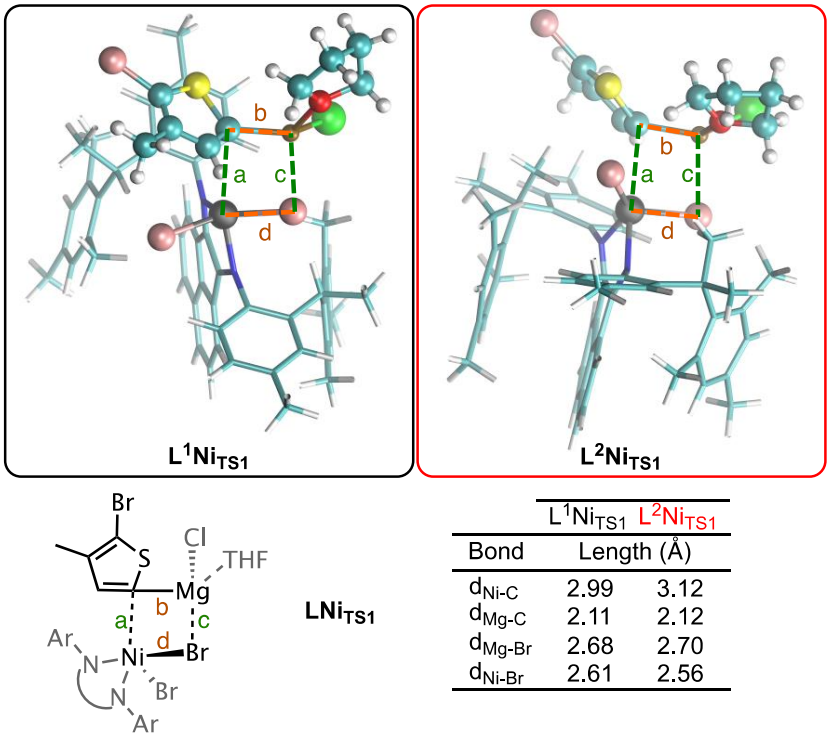

Bond	L^1Ni_{TS1} Length (Å)	L^2Ni_{TS1} Length (Å)
d_{Ni-C}	2.99	3.12
d_{Mg-C}	2.11	2.12
d_{Mg-Br}	2.68	2.70
d_{Ni-Br}	2.61	2.56

Figure 5.16: Transition state geometries for TM1.

Table 5.3 provides calculations that show relative energy of low- and high-spin transition states ($\Delta G^{\ddagger}$) and barrier heights (E_A) for **TM1** – **TM3**. Barrier heights are calculated by subtracting the energy of the transition state from the energy of the separated LNiBr(RL) and

$(THF)_2MgCl$(thiophene) complexes (RL=Br, thiophene, or dithiophene) for a given spin state. This data suggests that while the spin state of the catalytically active complex may switch between low- and high-spin states, the transmetalation reactions appear most stable in the high-spin state.

Ancillary Ligand	$\Delta G^{\ddagger}$(S0) – $\Delta G^{\ddagger}$(T1) (kcal/mol)			E_A(S0) – E_A(T1) (kcal/mol)		
	TM1	TM2	TM3	TM1	TM2	TM3
L1	19.5	8.1	13.2	5.9	12.6	17.7
L2	26.3	12.1	9.9	16.3	10.0	12.1

Table 5.3: Low-spin (S0) vs. high-spin (T1) transition state energies (ΔG) and barrier heights (E_A)

Reaction	Species	ΔG (kcal/mol)			
		L1		L2	
		S0	T1	S0	T1
TM1	$LNiBr_2$ + $(THF)_2MgCl$(thiophene)	13.6	0	10.0	0
	$LNiBr_{2Rct}$	16.3	9.9	16.8	5.6
	LNi_{TS1}	33.2	13.8	41.2	12.6
	$LNiBr_{2Prd}$	-0.9	10.8	-0.4	8.5
	LNiBr(thiophene) + $(THF)_2MgClBr$	-9.3	-4.9	-7.4	-9.5
TM2	LNiBr(thiophene) + $(THF)_2MgCl$(thiophene)	-4.5	0	2.1	0
	$LNiBr(thiophene)_{Rct}$	1.3	5.8	7.2	8.3
	LNi_{TS2}	19.5	7.5	29.4	18.0
	$LNiBr(thiophene)_{Prd}$	-4.1	6.9	4.9	10.6
	$LNi(thiophene)_2$ + $(THF)_2MgClBr$	-22.0	-8.8	-19.5	-4.7
TM3	LNiBr(dithiophene) + $(THF)_2MgCl$(thiophene)	-4.5	0	2.5	0
	$LNiBr(dithiophene)_{Rct}$	0.8	5.1	6.0	8.1
	LNi_{TS3}	19.6	8.9	30.3	20.7
	$LNiBr(dithiophene)_{Prd}$	-1.8	4.8	-0.3	18.4
	LNi(dithiophene)(thiophene) + $(THF)_2MgClBr$	-22.5	-4.1	-16.6	-5.6

Table 5.4: Relative energies of all low-spin (S0) and high-spin (T1) transmetalation pathways. The reference energy is the separated LNiBr(RL) complex in the high-spin state and $(THF)_2MgCl$(thiophene).

A.2.4 Density functional comparison

	Bond Distance (Å)			
	Exp.	B3LYP/ LanL2DZ	B3LYP/ 6-31G*	ωB97X-D/ 6-31G*
Ni-N^1	2.03	2.06	2.02	2.02
Ni-N^2	2.03	2.06	2.02	2.01
Ni-Br^1	2.33	2.45	2.36	2.34
Ni-Br^2	2.33	2.44	2.36	2.35
C^1-C^2	3.25-3.88	3.57-4.46	3.68-4.49	3.28-3.76
C^2-C^3	3.25-3.88	3.55-4.58	3.68-4.57	3.31-3.71

Table 5.5: Selected bonds for L^1NiBr_2 compared to X-ray structure

	B3LYP/ LanL2DZ	B3LYP/ 6-31G*	B3LYP-D3/ 6-31G*	ωB97X-D/ 6-31G*
Bond distance error (Å)	0.061	0.058	0.056	0.056
Bond angle error (°)	2.20	2.12	2.13	1.97
Torsion error (°)	6.50	6.44	7.62	6.14

Table 5.6: Average error of bond distances, angles and torsions for L^1NiBr_2 compared to X-ray structure.

Geometry optimizations using dispersion-corrected density functionals and a larger basis set were performed to compare DFT-optimized geometries of L^1NiBr_2 with the X-ray structure.[1] Increasing the basis set size from LanL2DZ to 6-31G* improved the important bond distances to the Ni metal center. When comparing geometries optimized with and without dispersion at the larger 6-31G* basis set, we found that the *ω*B97X-D geometry marginally improves the geometry with respect to the X-ray structure. The B3LYP-D3 geometry is slightly less accurate than B3LYP when compared to the X-ray structure. The bond distances involved in the π-π stacking interaction between the mesitylene and diimine-naphthalene moieties improve upon re-optimization with *ω*B97X-D.

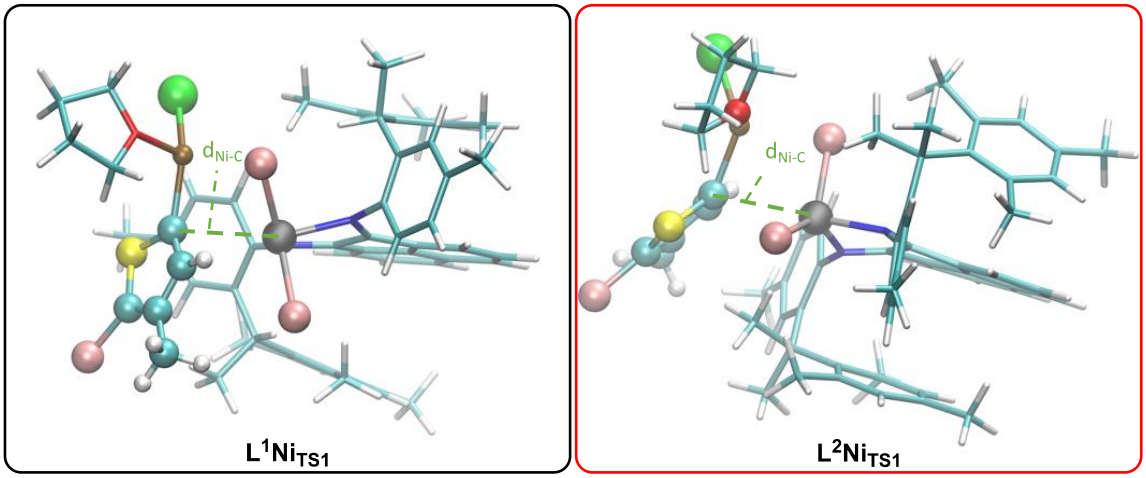

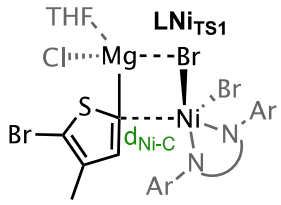

		L^1Ni_{TS1}	L^2Ni_{TS1}	L^1Ni_{TS1}	L^2Ni_{TS1}
	Bond	Length (Å)		Barrier Height (TM1)	ΔH (kcal/mol)
B3LYP/LanL2DZ	d_{Ni-C}	2.99	3.12	11.4	12.2
B3LYP-D3/6-31G*	d_{Ni-C}	3.03	3.18	4.3	4.8

Figure 5.17: Average error of bond distances, angles and torsions for L^1NiBr_2 compared to X-ray structure.

A comparison between Mg-C bond distances and barrier heights from the TM1 reaction using calculations with and without dispersion are provided in Figure 5.17. The absolute barrier heights change substantially when considering dispersion, but the relative barrier heights (0.8 and 0.5 kcal/mol) remain similar, as do the relative change in the Mg-C bond distance at the transition state (0.13 and 0.15 Å).

A.2.5 Computed spin gaps for full and reference systems

Complex	ΔE=E(S0)-E(T1) (kcal/mol)			
	B3LYP-D3/cc-pVTZ/SMD(THF)		*ω*B97X/cc-pVTZ/SMD(THF)	
	L^1	L^2	L^1	L^2
$LNiBr_2$	21.5	24.7	11.3	10.5
LNiBr(thiophene)	-1.6	12.5	-6.6	-1.4

Table 5.7: Computed spin gaps for full (L^1/L^2) complexes with and without dispersion

Complex	ΔE=E(S0)-E(T1) (kcal/mol)	
	CCSD(T)/def2-TZVP	*ω*B97X/cc-pVTZ
$LNiBr_2$ (ref)	30.8	19.0
LNiBr(thiophene) (ref)	13.5	4.1

Table 5.8: Computed CCSD(T) spin gaps for reference complexes

DLPNO-CCSD(T)[28]/def2-TZVP[29] calculations were performed in the ORCA4.0 quantum chemistry package.[30] The reported spin gaps for the reference complex (i.e. truncated sterics on ligands) indicate that the density functional values predict a S-T gap that is too low. At the key LNiBr(thiophene) intermediate, CCSD(T) suggests the triplet is favored by 9.4 kcal/mol more than *ω*B97X predicts. Adding this approximate correction to the Table 5.7 gaps places the triplet state as more favored for both ligands. This affirms the main texts suggestions that transmetalation preferentially occurs from the triplet state through tetrahedral geometries.

As a note, the difficulties of achieving high accuracy spin gaps with DFT is well documented.[31-36] Spin gaps are known to be dependent on the functional or amount of Hartree-Fock exchange. On the other hand, the trend in spin gap is subject to cancellation of errors, and therefore differences in gap from one reactive or ancillary ligand to the next should be relatively accurate.

A.3 References

(1) Cherian, A. E.; Rose, J. M.; Lobkovsky, E. B.; Coates, G. W. *J. Am. Chem. Soc.* **2005**, *127*, 13770–13771.

(2) Love, B. E.; Jones, E. G. *J. Org. Chem.* **1999**, *64*, 3755–3756.

(3) Evans, D. F. J. Chem. Soc. **1959**, 2003–2005.

(4) Sur, S. K. J. Magn. Reson. **1989**, *82*, 169–173.

(5) Shao, Y.; Gan, Z.; Epifanovsky, E.; Gilbert, A. T. B.; Wormit, M.; Kussmann, J.; Lange, A. W.; Behn, A.; Deng, J.; Feng, X.; Ghosh, D.; Goldey, M.; Horn, P. R.; Jacobson, L. D.; Kaliman, I.; Khaliullin, R. Z.; Kuś, T.; Landau, A.; Liu, J.; Proynov, E. I.; Rhee, Y. M.; Richard, R. M.; Rohrdanz, M. A.; Steele, R. P.; Sundstrom, E. J.; Woodcock, H. L.; Zimmerman, P. M.; Zuev, D.; Albrecht, B.; Alguire, E.; Austin, B.; Beran, G. J. O.; Bernard, Y. A.; Berquist, E.; Brandhorst, K.; Bravaya, K. B.; Brown, S. T.; Casanova, D.; Chang, C.-M.; Chen, Y.; Chien, S. H.; Closser, K. D.; Crittenden, D. L.; Diedenhofen, M.; DiStasio, R. A.; Do, H.; Dutoi, A. D.; Edgar, R. G.; Fatehi, S.; Fusti-Molnar, L.; Ghysels, A.; GolubevaZadorozhnaya, A.; Gomes, J.; Hanson-Heine, M. W. D.; Harbach, P. H. P.; Hauser, A. W.; Hohenstein, E. G.; Holden, Z. C.; Jagau, T.-C.; Ji, H.; Kaduk, B.; Khistyaev, K.; Kim, J.; Kim,J.; King, R. A.; Klunzinger, P.; Kosenkov, D.; Kowalczyk, T.; Krauter, C. M.; Lao, K. U.;Laurent, A. D.; Lawler, K. V.; Levchenko, S. V.; Lin, C. Y.; Liu, F.; Livshits, E.; Lochan, R. C.; Luenser, A.; Manohar, P.; Manzer, S. F.; Mao, S.-P.; Mardirossian, N.; Marenich, A. V.; Maurer, S. A.; Mayhall, N. J.; Neuscamman, E.; Oana, C. M.; Olivares-Amaya, R.; O'Neill, D. P.; Parkhill, J. A.; Perrine, T. M.; Peverati, R.; Prociuk, A.; Rehn, D. R.; Rosta, E.; Russ, N. J.; Sharada, S. M.; Sharma, S.; Small, D. W.; Sodt, A.; Stein, T.; Stück, D.; Su, Y.-C.; Thom, A. J. W.; Tsuchimochi, T.; Vanovschi, V.; Vogt, L.; Vydrov, O.; Wang, T.; Watson, M. A.; Wenzel, J.; White, A.; Williams, C. F.; Yang, J.; Yeganeh, S.; Yost, S. R.; You, Z.-Q.; Zhang, I. Y.; Zhang, X.; Zhao, Y.; Brooks, B. R.; Chan, G. K. L.; Chipman, D. M.; Cramer, C. J.; Goddard, W. A.; Gordon, M. S.; Hehre, W. J.; Klamt, A.; Schaefer, H. F.; Schmidt, M. W.; Sherrill, C. D.; Truhlar, D. G.; Warshel, A.; Xu, X.; Aspuru-Guzik, A.; Baer, R.; Bell, A. T.; Besley, N. A.; Chai, J.-D.; Dreuw, A.; Dunietz, B. D.; Furlani, T. R.; Gwaltney, S. R.; Hsu, C.-P.; Jung, Y.; Kong, J.; Lambrecht, D. S.; Liang, W.; Ochsenfeld, C.; Rassolov, V. A.; Slipchenko, L. V.; Subotnik, J. E.; Van Voorhis, T.; Herbert, J. M.; Krylov, A. I.; Gill, P. M. W.; Head-Gordon, *M. Mol. Phys.* **2015**, *113*, 184–215.

(6) Becke, A. D. J. Chem. Phys. **1993**, *98*, 5648–5652.

(7) Lee, C.; Yang, W.; Parr, R. G. *Phys. Rev. B* **1988**, *37*, 785–789.

(8) Vosko, S. H.; Wilk, L.; Nusair, M. *Can. J. Phys.* **1980**, *58*, 1200–1211.

(9) Stephens, P. J.; Devlin, F. J.; Chabalowski, C. F.; Frisch, M. J. *J. Phys. Chem.* **1994**, *98*, 11623–11627.

(10) Hay, P. J.; Wadt, W. R. *J. Chem. Phys.* **1985**, *82*, 299–310.

(11) Hay, P. J.; Wadt, W. R. *J. Chem. Phys.* **1985**, *82*, 270–283.

(12) Wadt, W. R.; Hay, P. J. *J. Chem. Phys.* **1985**, *82*, 284–298.

(13) Chai, J. Da; Head-Gordon, M. *J. Chem. Phys.* **2008**, *128*, 084106.

(14) Dunning, T. H. *J. Chem. Phys.* **1989**, *90*, 1007–1023.

(15) Woon, D. E.; Dunning, T. H. *J. Chem. Phys.* **1995**, *103*, 4572–4585.

(16) Balabanov, N. B.; Peterson, K. A. *J. Chem. Phys.* **2005**, *123*, 064107.

(17) Wilson, A. K.; Woon, D. E.; Peterson, K. A.; Dunning, T. H. *J. Chem. Phys.* **1999**, *110*, 7667–7676.

(18) Cammi, R.; Tomasi, J. *J. Comput. Chem.* **1995**, *16*, 1449–1458.

(19) Tomasi, J.; Mennucci, B.; Cammi, R. *Chem. Rev.* **2005**, *105*, 2999–3093.

(20) Aleksandr V. Marenich, Christopher J. Cramer, and D. G. T. *J. Phys. Chem. B* **2009**, *113*, 6378–6396.

(21) Bahri-Laleh, N.; Poater, A.; Cavallo, L.; Mirmohammadi, S. A. *Dalt. Trans.* **2014**, *43*, 15143–15150.

(22) Bhatt, M. P.; Magurudeniya, H. D.; Sista, P.; Sheina, E. E.; Jeffries-EL, M.; Janesko, B. G.; McCullough, R. D.; Stefan, M. C. *J. Mater. Chem. A* **2013**, *1*, 12841–12849.

(23) Chass, G. a; Kantchev, E. A. B.; Fang, D.-C. *Chem. Commun. (Camb).* **2010**, *46*, 2727–2729.

(24) Zhao, Y.; Nett, A. J.; McNeil, A. J.; Zimmerman, P. M. *Macromolecules* **2016**, *49*, 7632–7641.

(25) Yoshikai, N.; Matsuda, H.; Nakamura, E. *J. Am. Chem. Soc.* **2009**, *131*, 9590–9599.

(26) Hatakeyama, T.; Hashimoto, S.; Ishizuka, K.; Nakamura, M. *J. Am. Chem. Soc.* **2009**, *131*, 11949–11963.

(27) Ogawa, H.; Minami, H.; Ozaki, T.; Komagawa, S.; Wang, C.; Uchiyama, M. *Chem. - A Eur. J.* **2015**, *21*, 13904–13908.

(28) Riplinger, C.; Neese, F. *J. Chem. Phys.* **2013**, *138*. 034106.

(29) Weigend, F.; Ahlrichs, R. *Phys. Chem. Chem. Phys.* **2005**, *7*, 3297–3305.

(30) Neese, F. ORCA, version 4.0; Max-Planck-Institut für Bioanorganische Chemie: Mülheim an der Ruhr, Germany, **2004**.

(31) Orms, N.; Krylov, A. I.; *Phys. Chem. Chem. Phys.* **2018**, published online, DOI:10.1039/C7CP07356A

(32) Swart, M. *Int. J. Quantum Chem.* **2013**, *113*, 2−7.

(33) Costas, M.; Harvey, J. N. *Nat. Chem.* **2013**, *5*, 7−9.

(34) Harvey, J. N. *Annu. Rep. Prog. Chem., Sect. C: Phys. Chem.* **2006**, *102*, 203−226.

(35) Ghosh, A. *J. Biol. Inorg. Chem.* **2006**, *11*, 712−724.

(36) Ghosh, A.; Taylor, P. R. *Curr. Opin. Chem. Biol.* **2003**, 113−124.

Appendix B: Supporting Information for Chapter 4

B.1 τ_4' Equation

$$\tau_4{}' = \frac{\beta - \alpha}{360° - \theta} + \frac{180° - \beta}{180° - \theta}$$

Equation 5.1: τ_4' equation.

where $\beta > \alpha$ are the two greatest valence angles at the metal center and θ is 109.5° (typical tetrahedral angle).

B.2 Geometry Index Comparison

The qualitative relationship between increasing bisphosphine bite angle and decreasing reductive barrier height is implicitly shown in Figure 4.6, which depicts conformer barriers for the eight studied ancillary ligands. Bisphosphine bite angles increase when the alkyl backbone of the ancillary ligand increases (e.g. the bite angle from dmpe to dmpp increases by ~8°). Reductive elimination barrier heights decrease when the propyl backbone is substituted for the ethyl backbone for the four side chains studied. The quantitative relationship between bisphosphine bite angle and barrier height, however, shows weak correlation (shown in Table 5.9). A more descriptive geometry parameter, τ_4', shows much stronger correlation with barrier height for all of the studied ancillary ligands.

Ancillary Ligand	Correlation (R^2) with barrier height	
	Bite Angle (°)	τ_4'
dmpe	0.26	0.37
dmpp	0.01	0.41

dppe	0.21	0.79
dppp	0.09	0.52
dcpe	0.10	0.16
dcpp	0.05	0.25
dtpe	0.42	0.69
dtpp	0.00	0.98
all	0.13	0.71

Table 5.9: Correlation of geometry parameters (bite angle and τ_4') with reductive elimination barrier height.

B.3 Conformer Generation Scheme

Reaction simulation methods developed by the Zimmerman group (i.e. ZStruct2[1]) have proven useful for automating the exploration of chemical space for transition metal catalyzed reactions in a systematic and efficient manner.[2] However, in systems with flexible substrates or ligands the conformational impact of these structures remains unexplored and the choice of conformer used for reaction exploration is left to human intuition. This can prove problematic when numerous conformations can be imagined because generation of the lowest energy conformer becomes a non-trivial task that is ignored in most cases. The neglect in searching conformational space can lead to inaccuracies in energetic information gained through reaction exploration, due to not using the lowest energy conformer as the starting point for reaction discovery.

To address this issue our research group has developed a method for conformer generation, CGen, as outlined in Figure 5.18. This new method allows for metal-ligand or metal-substrate complexes to be generated with various ligand or substrate conformers, providing insight into the number of possible low energy structures that could exist, ultimately giving way to more accurate modeling of reaction pathways using ZStruct2 and the Growing String Method (GSM).[3]

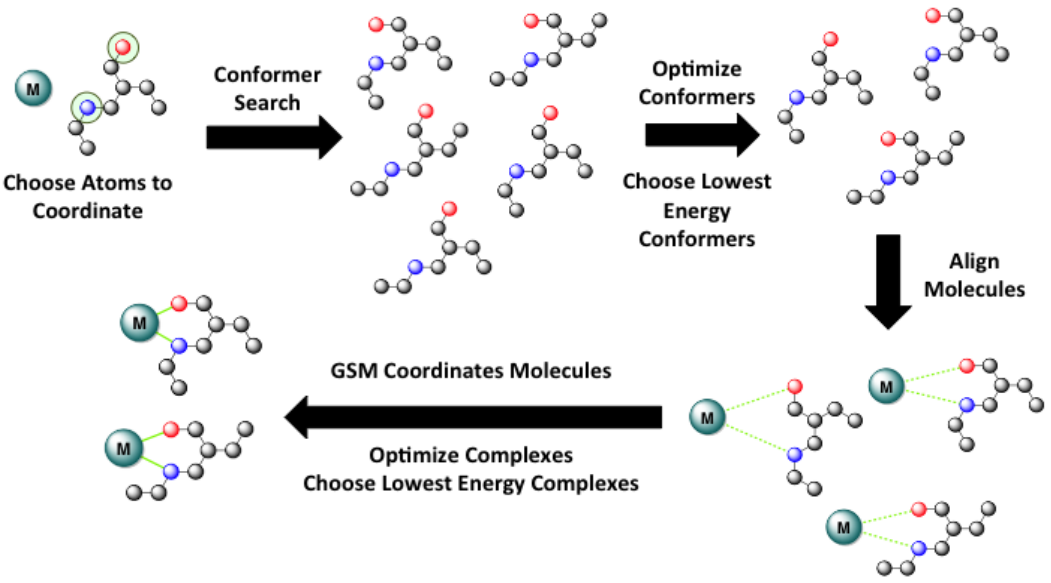

Figure 5.18: Flow chart for the generation, optimization, and screening of conformer complexes using CGen developed by Amanda Dewyer.

The method described in Figure 5.18 begins with the selection of two species, the metal center, and ligand/substrate that will be bound to the metal center. Once the ligand/substrate is defined the use must choose which atoms on each structure (i.e. the metal of the metal center and the chelating atom of the ligand/substrate) will be coordinated in the final complexes that are generated. Once this choice is made our method utilizes openBabel's confab method[4] to generate conformers of the ligand/substrate by rotating all of the "rotatable" bonds within the molecule. From the conformers that are generated openBabel performs a low accuracy Molecular Mechanics optimization and then applies an energetic cutoff to identify the lowest energy structures. These conformers are then aligned with one another based on the atoms that are selected to be coordinated to one another by the user. Once the molecules are aligned, a modified version of GSM is used to push the metal center and ligand/substrate towards one another until a low energy complex is generated. The complexes are then optimized using semi-empirical

methods, and another energy cutoff is applied to the end structures. From there the user can further optimize the lowest energy structures using DFT/high levels of theory to gain more accurate energetic comparisons of the complexes generated, and assess the impact of the ligand/substrate conformation on the number of conformers that need to be considered during reaction exploration.

In the studies from Chapter 4, the nickel bisphosphine complexes that contain two thiophene reactive ligands are separated into two species: the nickel center bound to the two thiophene reactive ligands and the bisphosphine ancillary ligand. To generate the set of conformers for a given ancillary ligand and nickel dithiophene pair, first the ancillary ligand and the nickel dithiophene species were treated separately with the openBabel's conformer fabrication method. The nickel dithiophene species generated two stable conformers with the "up-up" and "up-down" thiophene reactive ligand configurations (see Figure 4.7) while the ancillary ligand generated a number of conformers that varied with the flexibility of the ligand. The conformers of the ancillary ligand and nickel dithiophene were then aligned to bind the bisphosphine to the nickel metal center and optimized using DFT (see section 4.5). Conformers were compared using the root-mean-square deviation of atomic particles to ensure that each conformer was unique.

B.4 π-π stacking interactions

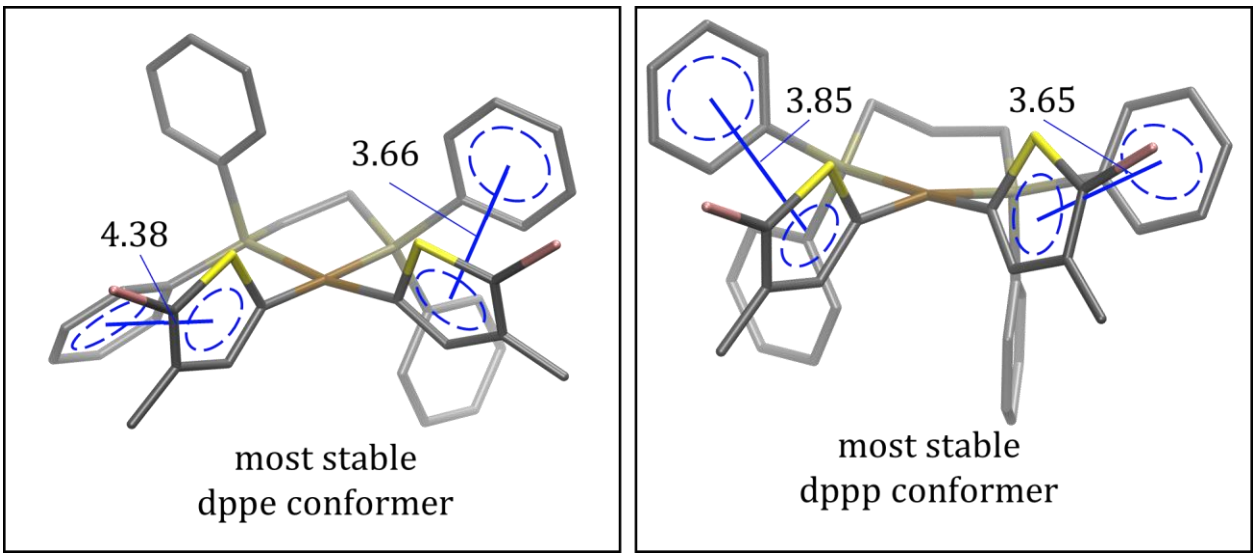

Figure 5.19: π-π stacking interactions of the most stable conformers of dppe and dppp.

B.5 References

(1) Dewyer, A. L., Zimmerman, P. M. *Org. Biomol. Chem.* **2017,** 15, 501-504.

(2) (a) Dewyer, A. L., Zimmerman, P. M. *ACS Catal.* **2017**, 7, 5466-5477. (b) Nett, A. J., Zhao, W., Zimmerman, P. M., Montgomery, J. *J. Am. Chem. Soc.* **2015,** 137, 7636. (c) Pendleton, I. M., Perez-Temprano, M. H., Sanford, M. S., Zimmerman, P. M. *J. Am Chem. Soc.* **2016,** 138, 6049.

(3) (a) Zimmerman, P. M. *J. Chem. Phys.* **2013,** 138, 1840102. (b) Zimmerman, P. M. *J. Comput. Chem.* **2005,** 36, 601

(4) O'Boyle, N. M., Banck, M., James, C. A., Morley, C., Vandermeersch, T., Hutchinson, G. R. *J. Cheminformatics* **2011,** 3, 1-14